High Performance CMOS-Compatible Perovskite Oxide Memristors: Compositional Control and Nanoscale Switching Characteristics

A thesis submitted in fulfilment of the requirements for the degree of

DOCTOR OF PHILOSOPHY

Hussein Nili Ahmadabadi

B.Sc.

School of Electrical and Computer Engineering

RMIT University

January 2015

DECLARATION

I certify that except where due acknowledgement has been made, the work is that of the author alone; the work has not been submitted previously, in whole or in part, to qualify for any other academic award; the content of the thesis is the result of work which has been carried out since the official commencement date of the approved research program; and, any editorial work, paid or unpaid, carried out by a third party is acknowledged.

_____

Hussein Nili Ahmadabadi

January 2015

ACKNOWLEDGMENTS

This PhD research program would not have been possible without the ongoing support and help of many people. First and foremost, I would like to thank my primary supervisors, Dr. Madhu Bhaskaran and Dr. Sharath Sriram; their detailed and rigorous scientific approach, their persistent assistance with every aspect of the research project and their unwavering trust and support, have been ubiquitous to the successful implementation of the research ideas and have carried me through the process from the very beginning. I am grateful for all the unique opportunities provided to me by my supervisors. I would also like thank my associate supervisor, Prof. Kourosh Kalantar-zadeh, for his excellent suggestions and valuable ideas on my research. During the last year of my PhD, I have been in close contact with Dr. Dmitri Strukov (University of California, Santa Barbara) and have benefitted immensely from his expertise in the field. His contributions to the success of this PhD are gratefully acknowledged.

The state-of-the-art scientific equipment and facilities of RMIT University have been indispensable in the successful completion of this research program. The valuable support of the technical staff across the network of RMIT University is gratefully acknowledged. I would like to thank Mr. Yuxun Cao, Mr. Paul Jones and Mrs. Chi-ping Wu of RMIT's Microelectronics and Materials Technology Center for their support. Valuable assistance of Mr. Philip Francis, manager of RMIT's Microscopy and Microanalysis Facility, and Mr. Peter Rummel is appreciated.

I would also like to thank my colleagues and friends in the School of Electrical Engineering, Functional Materials and Microsystems Research Group and RMIT's School of Applied Sciences. The assistance and support of Dr. Sumeet Walia, Dr. Ahmad Esmaielzadeh-Kandjani, Dr. Sivacarendran Balendhran, Mr. Philipp Gutruf, Dr. Rajesh Ramanathan, Prof. Vipul Bansal, Dr. Mahyar Nasabi and Mr. Andreas Boes are greatly appreciated.

I deeply treasure the absolute support and encouragement of my parents and my sister throughout the course of this research program. Without them, none of these would have been possible.

Finally, the love and support I have received from my lovely partner, Nazanin Shobeiri, throughout these years cannot be adequately cherished. Her enthusiasm for my work and persistent encouragements during the most troubling times, her complete acceptance and understanding of the long working hours (including the weekends) and her sacrifices to see me through this program have astonished me to end. I shall just simply thank her for "being".

Contents

LIST OF FIGURES

LIST OF TABLES

GLOSSARY

AFM	Atomic Force Microscopy
a-STO	Amorphous Strontium Titanate
EDX	Energy Dispersive X-Ray Analysis
KNN	Potassium Sodium Niobate
MIM	Metal-Insulator-Metal
MIT	Metal-Insulator-Transition
STO	Strontium Titanate
XPS	X-Ray Photoelectron Spectroscopy
XRD	X-Ray Diifraction
τ	Time Constant
D	Diffusion Constant
K	Boltzmann Constant
F	Faraday Constant
υ	Poisson's Ratio
E	Elastic Modulus
H	Hardness
φ	Magnetic Flux
μ_V	Ionic Mobility

ABSTRACT

Nanoscale memristive devices have been dubbed as one of the main contenders for the next generation nonvolatile memories (NVM) and alternative logic architectures. Passive two-terminal metal-insulator-metal (MIM) memristive crossbar configurations based on functional transition metal-oxides (e.g. TiO_2, $SrTiO_3$) offer great potential for ultimate integration in contemporary electronic industry. The bipolar resistive switching behavior in these devices is attributed to a combination of electronic effects at the metal/oxide interfaces and reversible redox reactions and nanoionics transport in transition metal-oxide layers. However, the underlying microscopic conduction and switching mechanisms are not yet fully understood.

Complex transition metal oxides with Perovskite crystal structure are among the most technologically relevant classes of electronic materials. A plethora of functional properties such as ferro/piezoelectricity, ferromagnetism, superconductivity and memristivity can be engineered through the compositional and structural modification of the perovskite structure.

This thesis focuses on the realization and nanoscale characterization of high performance CMOS-compatible memristive devices utilizing functional perovskite oxides. A PVD based synthesis route for the realization of functional perovskite oxides with control over their composition and structure has been

established. Utilizing the synthesis approach, first realization of memristive devices based on oxygen deficient amorphous $SrTiO_3$ (*a*-STO) oxides has been demonstrated and their resistive switching performance has been studied in detail utilizing micro-scale crossbar MIM arrays and a sophisticated conductive nano-contact technique based on *in situ* electrical nanoindentation.

RF magnetron sputtering has been used in this work to synthesis perovskite oxide thin films on conventional silicon substrates. Firstly, a lead-free ferro/piezoelectric perovskite oxide ($K_xNa_{1-x}NbO_3$) was chosen to study the effects of sputtering parameters and post-deposition treatments on the composition and the structure of sputtered thin films. This study demonstrates that the crystal orientation, thickness and the elemental composition of the thin films sputtered from the same ceramic target can be effectively and reliably controlled *via* tuning the sputtering parameters (process gas, substrate temperature, etc.) and the oxide structure and secondary phases can be engineered through post-annealing treatments. The same procedure was employed for the synthesis of $SrTiO_3$ thin films as a reliable resistive switching perovskite oxide. A low temperature synthesis of amorphous $SrTiO_3$ (*a*-STO) thin films with precise control over the thickness, oxygen deficiency and A-site/B-site dopants has been demonstrated for the first time.

The switching characteristics of *a*-STO cross-point devices suggest the possibility of fine tuning the memristive performance through tailoring the oxide composition and device structure. Outstanding switching performance (high switching ratios, excellent endurance and retention) is demonstrated in oxygen deficient *a*-STO devices. Also, it is shown that niobium doping through low

temperature co-sputtering of Nb: *a*-STO result in significant improvements in device energy requirements.

Furthermore, nanoscale conduction and resistive switching mechanisms of these devices have been studied in detail utilizing a sophisticated *in situ* electrical nanoindentation technique, capable of forming nano-contacts with controlled size and mechanical force. To this end, a unique empirical model has been developed that allows for a complete characterization of the electrical properties of the load controlled nano-contact and therefore yields quantified insights into the conduction and switching mechanisms of *a*-STO based memristive device at nanoscale. The results exhibit ultimately scalable and isolatedly controllable switching characteristics in these devices and also suggest the possibility of mechanically modulated nanoscale resistive switching in a-STO based devices.

Overall, this thesis highlights *a*-STO based devices as strong candidates for the ongoing development of the alternative memory technologies as well as applications in MEMS/NEMS devices.

CHAPTER 1

INTRODUCTION

1.1. Context and Objectives

The emerging field of oxide nano-electronics is expanding in scientific discoveries and technological relevance at a fascinating pace [1.1-4]. The exotic properties of complex oxide structures and interfaces arise from interactions between charged species in the strongly correlated complex oxide systems. These properties are the gateway to new electronic devices capable of surpassing their semiconductor-based predecessors both in scale and performance. Two-dimensional electron gases, superconductivity and colossal magnetoresistivity at correlated oxide interfaces, ultrafast metal-insulator transitions (MIT) actuated by a variety of external stimuli (thermal, mechanical, electrical, optical, etc.) in complex transition metal oxides, and ultrafast highly nonlinear resistive switching in metal-oxide-metal cells are just a few examples of the potential of complex oxide systems for novel electronic devices and applications. The ongoing research efforts are aimed at developing a comprehensive understanding of the physical phenomena in complex correlated oxide systems and the ultimate realization of advanced oxide-based electronic

devices through controlling the properties of complex oxides and oxide interfaces.

Information processing and data storage capabilities of conventional semiconductor-based devices are almost at their limits as the industry is reaching the scaling and performance limits of such devices. Among several candidates for alternative memory and information processing devices, solid-state resistive random access memories (RRAMs) and memristive devices have proven to be a viable option due to their scalability potential and reliable performance characteristics. Research in the relatively advanced RRAM field is now focused on realizing large scale integration of memristive devices in hybrid CMOS compatible systems, optimizing the performance of RRAM device through material and structural engineering, and developing physical and circuit element based analysis and simulation models for the ultimate integration of these devices in contemporary electronic industry.

The rapid progress in the realm of complex functional oxides and nanostructures and the consistent pursuit of miniaturization of electronic devices, relies heavily on the capabilities of characterization and analysis tools available to materials scientists. Of particular interest, are multi-sensory and *in situ* characterization tools that can provide valuable information about nanoscale phenomena and correlated properties and enable scientists to develop ever more accurate pictures of the physical nature of the properties of complex functional oxides.

The motivation behind this thesis aligns with the demands of the expanding field of oxide nanoelectronics. The control of the physical and functional properties of

complex oxides through control of their structure and composition is a topic of immense importance. The PhD research project outlined in this thesis starts with exploring the relationship between the synthesis conditions of complex perovskite oxides and their compositional and structural characteristics with the aim to establish a synthesis protocol for functional perovskite oxides. The oxide systems chosen for these investigation include a ferro/piezoelectric complex perovskite oxide system (potassium sodium niobate, $K_xNa_{1-x}NbO_3$: KNN) and a prototypical perovskite oxide system (strontium titanate, $SrTiO_3$: STO) with the potential to be used as the functional layer in solid-state memristive devices. The research project then focuses on exploring the memristive properties of engineered perovskite oxides to attain high-performance memristive devices. The project uses an advanced electromechanical characterization tool (*in situ* electrical nanoindentation) to gain fundamental nanoscale insights into the mechanisms of the memristivity and resistive switching in perovskite oxides.

1.2. Original Contributions

The primary achievements and original contributions through the course of this PhD research project are listed below:

- A PVD synthesis and post-synthesis treatment protocol has been developed to achieve monolithic perovskite oxide thin films on CMOS compatible substrates (platinized Si and SiO_2/Si) with thicknesses controllable to less than 10 nm. In the context of perovskite oxides systems studied in this PhD research project:

- Ferro/piezoelectric potassium sodium niobate (KNN) thin films with controllable alkali ratio and crystal orientation were synthesized through high temperature RF magnetron sputtering using a single ceramic target and post-annealing treatments. The facile synthesis and post-treatment route allows for the effective control of the ferro/piezoelectric properties of KNN thin films through compositional and structural engineering.

- Pristine and co-doped amorphous strontium titanate (*a*-STO) thin films were synthesized using a single stoichiometric ceramic target *via* room temperature RF magnetron sputtering. The control over synthesis parameters allow for precise control over thickness, oxygen deficiency content, and external dopants. These tuning procedures allow for effective control over the electronic band structure of *a*-STO. As such, the technique can serve as an efficient enabler for engineering the physical properties of STO oxides.

- First realization of CMOS compatible, high performance micro-scale *a*-STO based metal-insulator-metal (MIM) memristive cells was achieved. The composition of the amorphous oxide and the MIM cell were engineered to attain optimal memristive performance in *a*-STO based cells. In-depth compositional, electrical and nanoscale studies reveals the underlying mechanisms of the switching performance of *a*-STO based devices and suggests their scaling potential for high density electronic devices.

- *In situ* electrical nanoindentation tool was utilized to study the nano-electromechanical coupling effects in *a*-STO oxides. To attain fundamental quantitative insights, an empirical model has been developed to isolate and eliminate the role of nanoindentation probe contact geometry and resistance in the *in situ* electrical results.

    - The effect of machine compliance, surface roughness, thermal drift and friction, and probe geometry on the nano-electromechanical response data of the indented materials has been investigated and correction methods have been developed to increase the accuracy of data analysis to a large degree. The effectiveness of the correction procedure has been tested and demonstrated in a study on nano-crystalline platinum thin films.

    - An empirical model developed to map and analyse the contact resistance versus the contact depth which can be utilized to study the nano-electromechanical response of a large variety of material systems. This quantitative approach also allows for the utilization of *in situ* electrical nanoindentation method as a stable and precisely controllable conductive SPM tool, whereby SPM nano-contacts are electrically grounded, their diameters and contact areas are verifiable and controllable, and their position can be precisely defined and kept stationary for extended periods of time. This will prove as a very powerful toolbox for the investigation of nanoscale functional systems.

- Using the aforementioned *in situ* electrical nanoindentation and conductive nano-contact analysis technique the conduction and switching

mechanisms in *a*-STO cells and oxides has been investigated. Several significant insights have been achieved including the multi-filamentary nature of redox-based switching mechanisms in *a*-STO memristive cells. It has also been highlighted that these filamentary pathways with sub 100 nm dimensions can be individually and reliably switched which hints at the ultimate scalability and reliability of *a*-STO based devices.

- Direct *in situ* electrical nanoindentation experiments on *a*-STO oxide layers of different thicknesses provide further valuable insights into the nanoscale nature of conduction mechanisms and the possibilities of multi-stimuli modulation of physical properties of complex perovskite oxide systems.

1.3. Thesis Outline

This thesis has been segmented into chapters as individual entities of research. The major chapters of this thesis are as follows:

Chapter 2 provides a brief background on the research into perovskite oxide systems and complex oxide structures, memristive devices and systems and *in situ* electrical nanoindentation technique.

Chapter 3 presents the optimized PVD synthesis technique for the realization of perovskite oxide thin films (KNN and STO perovskite oxide systems) with controlled composition, crystal structure and defect chemistry.

Chapter 4 presents the results of investigations of the switching performance of *a*-STO based MIM cells, highlighting their memristive performance and linking

their characteristics to the composition and defect chemistry of *a*-STO oxide layers.

Chapter 5 details nanoscale investigations of conduction and switching mechanisms in *a*-STO oxides. In this chapter, the methodology for using *in situ* electrical nanoindentation technique as an accurate probing technique for electromechanical coupling effects as well as a displacement and contact size controlled conductive SPM has been detailed. The method has then been used to study the nanoscale conduction mechanisms in *a*-STO MIM cells and ultrathin oxide-metal stacks.

This thesis has three appendices: (i) Appendix A details the experimental methods and technique used throughout this thesis. (ii) Appendix B details the use of *in situ* electrical nanoindentation technique in accurate nano-electromechanical characterization of nanocrystalline platinum thin films. (iii) Appendix C provides an abstract of the use of *in situ* electrical nanoindentation technique in the investigations of electromechanical couplings in quasi-2D MoS_2 and MoO_3 layers.

1.4. Publications

Following is a list of peer-reviewed publications during the course of this PhD program. All publications relate to the synthesis and characterization of complex oxide thin films and *in situ* nanoscale investigations of functional materials and structures.

1.4.1. First-authored papers

1. **H. Nili**, S. Walia, M. Bhaskaran, S. Sriram, "Nanoscale Electro-Mechanical Dynamics of Nano Crystalline Platinum Thin Films: An *In Situ* Electrical Nanoindentation Study", ***Journal of Applied Physics*** in press (2014).

2. **H. Nili**, S. Walia, S. Balendhran, D. B. Strukov, M. Bhaskaran, S. Sriram, "Nanoscale Resistive Switching in Amorphous Perovskite Oxide (*a*-$SrTiO_3$) Memristors", ***Advanced Functional Materials*** DOI: 10.1002/adfm.201401278 (2014).

3. **H. Nili**, A. Esmaielzadeh Kandjani, J. Du Plessis, V. Bansal, K. Kalantar-zadeh, S. Sriram and M. Bhaskaran, "Alkali Ratio Control for Lead-Free Piezoelectric Thin Films utilizing Elemental Diffusivities in RF Plasma", ***CrystEngComm*** 15 7222 (2013).

4. **H. Nili**, G. Cheng, T. A. Venkatesh, S. Sriram, and M. Bhaskaran, "Correlation between Nano-Mechanical and Piezoelectric Properties of Thin Films: An Experimental and Finite Element Study", ***Materials Letters*** 90 148 (2013).

5. **H. Nili**, K. Kalantar-zadeh, M. Bhaskaran, and S. Sriram, "*In situ* nanoindentation: Probing nanoscale multifunctionality", ***Progress in Materials Science*** 58 1 (2013).

1.4.2. Co-authored papers

6. S. Balendhran, S. Walia, **H. Nili,** S. Sriram, M. Bhaskaran, “Elemental Analogues of Graphene: Silicene, Germanene, Stanene and Phosphorene”, ***Small*** DOI: smll.201402041 (2014).

7. S. Balendhran, S. Walia, **H. Nili**, J. Z. Ou, S. Zhuiykov, R. B. Kaner, S. Sriram, M. Bhaskaran, and K. Kalantar-zadeh, “Two-dimensional molybdenum trioxide and dichalcogenides,” ***Advanced Functional Materials*** 23 3952 (2013).

8. S. Walia, S. Balendhran, **H. Nili,** S. Zhuiykov, G. Rosengarten, Q. H. Wang, M. Bhaskaran, S. Sriram, M. S. Strano, K. Kalantar-zadeh, “Thermoelectric properties of transition metal oxides”, ***Progress in Materials Science*** 58 1443 (2013).

9. P. Gutruf, C. M. Shah, S. Walia, **H. Nili**, A. S. Zoolfakar, C. Karnutsch, K. Kalantar-zadeh, S. Sriram, M. Bhaskaran, “Transparent functional oxide stretchable electronics: micro-tectonics enabled high strain electrodes’, ***NPG Asia Materials*** 5 e62 (2013).

10. R. Abdul Rani, A. Zoolfakar, J. Z. Ou, R. Ab. Kadir, **H. Nili**, K. Latham, S. Sriram, M. Bhaskaran, S. Zhuiykov, R. Kaner, K. Kalantar-zadeh, “Impurity-Driven Defect States in Nanoporous Anodized Nb_2O_5 Photoanodes” ***Chemical Communications*** 49 6349 (2013)

CHAPTER 2

LITERATURE REVIEW

2.1. Perovskite Oxides: Technological Relevance

The research into oxide nano-electronics has recently gained traction as a serious contender for enabling ongoing advancement in information processing and data storage capabilities beyond conventional CMOS scaling. The advances in understanding the fundamental principles of complex electronic structure, phase transitions and interfacial properties of correlated oxide systems can enable novel electronics and photonics devices relying on the plethora of functional properties embedded in such systems [2.1-8].

Transition metal oxides are a fascinating class of functional oxides exhibiting a large range of functional properties as well as an intrinsic flexibility for structural and compositional engineering [2.3,5,7,9-12]. Multiple stable oxidization states of the transition metal oxides and the drastic changes in the crystal and electronic band structures as a result of local or distributed changes in the valence states, provide a vast materials design and engineering landscape for direct manipulation of the transition metal-oxygen functional units [2.3,4,9,10]. Among these, perovskite oxides of the ABO_3 crystal structure (Figure 2.1) possess a unique functional unit, the BO_6 oxygen octahedral structure [2.3,13],

which provides a large degree of freedom for application specific materials engineering. Functional properties of perovskite oxides range from superconductivity [2.14,15] and ferro/piezoelectricity [2.16-20], to novel oxide-based ultrafast memories and low-power electronics and optical devices [2.7,21-25].

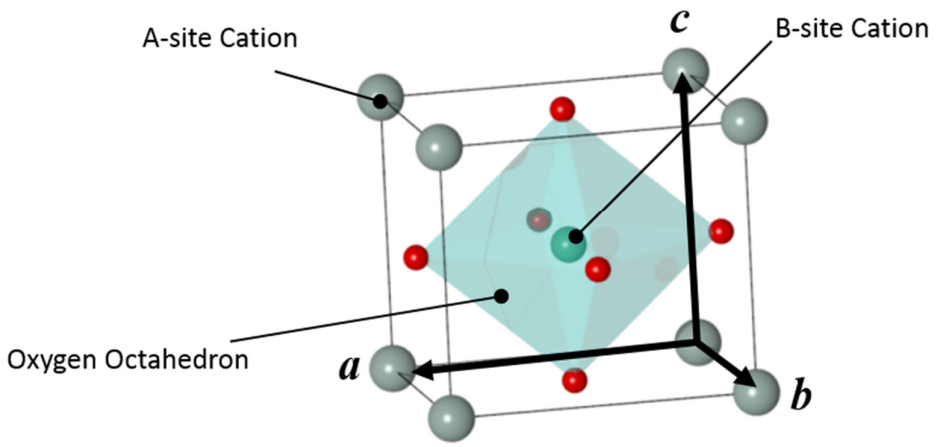

Figure 2.1. Schematic of a typical cubic perovskite oxide structure

As such, perovskite oxides have been the topic of rigorous research in the past couple of decades. With the emergence of novel oxide electronics, intensified research focus on perovskite oxides has made great strides in understanding the physical principles governing their structural properties and materials engineering for high performance nanoscale devices and systems [2.4,5,8-10,13].

2.1.1. Potassium sodium niobate ($K_xNa_{1-x}NbO_3$: KNN) perovskite oxide system: lead-free ferro/piezoelectrics

Potassium sodium niobate (KNN) is one of the most promising candidates for substituting lead-based ferro/piezoelectrics [2.19,26-28]. Besides having a high

electromechanical coupling factor [2.29] (comparable to commercially available lead-based PZT4), its high Curie temperature, high chemical inertness and biocompatibility, make it a promising candidate for environmentally friendly and bio-compatible sensor/actuator and energy harvesting applications [2.30-34]. The complex perovskite structure of KNN is a mixed system of ferroelectric potassium niobate ($KNbO_3$: KN) and anti-ferroelectric sodium niobate ($NaNbO_3$: NN) both with orthorhombic crystal structures (Figure 2.2) [2.35-38].

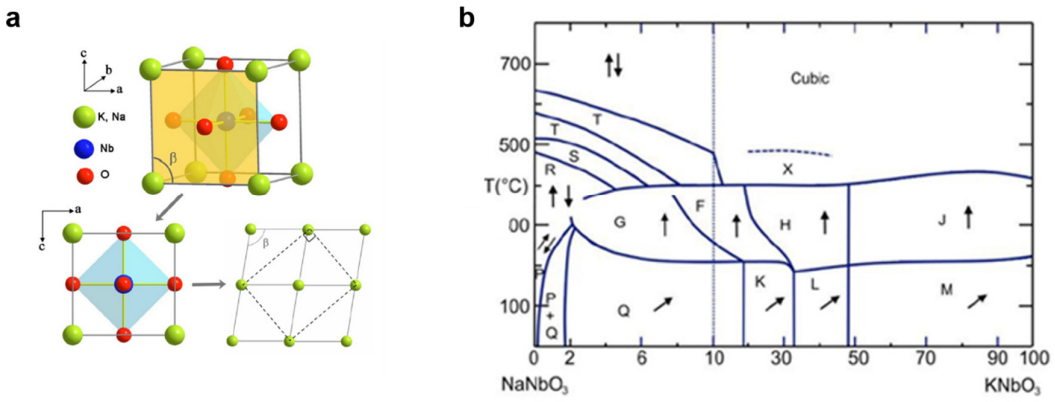

Figure 2.2. (a) Crystal structure and **(b)** phase diagram of $K_xNa_{1-x}NbO_3$ complex perovskite system. Regions labelled Q, K, and L are monoclinic ferroelectric, M, G are orthorhombic ferroelectric; F, H and J are tetragonal ferroelectric. Region P is orthorhombic antiferroelectric [2.39]

The anti-ferroelectric NN transitions to a ferroelectric phase (region Q in Figure 2.2b) with a small percentage of KN substitution. Besides several thermally induced phase transitions [2.35,36], several phase transitions and morphotropic phase boundaries (MPBs) exist at room temperature (at 17.5%, 32.5% and 47.5% NN content) [2.37]. Of particular interest is the MPB at 47.5%, where KNN exhibits its highest electromechanical coupling coefficients [2.17,40-42]. The main setback in commercializing KNN-based ferro/piezoelectrics is the

volatility of alkali metal compounds which results in poor quality of KNN ceramics and thin films [2.40,43]. A brief review on the status of synthesis and fabrication of KNN-based oxides is presented in Chapter 3.

2.1.2. Strontium titanate ($SrTiO_3$: STO): the archetypical perovskite oxide

Strontium titanate ($SrTiO_3$: STO) is the prototypical perovskite oxide with a cubic crystal unit at room temperature [2.44]. In its pristine single crystal form, STO is a high-k dielectric with superior temperature stability, commonly used as a gate oxide or the template substrate for oxide electronics applications. Relatively facile manipulations of structural and compositional characteristics of STO structure on the other hand, reveal its true promise. STO ceramics, thin films and interfaces can be engineered to exhibit a wide range of functional properties, from colossal magnetoresistance [2.45-47], metal-insulator transitions [2.48] and superconductivity [2.49,50] to two-dimensional electron gases [2.8], ferroelectricity [2.51], photoluminescence [2.52] and resistive switching [2.7,25,44,47,53]. As such, STO is sometimes compared to silicon as the foundation of oxide electronics [2.8]. From an interface engineering point of view, the distortion in the perovskite lattice *via* strain and phase engineering, layer thickness and defect structure control can be effectively used as a means to control the interfacial properties of STO [2.3]. Moreover, the compositional control of the STO structure enables direct control over the electronic structure as well as the defect chemistry of the material. Small scale donor (e.g niobium) [2.54,55] or acceptor (e.g. iron) [2.47] doping of STO is known to drastically change its electronic and energy band structures. STO also has a tendency of oxygen vacancy self-doping (i.e. oxygen exchange reaction) subject to external

stimuli (e.g. ion irradiation [2.52], electric field [2.56] and temperature), acting as native n-type dopants. The control over the concentration and equilibrium arrangement of these native dopants enables the control over electrical/electronic transport characteristics and optoelectronic properties of STO. Overviews of the functionalization techniques for the STO system are presented in Chapters 3, 4 and 5 in relevant sections.

2.2. Memristive Devices and Systems

The term “memristor” refers to circuit components capable of retaining an internal resistance state subject to the history of applied electrical field [2.1,57]. Memristors have been initially proposed by Chua *et al.* based on circuit symmetry arguments [2.58,59] as the fourth fundamental circuit component linking the charge (q) and flux (φ), namely:

$$d\varphi = Mdq \qquad (1)$$

In 2008 Strukov *et al.* [2.60] used a simple phenomenological model to demonstrate that memristivity can be described naturally, in nanoscale systems with coupled ionic-electronic carrier transport characteristics. They defined a charge-dependent state variable, w, which is subject to the history of charge-carrier distribution in the solid-state device, for the resistance of a memristive element:

$$M(q) = R_{OFF}\left(1 - \frac{\mu_V R_{ON}}{D^2}\right) q(t) \quad (2)$$

Where $M(q)$ is the charge-dependent memristance, R_{OFF} and R_{ON} are the resistance values in the device’s ON and OFF states (namely, the charge

carrier distributions that contribute to an either higher or lower resistance), D is the length of the solid-state device and μ_V is the average ionic mobility. The ionic mobility is an inherently field-dependent property in solid-state coupled ionic-electronic conductors such as metal-oxide-metal two terminal devices [2.61]. Moreover, this field dependency at extreme electrical fields (>1 MV/cm) commonplace in devices with thicknesses of a few tens of nanometers is proven to have a non-linear exponential-type characteristics [2.61,62]. This essentially means that coupled ionic-electronic devices operating under such conditions have the potential to exhibit extremely small memristive response times (< 10 ns) and large memristive state retention times (in the scale of years). This is signified by the equation [2.61]:

$$\tau_{store}/\tau_{write} \sim L/2a \times \exp(E/E_0) \qquad (3)$$

Where τ_{store} and τ_{write} are the retention and response time respectively, *L* is the active device region (in other words, the ionic diffusion length), *a* is the periodicity in an ideal ionic crystal, E is the applied electrical field and $E_0 = 2k_BT/qa$ is the characteristic field for a particular mobile atom in the crystal.

As such, memristive devices have the potential for integration in novel ultra high-density computing technologies. The immediate application for memristive devices is resistive random access memories (RRAMs) [2.1,6,63]. However the dynamic non-linear hysteretic behavior of these devices suggests applications in alternative computer logic architectures, multi-state logic and neuromorphic computational systems [2.1,57]. The typical device configuration for memristive devices in such applications, is a two terminal capacitive-type

metal-insulator (ion conductor)-metal (MIM) structure (Figure 2.3). This configuration is ideal for the high-density integration of memristive devices in cross-bar arrays in hybrid CMOS-based circuits. The device operates as an electronic switch in one of the two main resistance states (ON/OFF states) based on the history of the applied electrical field. These MIM structures are the focus of the investigation carried out throughout the course of the PhD project.

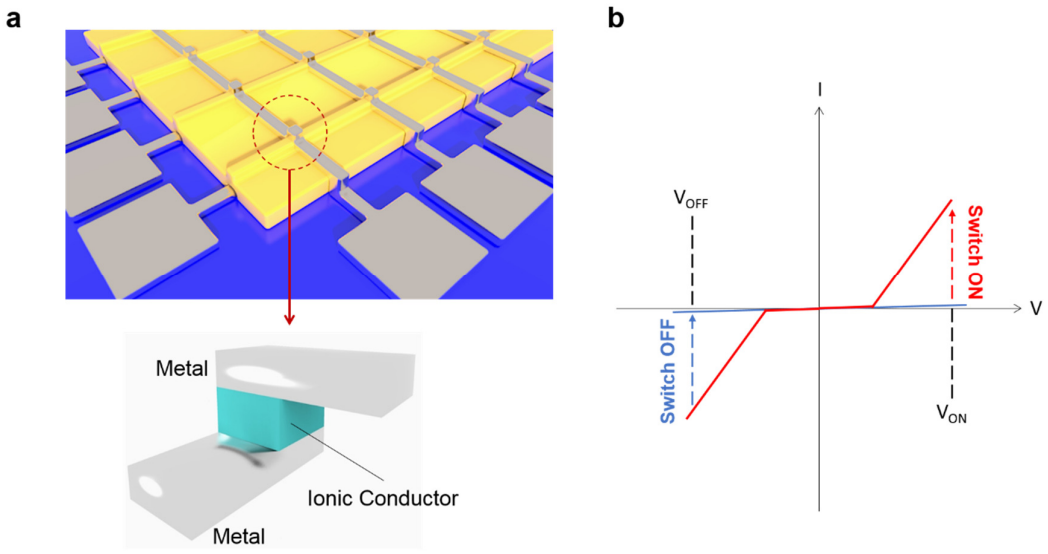

Figure 2.3. (a) Schematic representation of a cross-bar structure for memory and logic applications (the arrow points to the structure of a single memristive device). **(b)** Typical bipolar I-V characteristic of a memristive device as a resistive switch.

2.2.1. Resistive switching mechanisms and memristive materials

Memristive devices can be categorized based on the switching mechanism, switching materials and switching behavior. With regards to switching mechanisms, a large variety of physical effects can induce non-volatile resistive switching in a variety of functional materials [2.1,7]. Waser *et al.* have

summarized the physical mechanism known to cause non-volatile resistive switching effects (Figure 2.4) in their excellent review [2.7]. As for the switching materials, although many materials including solid amorphous electrolytes are known to exhibit variations of non-volatile resistive switching, the focus of this thesis is on the switching performance of transition metal oxides, in particular STO-based perovskite oxides. As a result, this brief overview is focused on the switching mechanisms in transition metal oxides.

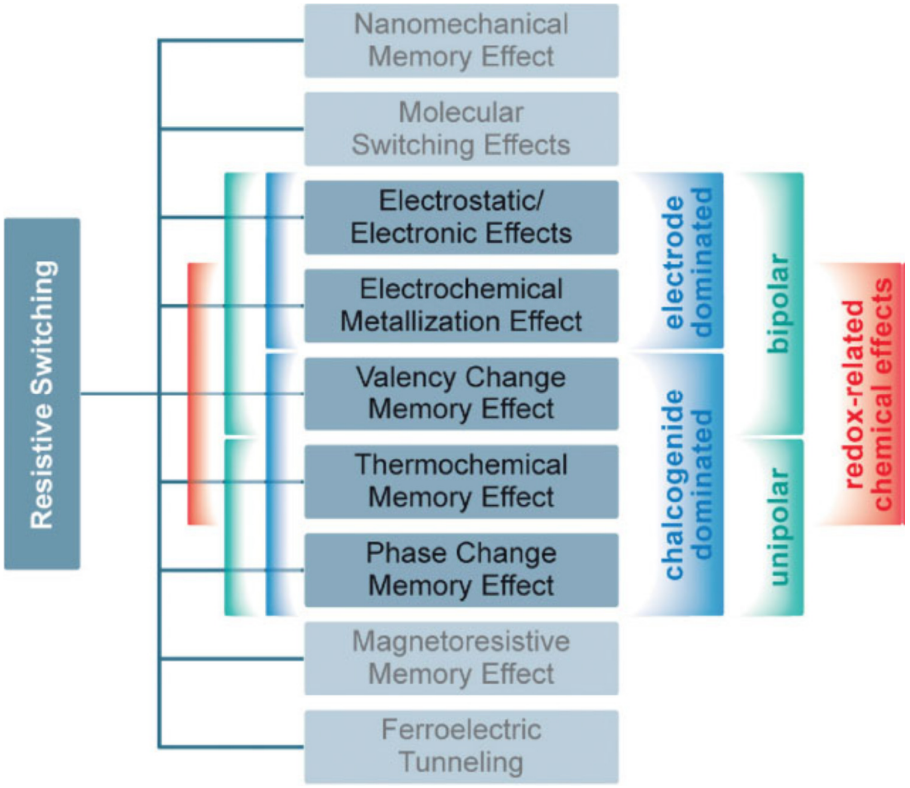

Figure 2.4. Classification of the physical resistive switching phenomena. Reproduced with permission from [2.7]. Copyright © 2009 WILEY-VCH Verlag GmbH & Co. KGaA, Weinheim

The resistive switching phenomena in most binary and complex transition metal oxides in MIM structures are largely considered to be originating from anionic

transport mechanisms [2.1,7]. From a defect chemistry point of view, the movement of anions through the defect structure of transition metal oxides can be described as a valence change mechanism [2.7]. In many transition metal oxides, these anionic species are oxygen ion related defects, i.e. oxygen vacancies, which exhibit high mobilities subject to extreme electrical fields. Local enrichment or depletion of mobile oxygen vacancies changes the current transport characteristics of the oxide layer. The switching behavior in this category of devices is a bipolar *I-V* switching characteristics (Figure 2.3b) resulting from field-dependent distribution of anionic species (oxygen vacancies). Since the movement of oxygen vacancies along the oxide network will lead to local changes in the valence states of the metallic cations, the resulting switching mechanism is regarded to as the valence change mechanism (VCM).

Other types of switching dynamics and mechanisms are highlighted in a recent comprehensive review by Yang *et al.* [2.1].

2.2.2. Resistive switching in $SrTiO_3$ and STO-based devices

Strontium titanate (STO) has been widely studied for its electronic and resistive switching properties [2.7,24,44,47,64-68]. It is a model perovskite system for the study of oxygen vacancy related defect structures and lattice disorders in transition metal oxides [2.56,66,69-74]. The crystal structure of STO be viewed as two inter-connected SrO and TiO_2 sublattices, where TiO_2 sublattice can be easily reduced and distorted in order to change the electronic band structure and electrical conductivity of the perovskite structure [2.7,75].

Because of its ability to harbor large concentrations of mobile oxygen vacancy charge carrier species, STO is considered to be a potent material system for resistive switching devices. The order and configuration of the vacancy related point and line defect structures are such that even in its un-doped single crystalline form, STO is capable of exhibiting resistive switching behavior. Such behavior can happen at very small scales upon introduction of oxygen vacancy related defect structures *via* temperature or electrical stress. In 2006, *Szot et al.* demonstrated resistive switching in thermally or electrically reduced individual dislocations in a STO single crystal [2.44]. The oxygen vacancy related extended defect structures in STO, act as filamentary pathways for current transport and enable the fast transport of electronic charge carriers (Figure 2.5).

These filamentary pathways typically consist of a partially reduced network in the TiO_2 sublattice along which the valance change mechanisms takes place [2.7,44,76].

In the MIM configuration, STO-based thin films of thicknesses around 100 nm are usually highly insulating in the virgin state and typically require a current-limited electroforming step to exhibit resistive switching [2.24,67,76,77]. The electroforming step creates extended oxygen vacancy defect structures along the thickness of the perovskite oxide, acting as switchable conductive filamentary pathways between the two metal electrodes. A simplified picture of the electroforming process can be described as follows. In a virgin MIM cell, the distribution of vacancy point defects is equilibrated over time.

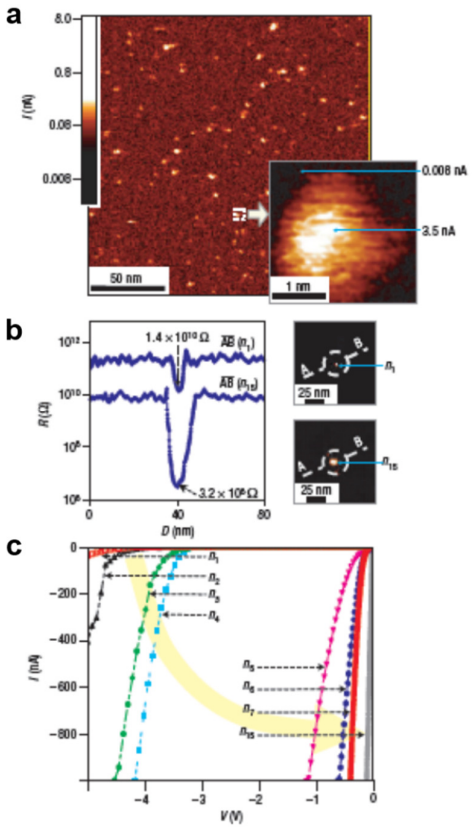

Figure 2.5. Electroformation and metallic conductance of individual dislocations. **(a)** A conductivity map of the surface of a $SrTiO_3$ single crystal as recorded by the LC-AFM. Filamentary paths with enhanced conductance are present on the surface after thermal reduction and re-oxidation under ambient conditions. Inset: spot with a dimension of 1–2 nm, where the main current is concentrated in a region corresponding to the size of the core of a typical edge-type dislocation. **(b)** Line scan across the selected spot (D denoting distance along AB) showing the dynamic range of the resistance change as a result of the application of a negative tip voltage bias, that is, selective electroformation. Right: Conductivity maps of the selected spot before (n1) and after electroformation (n15) with an increase in diameter at the surface from 5 to 10 nm. **(c)** I-V characteristics of a selected spot by sweeping the applied tip bias voltage between –5 and 0 V (0.3 s per cycle). The electroforming process during cycles 1-7 and 15 gives rise to a change from a nonlinear (n1–n7) to a linear (n15) behavior, which drives the filament from non-metallic to metallic conductance. Reproduced with permission form [2.44].

Since there is no conceivable direct conductive path between the two metal electrodes, the current transport characteristics of the MIM cell is governed by the interfaces between the metal electrodes and highly insulating oxide thin film [2.64,78,79]. If the metal electrodes are transparent to ionic partial current (i.e. they have a sufficiently low work function and are capable of exchanging oxygen bonds with STO oxide *via* localized redox reactions) the distribution of oxygen vacancies will not dramatically change upon applying small voltages [2.7,76]. On the other hand, if one or both electrodes are blocking to the ionic current, a pseudo-linear concentration gradient builds up based on the polarity of the applied bias and the disparity between the work functions of the metal electrodes (if the metal electrodes are of the same material or have a similar work function, then the gradient only depends on the polarity of the bias) [2.76]. The situation in higher biases changes dramatically based on the MIM structure and interfaces involved. Here for simplicity, a case of a simple MIM cell with dissimilar metal-oxide interfaces is considered (Figure 2.6). The concentration gradient is crucial for an ionic based resistive switching process to take place. This can be imposed during the electroforming process using the disparity between the metal-oxide interfaces or can be pre-existing in the oxide layer(s) (e.g. using double stacked layers of $SrTiO_{3-x}$ and $SrTiO_3$). Metal electrodes with different work functions can enhance the in-built vacancy concentration gradient and assist with the electroforming process. In the example structure of Figure 2.6a, a nominally stoichiometric STO oxide layer is sandwiched between a blocking Pt electrode with a high work function and a reactive Ti electrode with a lower comparative work function. The dissimilarity of electrodes work functions causes free carriers to flow from one material to the other until an

equilibrium state is established. Assuming that the charge-carrier concentration is low in the virgin STO thin film (i.e. the depletion-layer width exceeds the film thickness) the equilibrium Fermi level is determined only by the two metal electrodes and a simple flat band model can be proposed for the structure (assuming that the amount of trapped space charge is too low to cause band bendings) [2.64,78]. The mechanism of electroforming involves applying a high electrical stress by forward biasing one of the electrodes (the blocking electrode or anode of electroforming) to alter the concentration distribution of charged species (i.e. oxygen vacancies). Upon positive biasing the bottom electrode, the oxygen vacancies flow towards the opposite electrode (Transparent Ti electrode or cathode of electroforming) [2.7,76]. The increased concentration of the charge carriers at the cathode creates a strongly n-doped region at the vicinity of the cathode. The metal-oxide interface at the cathode ultimately breaks down at a critical concentration of oxygen vacancies thereby allowing the oxygen exchange reactions [2.80]. These reactions increase the width of the vacancy enhanced region creating a virtual cathodic region that propagates along the extended defect structures towards the anode [2.76]. The propagation stops in the vicinity of the forward biased blocking anode through limiting the current compliance. After the electroforming step is completed the width of the virtual cathode region can be controlled *via* applying biases of opposite polarities resulting in the bipolar switching behavior in electroformed STO-based cells [2.7,76]. Although the simplified electroforming and switching picture described for STO-based device is accurate to a large degree, the atomistic mechanisms and inter-correlations of the lattice defect structure, as well as optimization of the switching performance and ultimate compatibility and scalability of

STO-based devices are still not very well established and are subject to ongoing research.

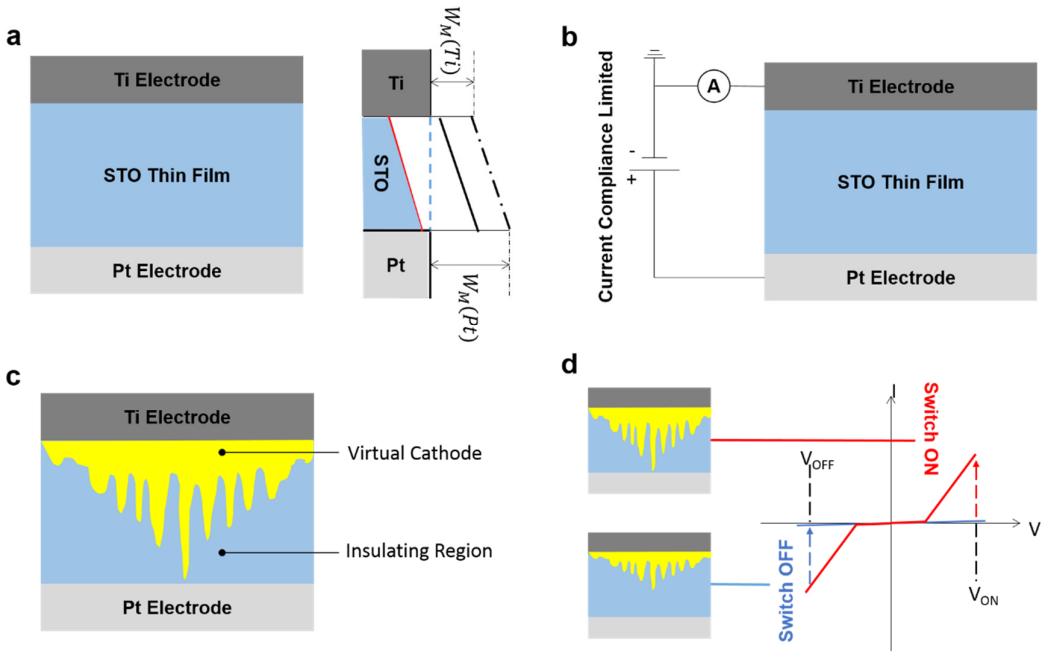

Figure 2.6. (a) The configuration and band structure of a STO-based MIM cell. **(b)** The electroforming procedure by applying a bias to the blocking (anode) electrode. **(c)** An electroformed STO-based MIM cell. **(d)** Switching the cell to ON (Low Resistance State) and OFF (High Resistance State) by extending and shrinking the virtual cathode region.

2.3. *In situ* Nanoindentation: Characterization of Nanoscale Multifunctionality

Nanoscale characterization techniques are continuously challenged by the rapid progress in nanostructures and functional materials demanding higher resolutions and advanced measurement techniques for mechanical, chemical, electrical, and thermal characterization. Numerous techniques have been developed over the years for the characterization of materials at nanoscale, the most notable of which are electron microscopy [2.81-86], scanning probe or

atomic force microscopy [2.87-95], X-ray imaging [2.83,85,96-101], and nanoindentation [2.102,103].

Amongst the wide variety of characterization techniques, nanoindentation is the most rigorous approach for quantitative characterization of nanoscale mechanical properties of materials (bulk and thin film form) [2.102,103]. The information gained from nanoindentation experiment is typically used to determine the Young's modulus and hardness of a material in the most basic form; however, this information can also be used to understand formation and propagation of mechanically-induced dislocations and defects. The study of the nanoindentation response of materials in combination with real-time imaging, heating, and/or electrical measurements *in situ* can create a broader understanding of the behavior of materials at the nanoscale. This understanding will be valuable in supporting the impetus to harness multifunctionality of materials to realize smart nano- and micro-devices.

2.3.1. *In situ* electrical nanoindentation

In the case of semiconductors, piezoelectrics, and other materials used in microelectromechanical systems (MEMS) and semiconductors industry, electrical properties and responses during stress and/or strain are of particular interest. *Ex situ* and post-mortem characterization techniques cannot provide real-time insight into the deformation mechanisms of materials, and more importantly, they cannot be employed to evaluate the electrical response of the materials to the applied force, which is of particular interest. To this end, nanoindentation combined with *in situ* electrical characterization has proven to be a powerful tool. Moreover, it can also provide additional detail during

indentation experiments. For instance, Fang *et al.* [2.104] reported an *in situ* electrical characterization technique to continuously measure the contact area between the indenter and sample using the absolute area between *I*–*V* curves continuously recorded during nanoindentation experiments.

In general, the electrical characterization during nanoindentation is performed using a conductive nanoindenter tip and a current/voltage source. Various techniques have been developed allowing a time-based correlation between load–displacement and electrical characterization data [2.105].

(i) Semiconductor transformations and properties

Silicon is the workhorse of the immense semiconductor industry, and its mechanical and electrical properties are of great interest. While the electrical and chemical properties of silicon are relatively well understood, its mechanical properties and dependence of electrical properties on mechanical stimuli are not well known, especially at the nanoscale. This has motivated extensive research in this area over the last decade and various *in situ* electrical characterization techniques have been developed to address the deformation mechanisms, phase transformations, and electrical response of silicon (and other semiconductors) under an applied force. Other semiconductors which have been studied using this technique include germanium and gallium arsenide (GaAs).

Clarke *et al.* [2.106] reported on the nanoindentation-induced amorphization of single crystal silicon and germanium. The current was monitored as a function of the applied voltage during indentation and behavioral changes from Schottky (diode-like) through to ohmic (resistor-like) and reversal to Schottky was studied

during loading and unloading. Pharr *et al.* [2.107] investigated phase transformations in silicon and germanium by studying the electrical resistance of metal contacts on these substrates during nanoindentation. It was indicated that changes in resistance observed were due to the interface of the metal to semiconductor rather contributions from the bulk semiconductor.

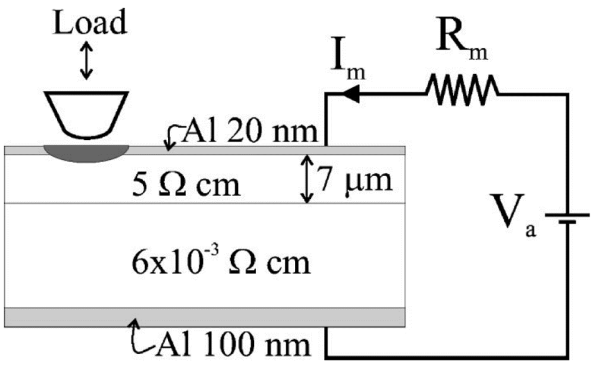

Figure 2.7. Schematic of experimental setup for *in situ* electrical nanoindentation of silicon. The silicon structure consists of an epilayer on low resistance silicon. Aluminum was evaporated onto both sides and a closed circuit for current measurement was created. (Figure reproduced from Ref. [2.108].)

Bradby *et al.* [2.108] introduced a quantifiable and highly sensitive *in situ* electrical characterization technique to investigate the deformation behavior and phase transformations of crystalline silicon during nanoindentation. In this study, a silicon epilayer was probed during nanoindentation, allowing the measurement of the current through a reverse-biased Schottky diode formed by the configuration which would turn to an ohmic contact following the formation of a pressure-induced metallic Si-II phase under the indenter (Figure 2.7). As this configuration was particularly sensitive to the Si-I to Si-II phase transformation, it proved useful in detecting such changes and correlating them with load–displacement data acquired from nanoindentation tests. Further,

phase transformations to either low pressure Si-III/Si-XII or amorphous-Si phases were identified from the current measurements during unloading, with the formation or nucleation of such phases depending on the unloading rate.

Given the sensitivity of this *in situ* electrical nanoindentation technique in detecting silicon phase transformations, the same group developed methods for *in situ* electrical measurements using a doped diamond indenter tip. The doped diamond tips utilize the hardness to diamond to expand the range of materials that electrical nanoindentation can be applied to. This was utilized to further investigate phase transformations of crystalline silicon under high pressure [2.109,110]. In Ruffell *et al.* [2.109], information from post-indent *I–V* curves and previous TEM and Raman spectroscopy measurements were correlated with the electrical behavior and phase transformations during nano indentation. Measurements of current flowing through the nanoindenter tip and sample during an indentation cycle was carried out (associated with load/unload curve), with a constant voltage applied [2.110]. This allows the system to be extremely sensitive to conductivity changes in the material below the indenter tip and also allows voltage monitoring throughout the loading and unloading cycle (Figure 2.8). A further development to this technique was reported by Fujisawa *et al.* [2.111] which consisted of combining cyclic loading with electrical measurements to monitor phase transformations during unloading. Changes in mechanical behavior and electrical conductivity were monitored and the phase transformation changes were verified using TEM data. Another novel approach to investigate the evolution of metastable Si-II metallic phase of crystalline Si during nanoindentation with a high spatial resolution employed *in situ* scanning spreading resistance microscopy (SSRM).

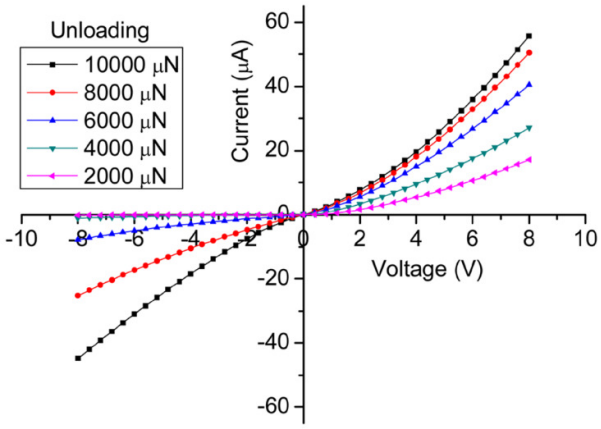

Figure 2.8. Current–voltage curves extracted during nanoindentation unloading highlighting sensitivity of *in situ* electrical nanoindentation in determining pressure-induced phase transformations. (Figure reproduced from Ref. [2.109].)

In this work [2.112], a diamond AFM probe was used for nanoindentation while a direct current (DC) bias was applied between a back contact on the back surface of the sample and AFM tip to realize a stable electrical contact. The resulting current was measured using a logarithmic current amplifier enabling the monitoring of electrical conductivity *vs.* applied force, and the detection of phase transformation by detecting a fall in resistivity. The experimental results were correlated with molecular dynamics simulation which predicted a new metastable phase of silicon Si-XIII when using a larger indenter tip. The relationship between indenter tip size, contact area, and phase transformations in silicon are also discussed [2.112].

An *in situ* electrical contact resistance measurement was introduced to monitor delamination of conductor–semiconductor specimens [2.113]. Measurements were carried out in *quasi*-static and oscillating loading modes on TiN thin films on steel. A pop-in event together with a current drop was identified as the detection signal for delamination occurring in both loading regimes.

In a nanoindentation study on GaAs, Nowak *et al.* [2.114] employed *in situ* electrical probing to simultaneously record mechanical and electrical response of an uncoated sample during the experiment. This study examined the pop-in events previously reported for GaAs, which were indicated by discontinuities in the load-displacement curves. During the experiments, an electrical current spike was generated in direct relation to the mechanical pop-in event in the load–displacement curve. This sharp increase in current suggested the occurrence of a pressure-induced phase transformation in GaAs, in contrast with previous assumptions about the onset of plasticity in GaAs.

(ii) Piezoelectric properties and energy harvesting

The need to characterize the electromechanical properties of piezoelectric and ferroelectric materials has served as a driving force in developing nanoscale probing techniques that combine mechanical stimuli with electrical measurements, and *vice versa*. Nanoindentation has been used to characterize both piezoelectric bulk materials and thin films, with the early *in situ* electrical experiments relying on significant modification of instrumentation.

The initial studies provided a theoretical background for employing indentation techniques with electrical measurements for the characterization of piezoelectric materials [2.115,116]. Sridhar *et al.* [2.116] also carried out experimental characterization with *in situ* electrical measurements to study mechanical and electrical responses of piezoelectric bulk materials (commercial lead zirconate titanate PZT-4 and barium titanate $BaTiO_3$). This study was performed using a conductive and electrically grounded spherical indenter tip, with an electrometer connected between the indenter and ground to measure the *quasi*-static current

induced in the sample. It was found that increasing indentation velocity (loading rate) increased the current magnitude and switching the poling direction in the films under study reversed the polarity of the measured current. Indentation velocities up to 50 μm min^{-1} and a maximum load of 300 N were used. Similar experiments were carried out using a conical indenter tip by the same group which showed that after a certain load, inelastic deformation sets in and analytical predictions based on linear models no longer apply [2.117].

Algueró *et al.* [2.118] studied stress-induced depolarization in lanthanum-modified lead titanate thin films. The nanoindenter tip was used as the top electrode to pole the thin films by applying a field of 150 kV cm^{-1}. The depolarization current density under indentation was measured, and correlated with the movements of 90° domain walls. In another study by the same group, this force induced domain wall motion and ferroelectric switching was investigated further, this time for calcium-modified lead titanate thin films [2.119]. Ferroelectric hysteresis loops under indentation force were obtained using a tungsten carbide and cobalt (WC-Co) spherical indenter, also acting as an electrode to enable electrical measurements. Under applied mechanical force and voltage, the resulting current density and electric charge were evaluated using Hertzian theory. Their study revealed that mechanical stress prevents the ferroelectric hysteresis loops from becoming saturated. This hinders the ferroelectric switching process and results in large coercive fields (up to 400 kV cm^{-1}).

Koval *et al.* [2.120] investigated the electromechanical response of pure and Mn-doped PZT films of 700 and 70 nm thicknesses during nanoindentation. Stress-induced electrical current transients were measured *in situ via* the use of

an electrometer under a mechanical load applied by a spherical indenter. The conductive indenter tip was used as the top electrode while a Pt layer served as the bottom electrode as shown in Figure 2.9. Under the nanoindentation load, an electrical current which is the aggregate of intrinsic response and force-dependent extrinsic contribution of domain walls was measured. Their results showed a non-linear behavior in the electromechanical response of the thin films within the sub-coercive stress range.

A new approach for quantitative characterization of piezoelectric materials, referred to as piezoelectric nanoindentation (PNI), was reported with the use of an oscillating voltage applied across the sample under study [2.121]. In PNI, utilizing the oscillating voltage applied between the indenter and sample in a standard nanoindentation system with continuous stiffness measurement, the first harmonic of bias-induced surface area at the contact area is detected. Lead zirconate titanate (PZT) and barium titanate ($BaTiO_3$) ceramics were examined, and their piezoelectric constants were measured under the converse piezoelectric effect (applying a voltage and measuring resulting strain-induced displacement). These results provided a quantitative insight into the electromechanical response of piezoelectrics. Drawing on the developments reported by Koval *et al*. [2.120] and Rar *et al*. [2.121], quantitative measurement of the longitudinal piezoelectric coefficient of strontium-doped PZT (PSZT) thin films were carried out by Sriram *et al.* [2.122] by combining the accuracy of the nanoindenter for displacement measurement and the converse piezoelectric effect. The change in the thickness of thin films was monitored while applying an electric potential across the thickness of the film. Utilizing the mapping capabilities of the nanoindenter, the piezoelectric response of the thin films has

been studied over large areas to determine uniformity and possible correlation with microstructure [2.122,123]. This enabled the determination of the average piezoelectric response of the material, along with identifying maxima and minima.

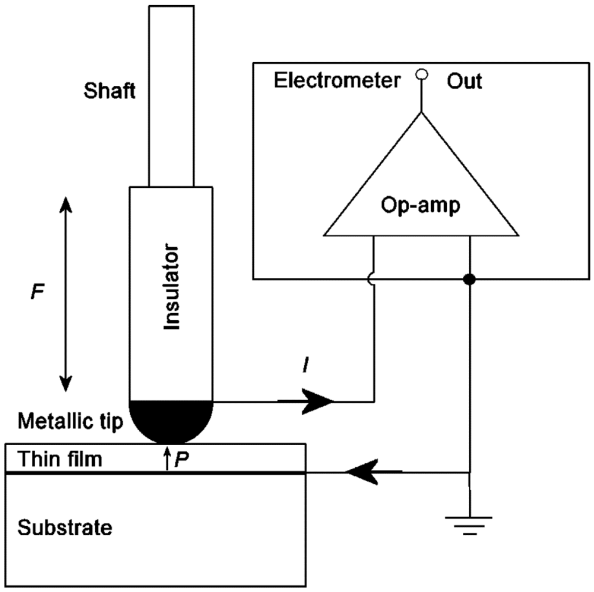

Figure 2.9. Schematic drawing of *in situ* electrical nanoindentation setup used to study electromechanical response of piezoelectric thin films. (Figure reproduced from Ref. [2.120].)

The piezoelectric response characterization was extended to the direct piezoelectric effect using a commercial *in situ* electrical nanoindentation instrument (Hysitron Triboindenter with NanoECR). In this work, controlled forces were applied to piezoelectric thin films and electron beam lithography defined piezoelectric nanoislands, as shown in Figure 2.10a and 2.10b [2.124]. These materials were tested with varying levels of force and loading rates to determine the open circuit voltage and short circuit current generation during nanoindentation (Fig. 2.10c). Measurements were done using impulse,

sustained, and staircase forces to investigate the response under the direct piezoelectric effect, with typical measurement results shown in Figs. 2.10d and 2,10e.

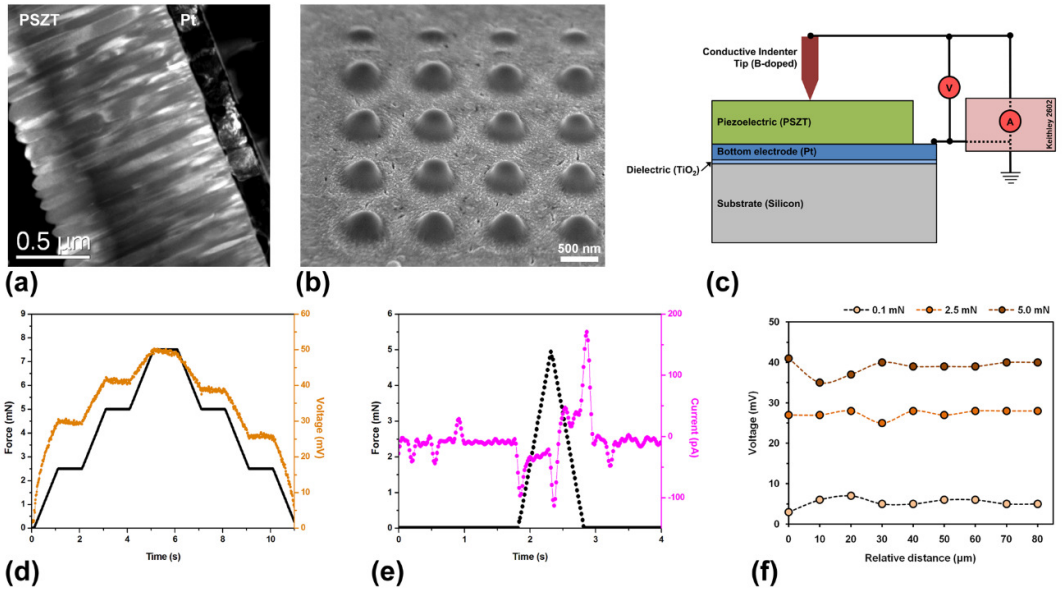

Figure 2.10. *In situ* electrical nanoindentation to characterize energy generation from piezoelectric materials. Electron micrographs of thin films and nanoislands are shown in **(a)** and **(b)**, respectively. Schematic of the electrical measurement arrangement is shown in **(c)**. Typical results for **(d)** voltage generation, **(e)** current generation, and **(f)** mapping voltage generation at different forces. (Figure adapted from Ref. [2.124].)

The programmable mapping capabilities of the nanoindenter again enabled the study of uniformity of voltage generation for different levels of force Figure 2.10f. Voltages of up to 40 mV and current transients of 200 pA were measured under a load of 5 mN, with estimated direct piezoelectric response coefficient in agreement with those measured under the converse effect. This study demonstrated the nanoscale electromechanical scientific insight that can be gained from *in situ* electrical nanoindentation, and provided quantitative

characterization of the energy generation capabilities of piezoelectric materials at the nanoscale.

CHAPTER 3

CONTROLLED PVD SYNTHESIS OF PEROVSKITE OXIDES

3.1. Composition, Phase and Structure Control of Lead-Free Piezoelectric $K_xNa_{1-x}NbO_3$ Perovskite Oxide Thin Films

Alkali-based potassium sodium niobate, $K_xNa_{1-x}NbO_3$ (KNN), material system is one of the most promising lead-free substitutes for the dominant ferroelectric lead zirconate titanate (PZT) system owing to its good piezoelectric properties, high Curie temperature, and modifiability by various dopants [3.1-4].

KNN-based thin films have been investigated extensively during the past ten years for applications ranging from optical waveguides [3.5,6] and FRAMs [3.7] to piezoelectric-based devices for energy harvesting applications [3.8-10]. KNN-based thin films have been processed by a variety of techniques encompassing chemical deposition such as sol-gel [3.11,12] and chemical solution deposition (CSD) [3.13,14], and physical deposition such as pulsed laser deposition (PLD) [3.3,15,16] and RF magnetron sputtering [3.5,7-10,17-

22]. Among these, RF magnetron sputtering is promising due to its capability for large area deposition with lower growth temperatures that makes it viable for integration with fabrication processes. Major challenges in RF magnetron sputtering of KNN-based thin films are non-stoichiometry due to volatility of alkali metals [3.18,23], formation of secondary phases [3.24], and high leakage current density [3.17,18].

The loss of alkali metals during KNN thin film synthesis was noted in early attempts of PLD and RF magnetron sputtering [3.17,23,25]. Further studies on the effects of different sputtering parameters on the composition, crystal structure, and growth rate of KNN thin films revealed that while crystalline phases and growth rates are largely dependent on sputtering pressure and growth temperature, alkali loss cannot be controlled by varying sputtering parameters [3.17,18,24]. It was suggested then that the alkali volatility can be addressed by excess amount of K and Na species (usually in the ratio of 1.5:1.5:1 for K:Na:Nb) in sputtering targets [3.23]. Most recently, Kim *et al.* [3.22] have studied the effect of post-annealing treatment on the crystal structure and electrical properties of KNN thin films grown on Pt/Ti/SiO_2/Si substrates at a substrate temperature of 300 ℃ utilizing a stoichiometric target, in different annealing atmospheres. A detailed study of the alkali loss and the compositional homogeneity of KNN thin films as a function of oxygen partial pressure during the sputtering process, offers the potential to control elemental diffusivity during deposition to tailor alkali content and composition ratios. This creates the opportunity to attain different alkali ratios from a single target and also create tailored deficiencies in films for ionic conduction for memristive applications.

In this section, the correlation between varying oxygen partial pressure during synthesis, and post-annealing treatment conditions on alkali loss and crystal structure of KNN thin films is studied. These insights are used to create a physical vapor deposition and post-annealing treatment protocol to control the stoichiometry and crystal structure of KNN thin films. The results of this investigation have been published in the journal of ***CrystEngComm*** [3.26]

3.1.1. Controlled RF-magnetron sputtering of KNN thin films

KNN thin films were deposited by RF-magnetron sputtering on platinized silicon substrates with a 200 nm thick platinum layer and a 20 nm thick titanium dioxide adhesion layer. A 100 mm diameter KNN target with the composition $(K_{0.3}Na_{0.7})NbO_3$ was used for all depositions. The composition of the target was verified using energy dispersive X-ray analysis (EDX) in a scanning electron microscope (SEM). To determine the role of elemental diffusivities on the resulting alkali ratio, the role of oxygen partial pressure during deposition and the effect of post-annealing in vacuum and gaseous atmosphere were investigated. The oxygen partial pressure in argon for the process gas during sputtering was varied from 0 to 40% in steps of 10% for each sputtering run.

KNN thin films were subsequently post-annealed at 700 °C for 1 and 3 hours in vacuum and in oxygen atmosphere to study the effects of post-annealing on their composition, surface chemistry, and crystal structure. Table 3.1 summarizes sputtering and post-annealing conditions.

Table 3.1. Sputtering and post-annealing conditions for KNN thin films

Substrate	$Pt/TiO_2/Si$
Target	$(K_{0.3}Na_{0.7})NbO_3$ [KNN30]
Process Gas	0, 10, 20, 40% oxygen in argon
Base pressure	1×10^{-7} Torr
Sputtering Pressure	5×10^{-3} Torr
Substrate Temperature	700 °C
RF Power	200 W
Sputtering Duration	3 h
Post-Annealing Treatment (at 700 °C)	1 and 3 h in vacuum 1 and 3 h in oxygen

3.1.2. Impact of the synthesis and post-annealing treatment conditions on the composition and crystal structure of KNN thin films

The composition and crystal structure of as-grown and post-annealed KNN thin films were studied using X-ray diffractometry (XRD) and X-ray photoelectron spectroscopy (XPS) depth profile analysis to identify the effects of synthesis parameters on the microstructure of KNN thin films. Figure 3.1 shows the X-ray diffractograms for as-deposited KNN thin films under different oxygen partial pressures. Peaks have been indexed using powder diffraction files for orthorhombic platinum silicide (PtSi – ICDD Card No. 07-0251) [3.27] and KNN monoclinic (ICDD Card No. 74-2025) [3.28] and tetragonal (ICDD Card No. 77-0037) [3.29] structures. At the high temperature range of KNN thin films deposition, the TiO_2 adhesion layer forms islands [3.30,31] providing contact between the substrate and the platinum layers and allowing the diffusion of the platinum layer into the silicon substrate [3.30]. The formation of TiO_2 islands and the contact between platinum and silicon layers during high temperature oxide sputtering deposition on $Pt/TiO_2/Si$ substrates have been previously

verified through TEM analysis [3.32]. Due to the high deposition temperature, the platinum bottom electrode has been morphed into a polycrystalline platinum silicide layer with a strong (200) orientation. Strong (200) orientation of the platinum silicide layer has resulted in the formation of (002) oriented KNN structure (peak at 2θ of 46.1°) [3.11]. Also, the KNN (101) peak at around 32.5° is observed. The differences in the relative intensity of the peak at around 32.5° between as-grown thin films deposited at different oxygen partial pressures is evidence of the existence of KNN (101) orientation in the films, which becomes more evident with results comparing the as-grown and post-annealed samples (discussed later).

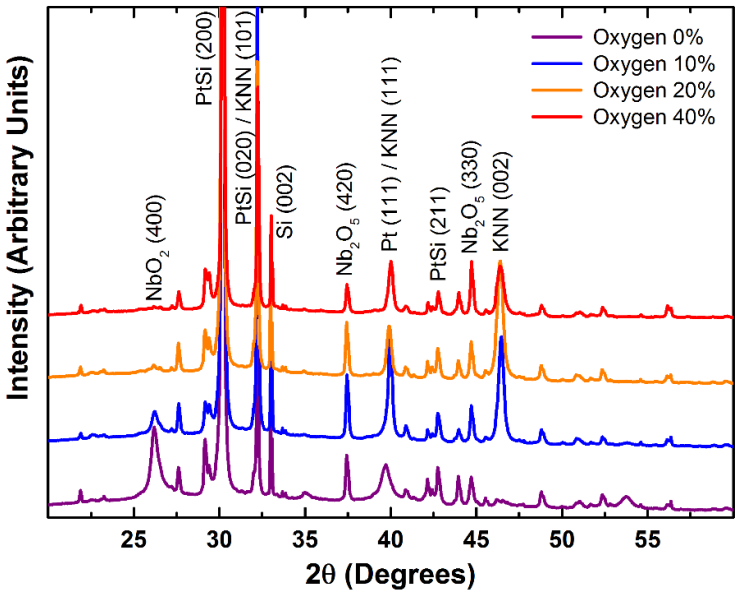

Figure 3.1. X-ray diffractograms for as-deposited KNN thin films. Depositions were performed at a substrate temperature of 700 °C, with varying oxygen partial pressure.

The appearance of secondary niobium oxide peaks in XRD can be primarily attributed to excess niobium compared to alkali metals in the films, resulting from the alkali loss during the RF magnetron sputtering with a stoichiometric target. To confirm niobium species indexed in the X-ray diffractograms and

study the effect of oxygen partial pressure and post-annealing treatments on the composition of the thin films, XPS depth profile analysis was conducted on the samples.

XPS elemental and depth profile analysis were carried out through the thickness of thin films to characterize elemental ratios variation of sodium, potassium, niobium, and oxygen as a function of oxygen partial pressure and post-annealing treatments, and to determine the compositional homogeneity of the KNN thin films. The elemental ratios for different species are uniform within tolerance levels throughout the thickness of all thin films, excluding the data acquired from the exposed surface of the films as it is subject to ambient contamination. Table 3.2 shows K/(K+Na) ratio for KNN thin films grown under different oxygen partial pressure conditions and subjected to various post-deposition treatments, highlighting the impact of process gas and post-annealing treatment on the alkali loss and ratio.

Table 3.2. K/(K+Na) ratio for KNN thin films grown under different oxygen partial pressure and subjected to various post-annealing treatments at 700 ℃. The K/(K+Na) ratio of the sputtering target used is 30%

Oxygen Partial Pressure (%)	K/(K+Na) Ratio (%)				
	As-Grown	1 h Vacuum	3 h Vacuum	1 h Oxygen	3 h Oxygen
0	89	78	73	83	78
10	32	39	17	42	43
20	41	44	44	42	44
40	41	40	50	43	42

A lack of oxygen in the sputtering atmosphere results in a dramatic loss of alkali species due to collisions with the argon ions in the RF plasma and thermal evaporation at the substrate end at high temperature. As a lighter element, sodium is more prone to the scattering mechanisms than potassium [3.33-35].

Thus, KNN phase was not observed in the XRD pattern of KNN films deposited in a pure argon atmosphere. The introduction of oxygen minimizes sodium loss, with the elemental ratios ranging from 31.7-41.3% (compared to the 30.0% for the target). Upon introduction of oxygen into the sputtering atmosphere, negative oxygen ions formed at the target surface get accelerated into the plasma towards the substrate. The highly-energetic oxygen ions enhance the scattering of the ablated perovskite species of the oxide target [3.36,37] which in turn leads to a decrease in the kinetic energy of the perovskite species. Since the sputtering species reach the substrate with a lower kinetic energy and surface mobility this leads to the formation of preferentially ordered grains with smaller sizes. Further, oxygen pressure helps the oxidization of the sputtered species into higher oxidization states leading to the formation of Nb^{5+} species for the perovskite crystal structure. Post-annealing treatments in most cases do not cause a significant change in the as-grown alkali ratio; however, slight increases observed in most cases indicate further sodium loss.

Table 3.3. (K+Na)/Nb ratio for KNN thin films grown under different oxygen partial pressure and subjected to various post-annealing treatments at 700 ℃. The (K+Na)/Nb ratio of the sputtering target used is 100%

Oxygen Partial Pressure (%)	(K+Na)/Nb Ratio (%)				
	As-Grown	1 h Vacuum	3 h Vacuum	1 h Oxygen	3 h Oxygen
0	10	9	14	15	20
10	45	27	56	50	53
20	37	33	39	52	44
40	28	25	33	43	40

The ratio of alkali to niobium concentration (K+Na)/Nb, which is expected to be 1 (or 100%), was also analyzed (see Table 3.3). The elevated loss of alkali metals in the sputtering process is observed in all films leading to alkali-to-

niobium ratios of 0.1-0.5 in the KNN thin films. This result supports reports [3.23] that a potential mechanism to compensate for alkali loss is to have excess alkali concentration in KNN oxide sputtering targets.

3.1.3. Stabilization of perovskite KNN chemical phase and crystal orientation through post-annealing treatments

In order to understand the underlying mechanism and chemical–crystallographic phase changes resulting from such alkali loss, detailed analysis of the XPS spectra for sodium, potassium, niobium and oxygen species in the KNN30 thin films was carried out.

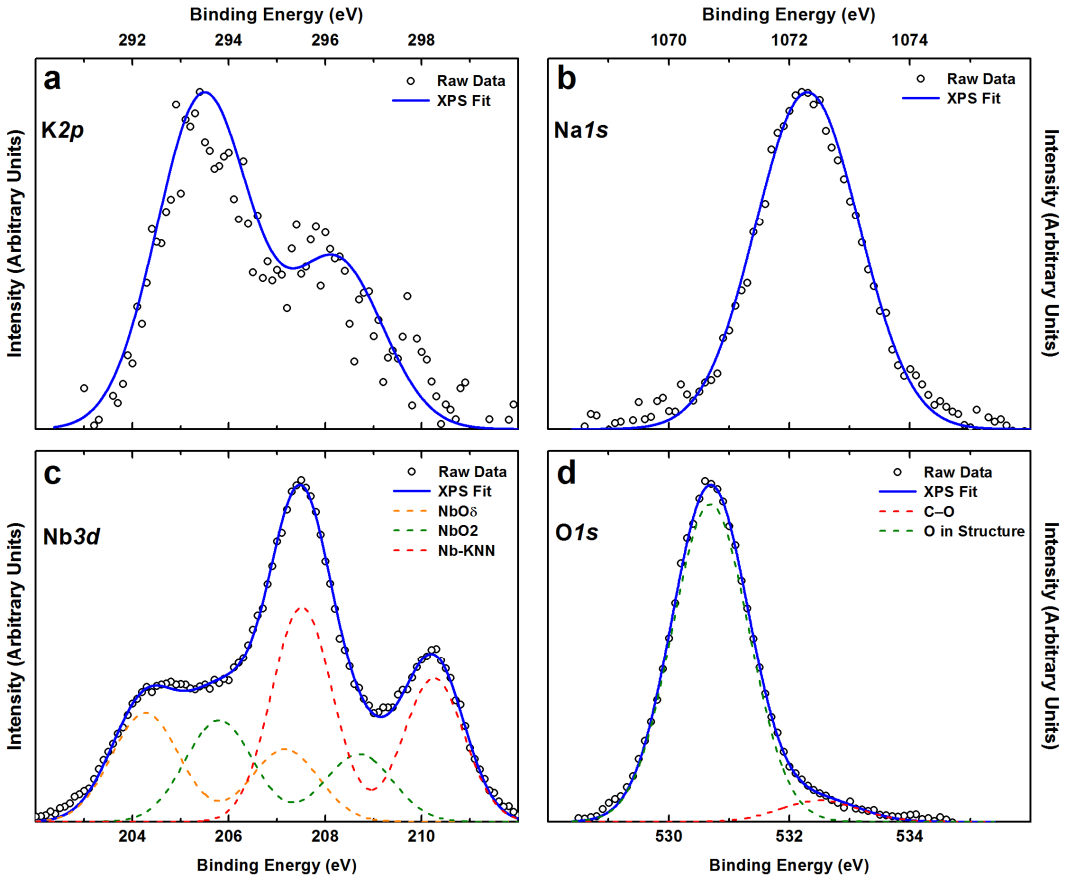

Figure 3.2. XPS spectra for **(a)** K*2p*, **(b)** Na*1s*, **(c)** Nb*3d*, and **(d)** O*1s* core levels for as-deposited KNN thin film grown under 20% oxygen partial pressure.

Figure 3.2 presents XPS spectra for these elements in the as-grown sample deposited under 20% oxygen partial pressure (chosen based on its preferential orientation, Fig. 3.1)

The results have been obtained after background correcting the as-obtained XPS spectra using Shirley algorithm [3.38], aligning the elemental binding energies to adventitious carbon (C*1s*) binding energy of 285 eV and resolving chemically distinct species using a non-linear least square fitting procedure [3.39].

Both potassium and sodium spectra were found to consist of a single component spectrum that can be correlated to KNN structure. Notably, as expected, K*2p* spectrum showed the spin orbital pair corresponding to $2p_{3/2}$ and $2p_{1/2}$. XPS spectrum for Nb*3d* shows three different spin orbital pairs, corresponding to three different niobium species: (i) NbO_{δ} where $1<\delta<2$ at 204.3 eV; (ii) NbO_2 at 205.8 eV; and (iii) Nb_2O_5 phase present in KNN (henceforth called Nb-KNN) at 207.7 eV [3.40,41]. Moreover, O*1s* spectrum could be de-convoluted into two components with binding energies at 530.7 eV and 532.5 eV [3.42], which correspond to O^{2-} ions in the structure of different niobium oxides, and the adventitious C–O bonds adsorbed on to the sample surface, respectively. Further, the effect of different post-annealing treatments on the composition of the thin films was examined by de-convoluting the Nb*3d* core level XPS spectra in corresponding spin orbital pairs. In as-grown samples and those post-annealed in vacuum for 1 h, NbO_{δ}, NbO_2, and Nb-KNN related peaks were all present. However, in the thin films annealed for 1 h in oxygen, the NbO_{δ} peak completely vanished and the peak related to KNN became

significantly more prominent than that of NbO_2 (based on the integrated peak area).

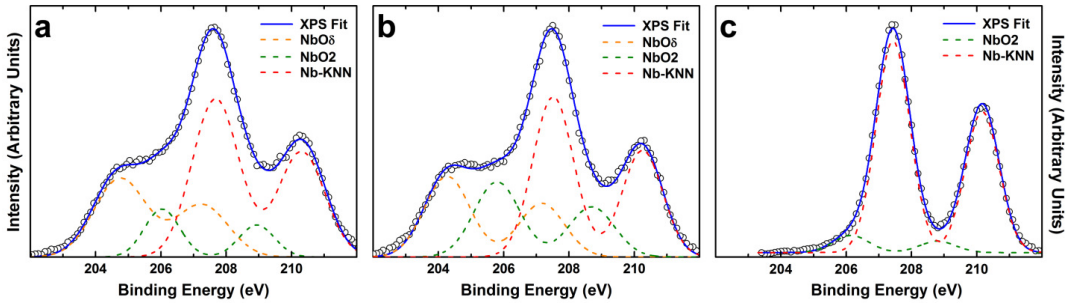

Figure 3.3. Nb*3d* spectra of the films grown under 20% oxygen partial pressure: **(a)** as-deposited, **(b)** post-annealed for 1 h in vacuum, and **(c)** post-annealed for 1 h in oxygen.

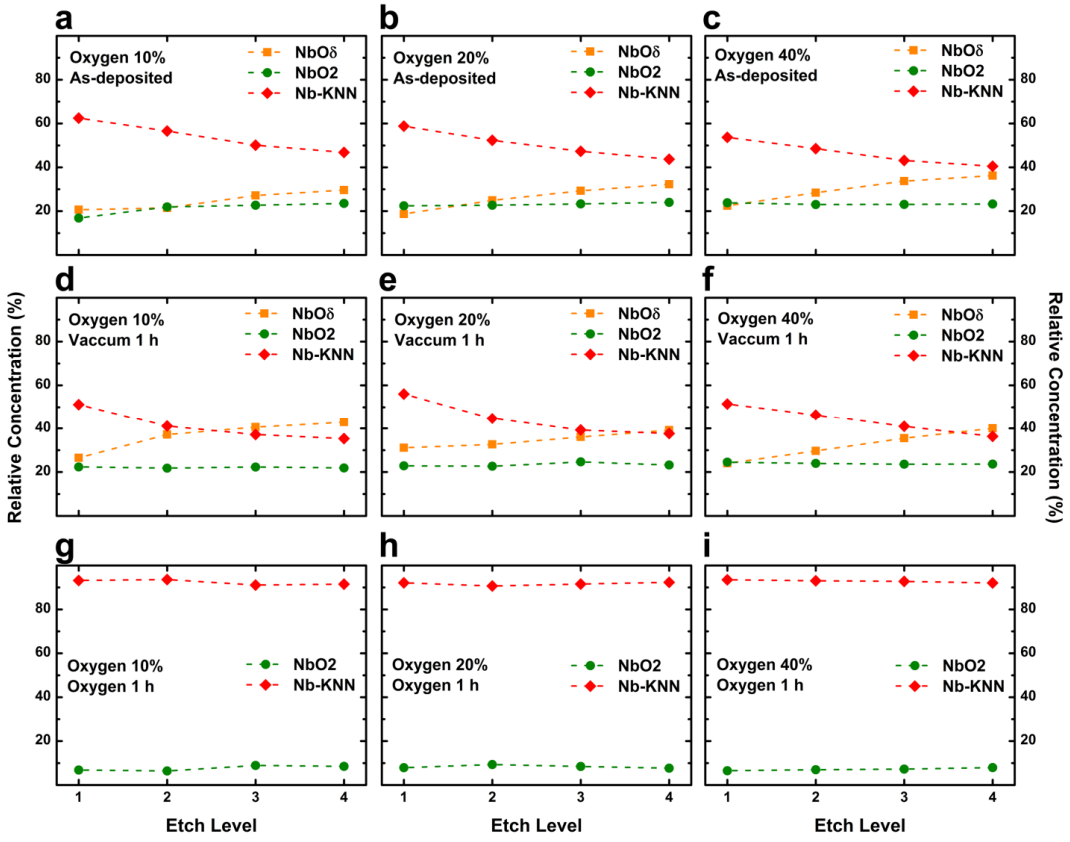

Figure 3.4. Relative percentage concentrations of the NbO_δ, NbO_2, and Nb-KNN species at consecutive etching levels of the KNN thin films studied **(a,b,c)** as-deposited and subjected to post-annealing treatment in **(d,e,f)** vacuum for 1 h and **(g,h,i)** oxygen for 1 h and grown with **(a,d,g)** 10%, **(b,e,h)** 20%, and **(c,f,i)** 40% oxygen partial pressure.

This indicates that the annealing in an oxygen environment for a sufficient amount of time increases the tendency of Nb to oxidize towards higher oxidation states, desirable for attaining the Nb_2O_5 state required for KNN. Figure 3.3 shows the evolution of Nb*3d* peak for the film grown under 20% oxygen partial pressure as a result of post-annealing treatments. XPS spectra of Nb*3d* through the thickness of films were also used to determine the uniformity of oxidation levels at different thickness levels of the sample. The films deposited under 10%, 20%, and 40% oxygen partial pressures were studied. Figure 3.4 shows the relative concentration of the three different Nb species at four different depths within the film (based on four consecutive etch cycles).

The concentration of the Nb-KNN species (as opposed to Nb species in oxides) decreases through the depth of films post-annealed in vacuum irrespective of the oxygen partial pressure during the sputter deposition process. This phenomenon can be attributed to the lack of oxygen during annealing which prevents Nb from attaining a more stable higher oxidation state, as desirable for KNN. Also, the amount of NbO_2 is relatively uniform (about 20%) at different etch levels. This indicates that limited oxygen was available at greater depths in the film, resulting in the dominance of the sub-stoichiometric NbO_δ species. On the other hand, films post-annealed for 1 h in oxygen exhibit considerably higher Nb^{5+} species almost uniformly throughout the thickness. This indicates that post-annealing in oxygen atmosphere enables oxygen diffusion through the film thickness, promoting Nb^{5+} oxidation states (Nb-KNN) desirable for KNN thin films.

To study the effects of post-annealing treatments on the crystal structure of thin films, powder diffraction XRD was conducted on the post-annealed samples.

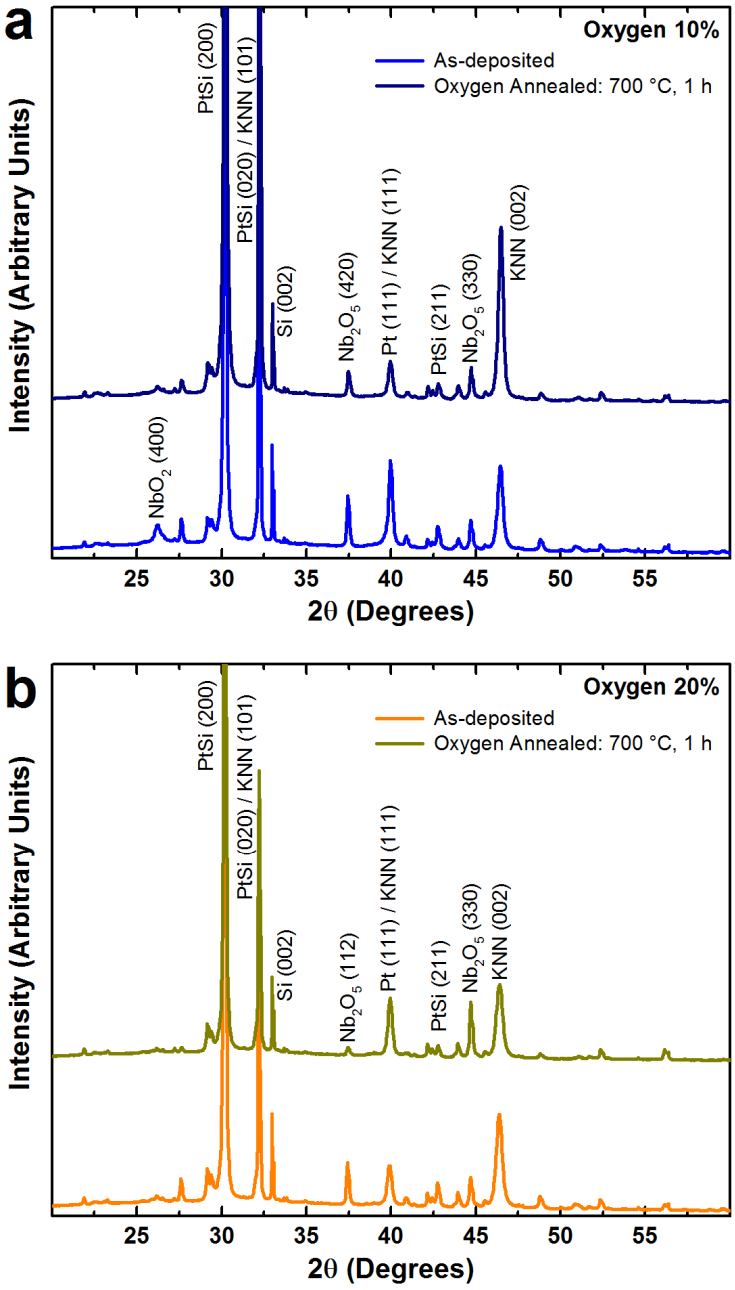

Figure 3.5. X-ray diffractograms for KNN thin films as-deposited at 700 °C and further annealed in oxygen at 700 °C for 1 h. Thin film deposition was carried out at oxygen partial pressures of **(a)** 10% and **(b)** 20%.

Figure 5 presents and compares X-ray diffractograms of as-deposited and post-annealed samples for the films grown under oxygen partial pressures of 10% and 20%. For thin films grown under 10% oxygen partial pressure at 700 °C, post-deposition annealing in an oxygen atmosphere for 1 h at 700 °C results in considerable growth of KNN (002) and KNN (101) orientations, and the suppression of NbO_2 as observed in the XRD results (Fig. 3.5(a)) [3.28,29]. The KNN (111) peak intensity also decreases, indicating the re-orientation of KNN crystal structure in (002) and (101) directions. Films grown under 20% oxygen partial pressure however, exhibit the growth of KNN crystal structure in (111) direction following post-deposition annealing in oxygen atmosphere (Fig. 3.5(b)).

Secondary niobium oxide peaks are reduced in intensity in these samples as well indicating the formation and growth of higher order Nb^{5+} oxidization states, as a result of the annealing treatment, complementary to the results of the XPS analysis (Figure 3.3 and 3.4).

These XRD results, considered in combination with the XPS outcomes, allude to the possibility of engineering the crystalline orientation and alkali ratio in KNN thin films through varying the oxygen partial pressure during the sputtering process coupled with specific post-annealing treatments.

3.1.4. Optimization of the synthesis parameters and post-annealing conditions for KNN thin films

Previous studies on the RF magnetron sputtering of KNN thin films have shown that the composition and the growth rate of KNN thin films are not influenced by growth temperature [3.17,18,24]. Further, the crystalline orientation of KNN thin

films was proven to be dependent on the growth temperature. To substantiate this hypothesis and to test the primary premise that the RF plasma can determine alkali ratios (and thereby, film composition), depositions were carried out on a modified substrate and at a lower temperature. KNN thin films were deposited on Pt/Ti/SiO_2/Si substrates at the growth temperature of 600 °C and post-annealed at 600 °C in oxygen atmosphere for 1 h. Figure 3.6 shows the X-ray diffractograms for as-deposited and post-annealed thin films grown under 20% oxygen partial pressure at 600 °C.

The SiO_2 barrier layer utilized on silicon substrates prior to deposition of platinum thin film prevents the formation of the PtSi layer during deposition at high substrate temperature [3.43]. As a result, the as-deposited nano-crystalline platinum crystallizes into the thermodynamically stable (111) configuration on exposure to higher temperatures. The resulting KNN thin films show strong *c*-axis (001) orientation with the absence of the KNN (101) peak. Strong preferential orientation of platinum layer as opposed to the polycrystalline Pt–Si layer also prevents the formation of crystalline phases for secondary niobium oxide species. The composition of KNN thin films deposited at 600 °C was examined after post-annealing treatment in oxygen *via* XPS, revealing its K/(K+Na) ratio to be 44.2%, almost identical to the film grown under 20% oxygen partial pressure at 700 °C and post-annealed in oxygen for 1 h. The (K+Na)/Nb ratio was 43.9%, slightly lower than the ratio at 700 °C. These XPS results highlight that the changes in the deposition temperature and the substrate do not significantly influence the RF plasma diffusivity which determines alkali loss and alkali-niobium ratio.

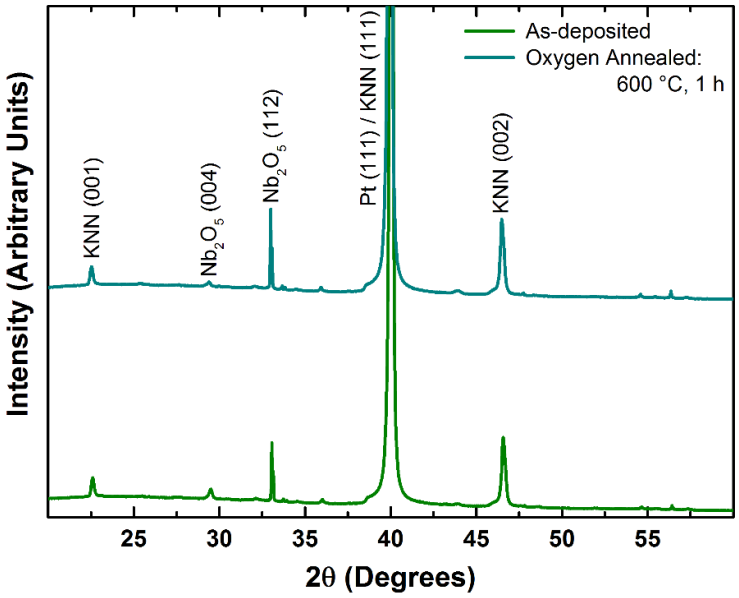

Figure 3.6. X-ray diffractograms for KNN thin films as-deposited at 600 °C and annealed in oxygen at 600 °C for 1 h.

In summary, the ability to control alkali concentration and ratio in lead-free KNN thin films has been examined. It has been shown that the lighter alkali species (sodium) experiences greater scattering in the deposition atmosphere; while both alkali species are significantly scattered in comparison to niobium. These results highlight the need to account for such loss in species during the RF sputtering process by tailoring the initial sputtering target composition. Such alkali ratio control by varying oxygen partial pressure, independent of substrate temperature and configuration, also provides a mechanism to vary dopant concentrations in thin film samples using just one sputtering target of fixed composition. Further, the stabilization of the KNN phase has been achieved through the elimination of secondary phases using a facile high-temperature post annealing process in oxygen atmosphere. Moreover, the effect of substrate orientation and crystallinity on the crystal structure of high temperature RF-sputtered KNN thin films was highlighted. Results for thin films sputtered at

600 ℃ on platinized silicon substrates with thermally grown SiO_2 barriers signal the formation of a strongly (111) textured platinum layer which in turn leads to a strong orientation in the KNN thin films. This further highlights the significance of temperature control during the RF deposition which allows for the effective control of the orientation in metallic substrate layer and in turn the preferential orientation in KNN perovskite oxide thin films.

3.2. Compositional and Oxygen Deficiency Control in $SrTiO_3$ Perovskite Oxide Thin Films for RRAM Applications

Strontium titanate ($SrTiO_3$: STO), the archetypical perovskite oxide with a vast majority of functional properties and an incredible flexibility for functionalization through compositional and structural engineering [3.44-48], has shown great potential for nanoscale resistive switching applications [3.49-55]. This is due to the inherent tendency of the stable perovskite structure of STO to harbor oxygen vacancy point defects and the pronounced redox activity along dislocations in TiO_2 sub-lattice [3.49,56]. Oxygen vacancy induced defect structures induced by electroforming play a decisive role in determining the resistive switching performance of metal-oxide-based devices. Therefore, synthesizing the oxide layer with a controlled concentration of oxygen vacancies can enhance the switching performance *via* the introduction of a network of point defects. Moreover, a built-in oxygen vacancy network provides greater flexibility and control over the electroforming process and partially eases high energy requirements for the creation of defect-rich, conductive filamentary pathways.

In this section, a facile low temperature synthesis route based on controlled RF-magnetron sputtering is introduced, to attain amorphous $SrTiO_3$ (*a*-STO) thin films with precise control over thickness, oxygen deficiency and external dopant concentration. The results of this investigation have been partly published in the journal of ***Advanced Functional Materials*** [3.57].

3.2.1. Controlled RF-magnetron sputtering of amorphous $SrTiO_3$ (*a*-STO) thin films

STO thin films were deposited by room temperature RF-magnetron sputtering on $Pt/TiO_2/SiO_2/Si$ (50:10:300 nm) substrates. A 100 mm diameter ceramic STO target stoichiometric composition was used for all depositions. Further, a metallic niobium (Nb) target was used at the DC source for co-sputtering of Nb species during the RF sputtering of STO thin films.

Table 3.4. Sputtering and co-sputtering parameters for STO thin films

Substrate	$Pt/TiO_2/SiO_2/Si$ (50:10:300 nm)
Target	$SrTiO_3$
Process Gas	0, 5% oxygen in argon
Base pressure	1×10^{-7} Torr
Sputtering Pressure	5×10^{-3} Torr
Substrate Temperature	Room Temperature
RF Power	100-200 W
DC Power	0-40W

Oxygen partial pressure as well as the sputtering power on both RF (STO) and DC (Nb) sources were systematically varied and the sputtered thin films were analyzed for their thickness, composition and crystal structure to obtain the optimum synthesis parameters for STO thin films. Table 3.4 summarizes the sputtering conditions.

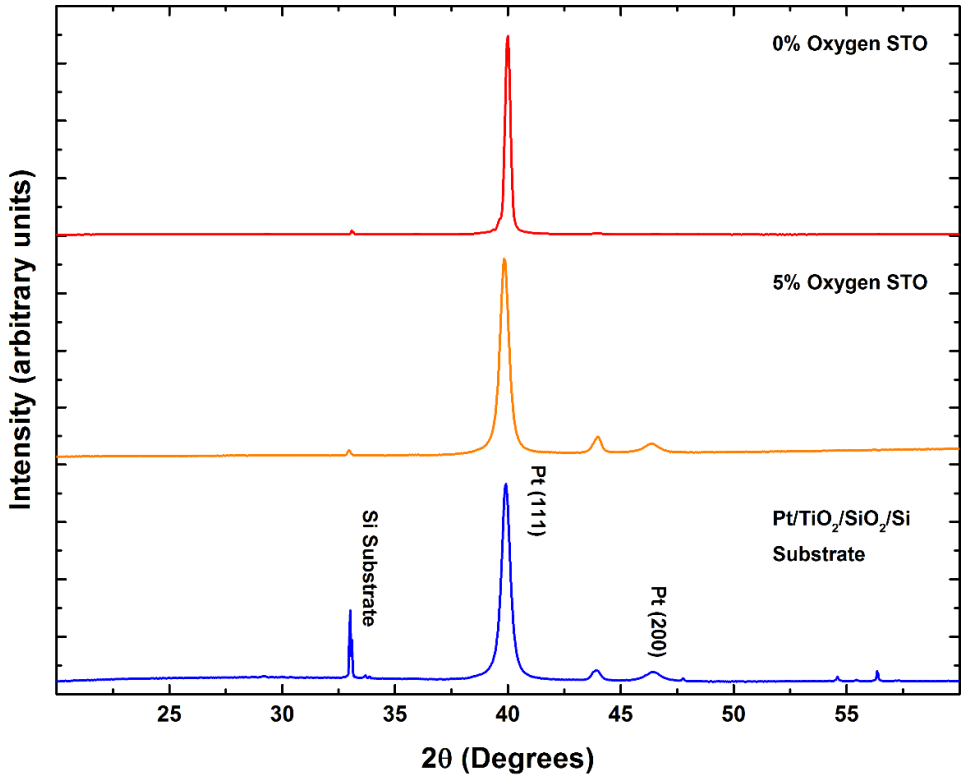

Figure 3.7. X-ray diffractograms for $Pt/TiO_2/SiO_2/Si$ substrate and STO thin films deposited in 0% and 5% oxygen partial pressure at room temperature.

RF sputtering power and sputtering time were varied between 100 to 200 W and 1 to 3 hours, respectively to obtain the optimal growth rate for STO thin films. The optimal growth conditions for precise thickness control were achieved at an RF power of 200 W, where the growth rates where 1.12 nm/min and 0.55 nm/min for 0% and 5% oxygen partial pressures, respectively. Figure 3.7 illustrates the XRD diffractograms for 100 nm STO thin films sputtered at room temperature, under 0 and 5% oxygen partial pressures.

No XRD peak pertaining to one of the preferential perovskite orientations was observed in STO thin films. Therefore, it is concluded that similar to previous reports [3.57-60], RF sputtering of STO at room temperature results in the formation of amorphous $SrTiO_3$ (*a*-STO) thin films.

X-ray photoelectron spectroscopy (XPS) elemental and depth profile analysis was carried out through the thickness of the as-deposited thin films to establish the optimum sputtering parameters for tuning the composition of *a*-STO oxide layers. The composition of the thin films was found to be uniform through the thickness with the exception of the surface layer as it is subject to oxidization and ambient contamination (Figure 3.8 and 3.9). Oxygen partial pressure of 5% during the sputtering process results in stoichiometric oxygen *a*-STO thin films with a Sr/Ti ratio of 80%. On the other hand, *a*-STO films sputtered in pure argon atmosphere are slightly Sr-rich and have a uniform oxygen deficiency of ~3% throughout the thickness. Co-sputtering of niobium was carried out during the deposition of oxygen deficient *a*-STO to obtain niobium-doped oxygen deficient *a*-STO thin films (Figure 3.10). For the optimal sputtering conditions, the growth rate of Nb:*a*-STO thin films was found to be ~1.20 nm/min.

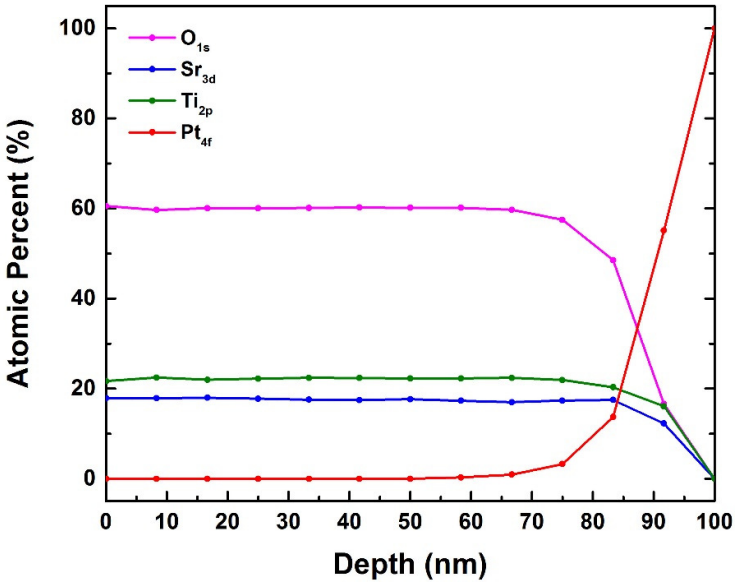

Figure 3.8. Atomic concentrations of the principal elements in as-grown *a*-STO thin films deposited under 5% oxygen partial pressure.

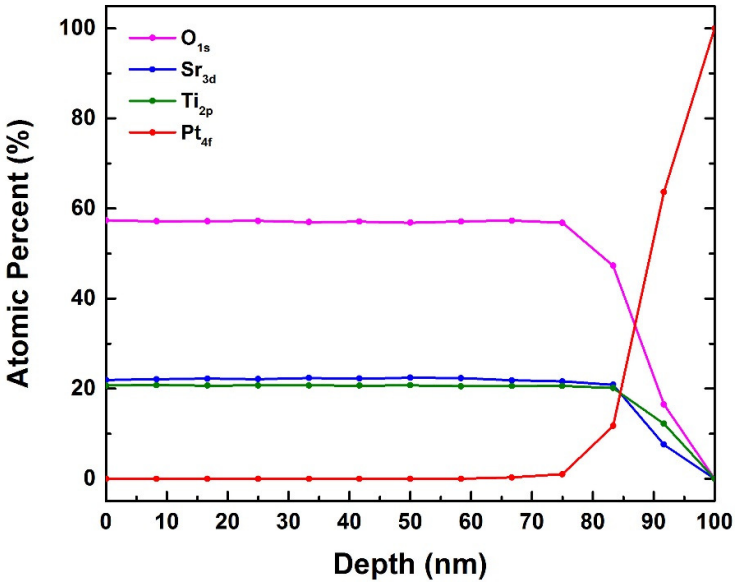

Figure 3.9. Atomic concentrations of the principal elements in as-grown *a*-STO thin films deposited under 0% oxygen partial pressure.

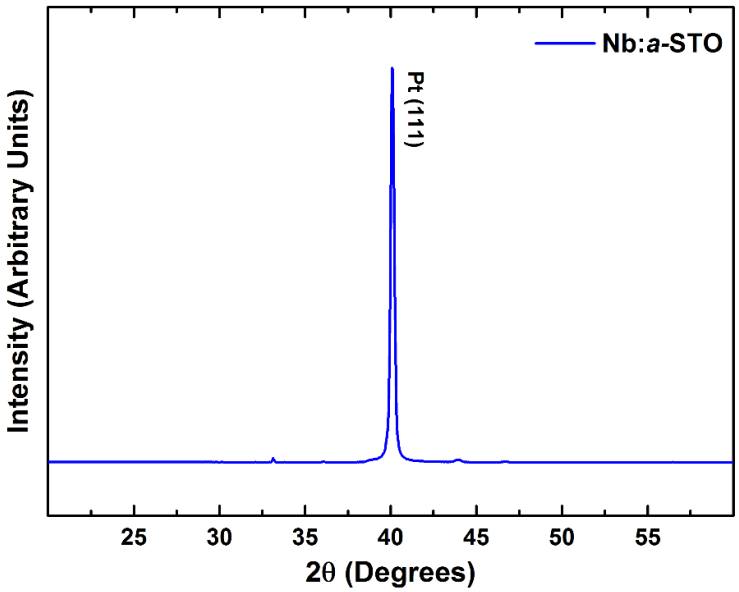

Figure 3.10. X-ray diffractograms of Nb:*a*-STO (DC/RF power: 5/200 W) thin films deposited in 0% oxygen partial pressure at room temperature, confirming their amorphous nature.

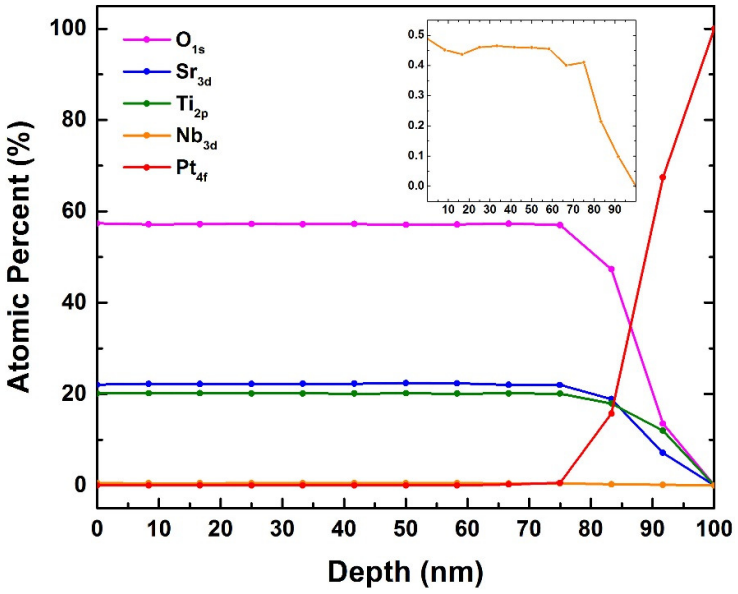

Figure 3.11. Atomic concentrations of the principal elements in as-grown Nb doped *a*-STO thin films deposited under 0% oxygen partial pressure at room temperature (DC/RF power: 5/200 W).

Table 3.5. Sputtering parameters and elemental ratios of sputtered a-STO thin films

	Stoichiometric oxygen *a*-STO	Oxygen-Deficient *a*-STO	Nb-doped Oxygen-Deficient *a*-STO
Sputtering Parameters			
Process Gas	$Ar:O_2$ (95:5)	Ar	Ar
Sputtering Pressure (Torr)	5×10^{-3}	5×10^{-3}	5×10^{-3}
RF Source Power (W)	200	200	200
DC Source Power (W)	N/A	N/A	5
Growth Rate (nm/min)	0.55	1.12	1.20
Principal Elements Concentration (at%)			
Sr	17.8	22.1	22.2
Ti	22.3	20.7	20.1
O	59.9	57.2	57.2
Nb	N/A	N/A	0.46

The low growth rate of the *a*-STO thin films combined with a direct non-linear dependence on oxygen partial pressure and plasma power density, allows for the synthesis of monolithic oxide layers (R_a = 0.45-0.55 nm as characterized by

tapping mode AFM and *in situ* SPM) with thicknesses down to 10 nm. Table 3.5 denotes the sputtering parameters and the composition of *a*-STO thin films.

In summary, the demonstrated low temperature deposition technique for oxygen deficient and doped *a*-STO thin films, provides a facile, CMOS-compatible synthesis route for the realization of functional oxide layers with as-synthesized oxygen deficiencies.

CHAPTER 4

TWO-TERMINAL AMORPHOUS $SrTiO_3$ (*a*-STO) BASED METAL-OXIDE-METAL (MIM) MEMRISTORS

4.1. Two-Terminal Metal-Oxide-Metal Based Memristors

Memory technologies were traditionally utilized to store digital data in the form of “1”s and “0”s. Current interest lies in technologies which enable analog memories that have multiple states. This enables unprecedented high density memories and most significantly neuromorphic computing [4.1,2]. These rely on the electronic state of memories being highly non-volatile, with durable and cyclic switching, and easy differentiation of ON/OFF states. Nanoscale resistive memories (or ‘memristors’) satisfy many of these requirements, and are reliant on functional oxides. They are normally configured as passive two terminal metal-insulator-metal (MIM) devices based on functional binary and ternary metal-oxides (e.g. TiO_2, $SrTiO_3$). These offer a scalable, fast, non-volatile and low energy “memristive” performance [4.3-8]. Their dynamic non-linear current–voltage characteristics also suggest applications in non-linear circuit design and alternative logic architectures.

The bipolar resistive switching behaviour in these devices is attributed to a combination of electronic effects at the metal/oxide interfaces and reversible redox reactions and nanoionics transport in transition metal-oxide layers [4.3,4,7,8]. These processes are triggered in the oxide upon the creation of extended defect structures during an electroforming process, under high electrical gradients. Complex transition metal oxides with perovskite crystal structure are among the most technologically relevant classes of electronic materials. A plethora of functional properties such as ferro/piezoelectricity, ferromagnetism, superconductivity and memristivity can be engineered through the compositional and structural modification of the perovskite structure [4.9-12].

In this chapter CMOS-compatible resistive switching devices based on amorphous STO (*a*-STO) thin films synthesized at room temperature are demonstrated. Compositional analysis of the virgin (as-grown) and electroformed devices underpin the nanoionics-based processes responsible for the conduction mechanisms in *a*-STO switches. Further, the role of defect chemistry, as-gown oxygen deficiency and external dopants in the switching performance of *a*-STO switches is investigated. The results of these investigations have been partly published in the journal of ***Advanced Functional Materials*** [4.13].

4.1.1. MIM memristors based on oxygen deficient *a*-STO oxide layers

To investigate the process of electroforming and subsequent electroresistive switching in oxygen deficient *a*-STO oxide layers, micrometre scale (20-100 µm

electrode dimensions) asymmetric MIM switching cells using a 100 nm oxide layer were fabricated in Pt/Ti/a-STO/Pt configuration. Microscale *a*-STO crossbar arrays were fabricated on SiO_2/Si substrates using a three-step photolithography/lift-off process. In the first lift-off step, 50 nm bottom platinum electrodes with 10 nm TiO_2 adhesion layers were deposited on pre-patterned SiO_2/Si substrates by electron beam evaporation at room temperature. Oxygen deficient *a*-STO thin films of 100 nm thickness were then RF sputtered through a shadow mask. Lastly, Pt/Ti (50:10 nm) top electrodes were patterned using photolithography and deposited by electron beam evaporation at room temperature to complete the crossbar structure (Figure 4.1).

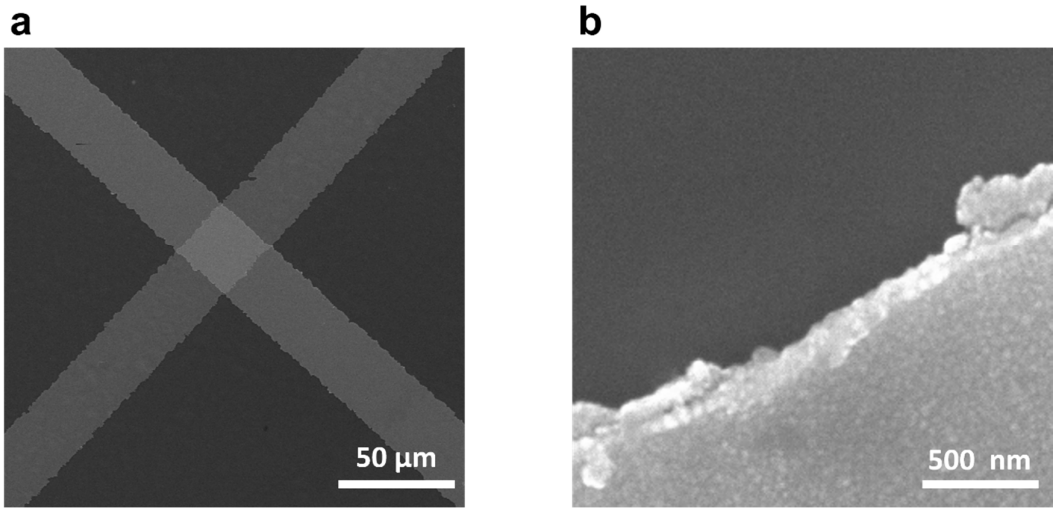

Figure 4.1. (a) Large-view SEM micrograph of a 20 µm × 20 µm Pt/Ti/*a*-STO/Pt crossbar device. **(b)** SEM micrograph of the surface of Pt top electrode and *a*-STO oxide demonstrating the dense, smooth surface of the oxide

As discussed in Chapter 3, X-ray photoelectron spectroscopy (XPS) depth profile results on as grown *a*-STO thin films reveal a uniform oxygen deficiency distribution throughout the thickness of the films. As such, the controlled physical vapour deposition process eliminates the need for the high

temperature reducing steps commonly required for the creation of oxygen vacancies in STO [4.4,14-16].

As previously reported, the dissimilar metal oxide interfaces facilitate robust redox process and the subsequent creation of nano filamentary extended defect structures. Particularly, *a*-STO forms an Ohmic interface with a shallow work function (4.3 eV) Ti which acts as the cathode (transparent to the ionic current) for redox reactions in the oxide layer. Even prior to the creation of the extended defect structures, the Ti is partially oxidized at the vicinity of the interface with *a*-STO according to the reaction $Ti + SrTiO_3 \rightarrow TiO_x + SrTiO_{3-x}$.The top Pt layer prevents further oxidization of the Ti layer which can occur due to exposure to ambient oxygen.

The electrical characteristics of *a*-STO metal-insulator-metal MIM cells were probed using either the bottom or top electrode as the drive electrode with the opposite electrode connected to the system ground. The initial current–voltage (*I*–*V*) curves of MIM devices in virgin state exhibited an area dependent, Schottky-like rectifying characteristic correlated with the choice of bias electrode and voltage polarity (Figure 4.2a). The *I*–*V* characteristics confirm the expected formation of dissimilar Schottky barriers at the Ti/*a*-STO and *a*-STO/Pt interfaces. A single irreversible electroforming (or forming) step, in form of a voltage sweep with maximum voltages in the range of |8-10| V, was required to trigger the electroresistive switching behaviour in *a*-STO MIM devices (Figure 4.2b).

The switching polarity of formed devices is governed by the relative voltage bias polarity between top and bottom electrodes during the electroforming step.

a-STO MIM cells biased from the top electrode were electroformed through a single current limited voltage sweep with a negative polarity and typically higher (~20%) maximum voltages during the electroforming step (Figure 4.3a). Upon electroforming, *a*-STO MIM cells biased from the top electrode show a bipolar switching behavior with a reversed polarity compared to the cells biased from the bottom electrode (Figure 4.3b). The average OFF/ON switching ratios for these devices is found to be around 70. Although top and bottom electrode biased devices were successfully electroformed with both bias polarities, devices formed with an effective positive polarity at the bottom *a*-STO/Pt interface (either through applying a positive bias to the bottom electrode or a negative bias to the top electrode) exhibited greater yield with superior and stable switching performance, and therefore, are the focus of this study.

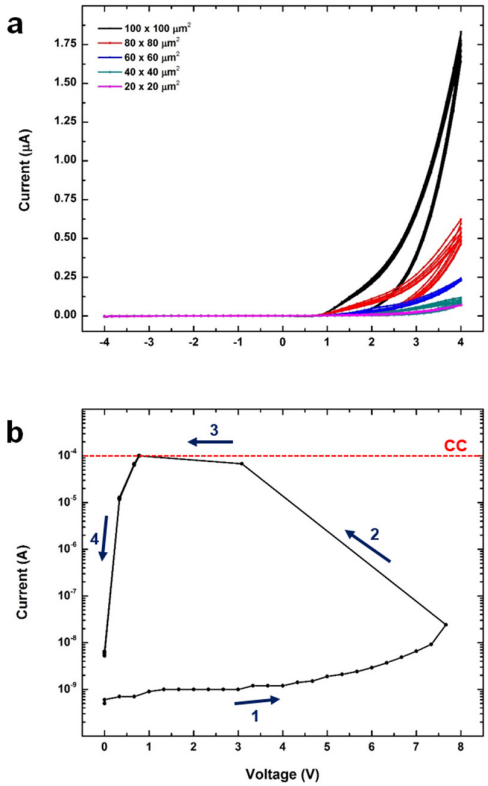

Figure 4.2. Electrical characterization of *a*-STO MIM cells. **(a)** *I–V* characteristics of virgin *a*-STO MIM cells biased from the bottom platinum electrode. **(b)** Typical electroforming sweep in positive polarity for *a*-STO MIM cells biased from the bottom electrode.

Post-electroforming, these devices exhibit stable non-volatile bipolar switching characteristics (Figure 4.4b, c) with OFF/ON ratios that exceed 10^3 over a wide range of READ voltages highlighting their operational flexibility (Figure 4.4c).

Individual devices were successfully operated for more than 10^6 *I–V* sweep WRITE/ERASE cycles with less than 10% deviation in the switching voltages (Figure 4.4c). No appreciable change in the high resistance state (HRS) and low resistance state (LRS) properties was observed at a read voltage of ±250 mV in either polarity over repeated reading cycles of 10^5 seconds (<1% over the total READ period).

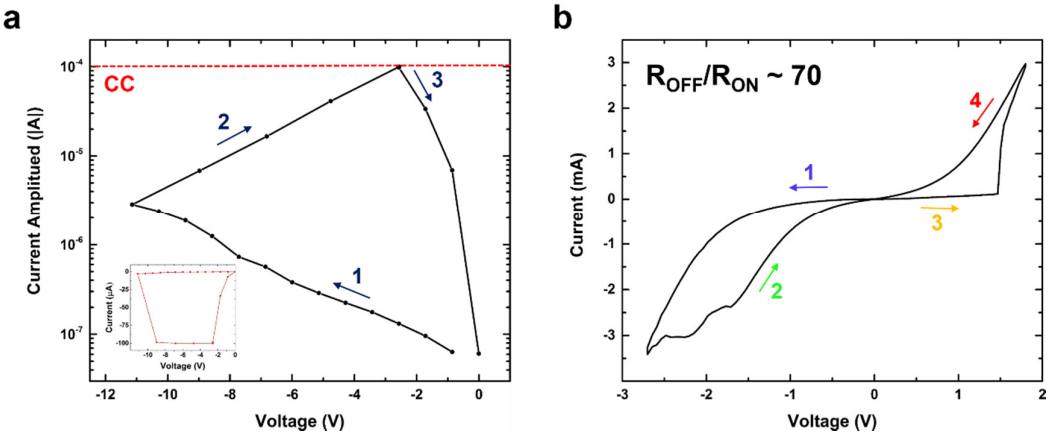

Figure 4.3. Electrical characterization of *a*-STO MIM cells biased from the top electrode. **(a)** Typical electroforming sweep in negative polarity for *a*-STO MIM cells biased from the top electrode. **(b)** Typical bipolar switching behavior of electroformed *a*-STO MIM cells biased from the top electrode.

Pulsed WRITE/READ/ERASE cycles were carried out using pulse widths of 10-100 µs. Table 4.1 outlines the switching performance of *a*-STO cells from

over a hundred tested devices. Both READ and WRITE operations can be carried out at very low current density (considering the cell sizes) in micro-meter scale *a*-STO devices.

The bipolar switching behavior of transition metal oxide layers in MIM configuration is generally perceived to be originating from inhomogeneous conduction mechanisms through localized filamentary channels [4.1,17-19]. As such, the current transport in HRS and LRS regimes is expected to be independent of the geometric area of the MIM device. Figure 4.4d presents the resistance-area product *vs*. the device area for micron-sized *a*-STO MIM cells of

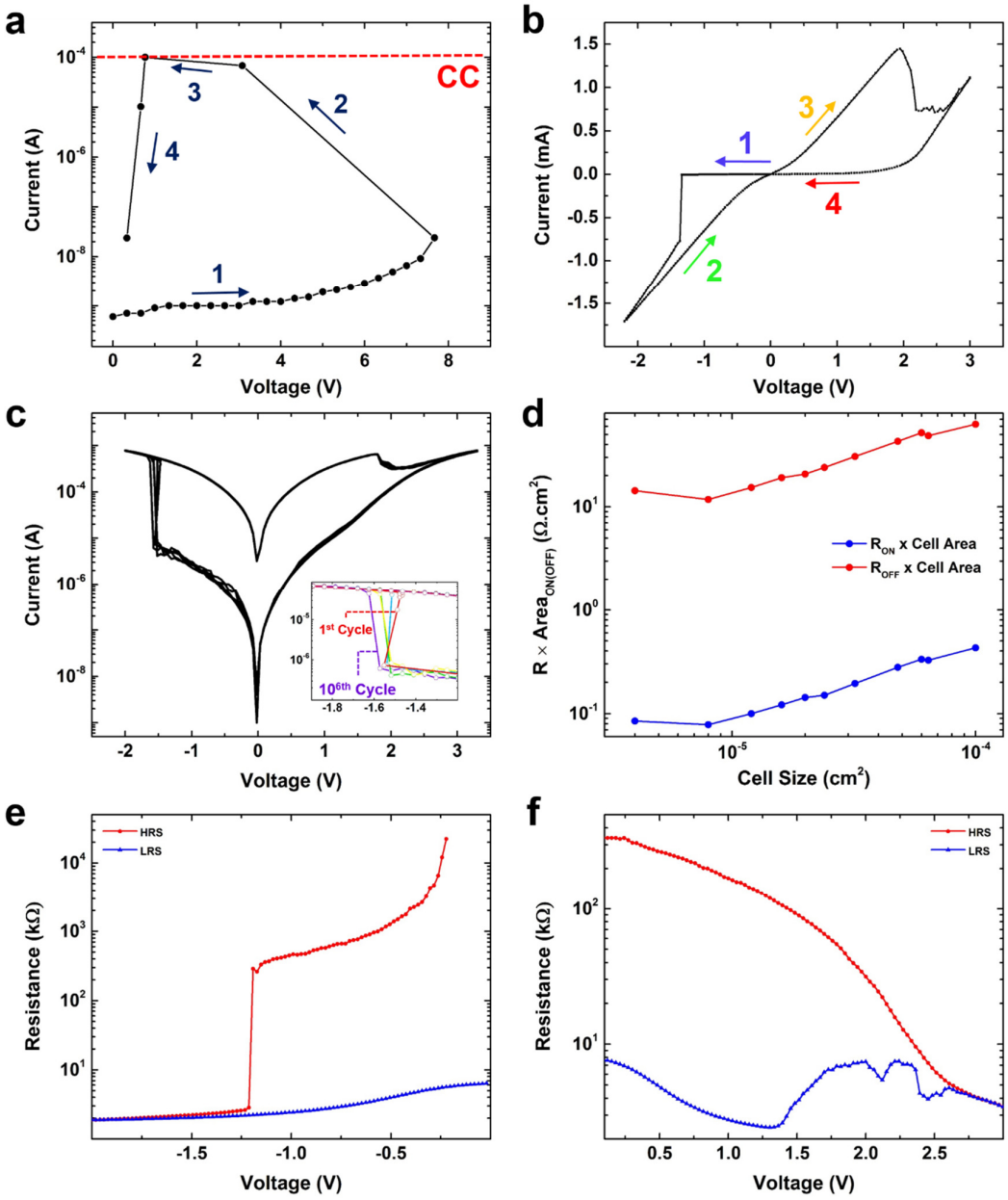

Figure 4.4. Resistive switching performance of electroformed *a*-STO MIM cells. **(a)** Typical electroforming sweep in positive polarity for *a*-STO MIM cells biased from the bottom electrode. **(b)** Typical bipolar switching behaviour of *a*-STO MIM cells. **(c)** Bipolar switching performance of a single cell over 10^6 consecutive *I*–*V* sweep. **(d)** Resistance-area products for *a*-STO MIM cells of various sizes in OFF and ON states. The resistance values were extracted through a linear fit to the *I*–*V* curves in the range of designated READ voltages of ±250 mV. **(e)** High and **(f)** low resistance states (HRS and LRS, respectively) of *a*-STO cells as function of READ voltage.

various sizes. The increase in the R×A product with increasing the device size clearly indicates a local conduction mechanism in both HRS and LRS regimes. Further, No appreciable size-dependency was observed for either the ON/OFF ratios or the READ/WRITE current densities in either state.

Table 4.1. Performance characteristics of *a*-STO memory cells

WRITE Voltage / Current (V / μA)	-1.35 / 200
READ Voltage / Current at LRS (mV / μA)	±250 / 85
ERASE Voltage / Current (V / μA)	1.9 / 600
READ Voltage / Current at HRS (mV / μA)	±250 / 0.6
Retention (s)	$>10^5$
Number of Cycles	$>10^6$
ON Switch Voltage Drift	8.6±1%
OFF Switch Voltage Drift	4.5±1%

The size-independency calls for a detailed investigation into the nature of resistive switching mechanisms in *a*-STO devices which will be addressed in the following sections, as this is an invaluable trait for scaling devices down to the nanoscale. The switching performance of *a*-STO devices is comparable to the best reported STO and TiO_2 based devices [4.17,19]. Such switching performance has not been previously demonstrated in STO-based devices on CMOS-compatible substrates (most reported devices have been fabricated on single crystal STO substrates [4.4,20-22]) or with a low temperature CMOS-compatible process. The facile fabrication of high performance resistive switching devices based on a single *a*-STO oxide layer can open new horizons in design and fabrication of resistive memory devices complementary to planar, semiconductor technology in the form of biocompatible and flexible devices [4.23].

4.1.2. The electroforming mechanism in *a*-STO MIM memristive cells

The electroforming process facilitates the electroresistive switching in intrinsically insulating metal oxides by permanently altering their stoichiometry and oxygen vacancy distribution *via* redox processes [4.7,8,14]. In order to characterize the impact of electroforming on the defect chemistry of *a*-STO thin films, XPS depth profile was performed on 100 µm × 100 µm junctions before and after electroforming The devices size was chosen to comply with the lowest X-ray spot-size (100 µm) available in the XPS system (Figure 4.5).

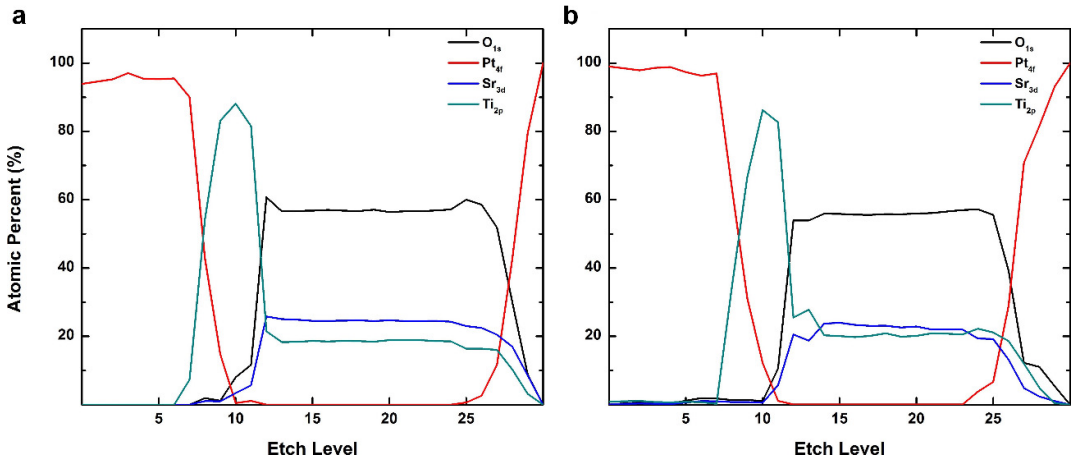

Figure 4.5. Atomic concentrations of the principal elements in *a*-STO devices. **(a)** Relative elemental ratios in virgin *a*-STO MIM cells. **(b)** Relative elemental ratios in electroformed *a*-STO MIM cells. Values are calculated from XPS depth profile analysis on 100 µm × 100 µm devices. While virgin *a*-STO devices show a uniform oxygen deficiency of around 3% throughout the oxide thickness, there is an enhanced deficiency gradient in formed cells with oxygen deficiency level being highest at the electroforming cathode (Ti/*a*-STO) interface.

Virgin devices exhibit a largely uniform atomic concentration with an oxygen deficiency of ~3% indicating a weak n-type doping (Figure 4.6a). On the other hand, electroformed devices show an overall enhancement in oxygen deficiency

concentration (~5%), in particular a sharp increase at the top interface with the titanium layer (Figure 4.6a). However, due to the averaging nature of the technique, an increase in the oxygen deficiency in the formed relative to the virgin devices implies that a large area of device has undergone redox processes upon electroforming. This is in contrast to common observations of highly localized filamentary pathways (usually around the edges) in MIM resistive switching devices based on redox processes in metal oxides (for example, in TiO_2 and Fe-$SrTiO_3$) [4.19,24-26]. This instigated further investigation into the impact of electroforming on the structure and switching mechanisms of *a*-STO devices using *in-situ* nanoscale probing experiments in Chapter 5.

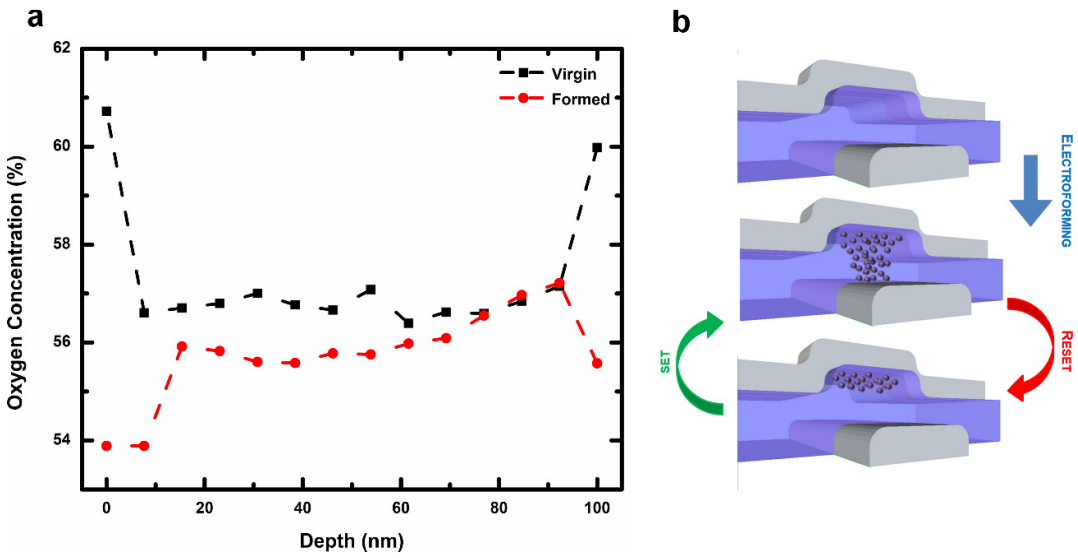

Figure 4.6. Electroforming and switching mechanisms in *a*-STO MIM cells. **(a)** Relative oxygen concentration throughout the thickness of the oxide layer calculated based on XPS depth profile results on 100 µm × 100 µm cells. **(b)** Schematic of electroforming and subsequent switching mechanisms in *a*-STO cells. The electroforming step results in an enhanced oxygen deficiency in the MIM cell. Subsequent motion of oxygen ions along the extended defect structure is responsible for bi-stable, cyclic switching behaviour.

Since the oxygen deficiency distribution is uniform in the virgin oxide layer, the metal/oxide interfaces dominate the conduction mechanisms in virgin devices and therefore largely govern the electroforming process. At a sufficiently high voltage bias, an abrupt jump in current is observed. A current compliance limit of 100 µA ensures that the bias voltage is compensated (*i.e.*, scaled back) to prevent further breakdown of the device. Following this process, the devices exhibit repeatable bipolar switching behaviour between a highly conductive ON and a highly resistive rectifying OFF state. This denotes electrically induced redox processes taking place at the Ti/*a*-STO which create a locally high concentration of oxygen vacancies in the vicinity of metal/oxide interface [4.8]. During the electroforming process with the *a*-STO/Pt interface as the drive (anode) electrode, oxygen vacancies drift away from the forward biased bottom interface through the most favorable paths in the amorphous oxide structure towards the top Ti/*a*-STO interface, resulting in a strongly n-type doped region with a high concentration of oxygen vacancies in the vicinity of the top interface. This in turn lowers the electronic barrier at the top interface, facilitating the redox processes under the high electrical stress. As such, the electrical barrier at top Ti/*a*-STO interface irreversibly collapses, and conductive channels propagate towards the bottom *a*-STO/Pt interface, creating a virtual cathode which is limited by the current compliance limit and the forward bias on the anode [4.8,18].

4.1.3. Ionic migration based switching mechanisms in *a*-STO MIM memristive cells

Figure 4.6b depicts a schematic for the switching behaviour of *a*-STO cells after the electroforming step. The electroformed STO MIM devices are pre-set to ON

state. The switching behaviour of electroformed *a*-STO MIM cells can be described by a simplistic memristor plus rectifier equivalent circuit [4.18]. In the OFF state, the conduction mechanism of the device is governed by the low oxygen vacancy concentration region at the bottom *a*-STO/Pt interface (the current limiting anode) as indicated by the rectifying Schottky-like transport characteristics of the *I–V* curves (Figure 4.2a). On applying a negative bias to the bottom interface, oxygen vacancies drift from the Ohmic virtual cathode region (vacancy enriched Ti/*a*-STO interface) towards the bottom through the pre-formed conduction channels, thinning the depletion layer at the *a*-STO/Pt interface and switching the device to ON state where the electron tunnelling through a thin residual barrier manifests itself as a symmetrical *I–V* characteristic (Figure 4.4), similar toTiO_2 devices (reported by Yang *et al.* [4.18,19]). A reversal of bias polarity at the bottom interface repels the oxygen vacancies in the conduction channel(s) further away from the *a*-STO/Pt interface resulting in the recovery of the electronic barrier and switching the device back to OFF state.

4.2. The Role of Defect Chemistry in the Switching Performance of *a*-STO MIM Devices

4.2.1. Switching performance of *a*-STO MIM cells with different stoichiometry

In order to investigate the effect of oxide layer stoichiometry on the switching performance of *a*-STO MIM cells, identical micrometre scale (20-100 µm dimensions) were fabricated using 100 nm oxide layers with the compositional values discussed in Chapter 3 (i.e. Stoichiometric oxygen, Oxygen-deficient and

Nb-Doped oxygen-deficient *a*-STO). The metal electrodes thickness and structure were kept the same for all MIM cells.

All *a*-STO MIM devices were highly insulating in their virgin state and showed Schottky-like transport characteristics. The bipolar resistive switching is achieved following an electroforming procedure for STO-based MIM devices [4.3,4,8,21,27]. In order to create an oxygen vacancy gradient in STO-based memristive devices, an ohmic contact permissible to ionic current (e.g. a contact with a low work function metal), and a blocking contact (e.g. a high work function metal) should be engineered in MIM devices. [4.8,20,22].

A single electroforming voltage sweep from the bottom Pt/*a*-STO interface was necessary to induce resistive switching behavior in *a*-STO devices. A current compliance limit of 100 µA was set to prevent the complete breakdown of the oxide layer. Figure 4.7c shows the electroforming procedure of devices utilizing *a*-STO thin films with different compositions. *a*-STO thin films with stoichiometric oxygen content are electroformed though voltage sweeps in the range of 11-13 V (Figure 4.7c). Following the electroforming, the *a*-STO devices show bipolar switching characteristics with switching ratios of the order of 50-70 at a READ voltage of ±250 mV (Figure 4.7d). On the other hand, oxygen deficient *a*-STO thin films require peak voltage sweep range of 8-10 V during the electroforming step. The bipolar switching behavior of oxygen-deficient *a*-STO thin films is more stable and the switching ratios are significantly enhanced to 10^3-10^4 (compared to $<10^2$ for the stoichiometric oxygen *a*-STO devices) at similar READ voltages. For niobium-doped oxygen-deficient *a*-STO thin films, maximum required sweep voltages for electroforming drops significantly (5-6 V).

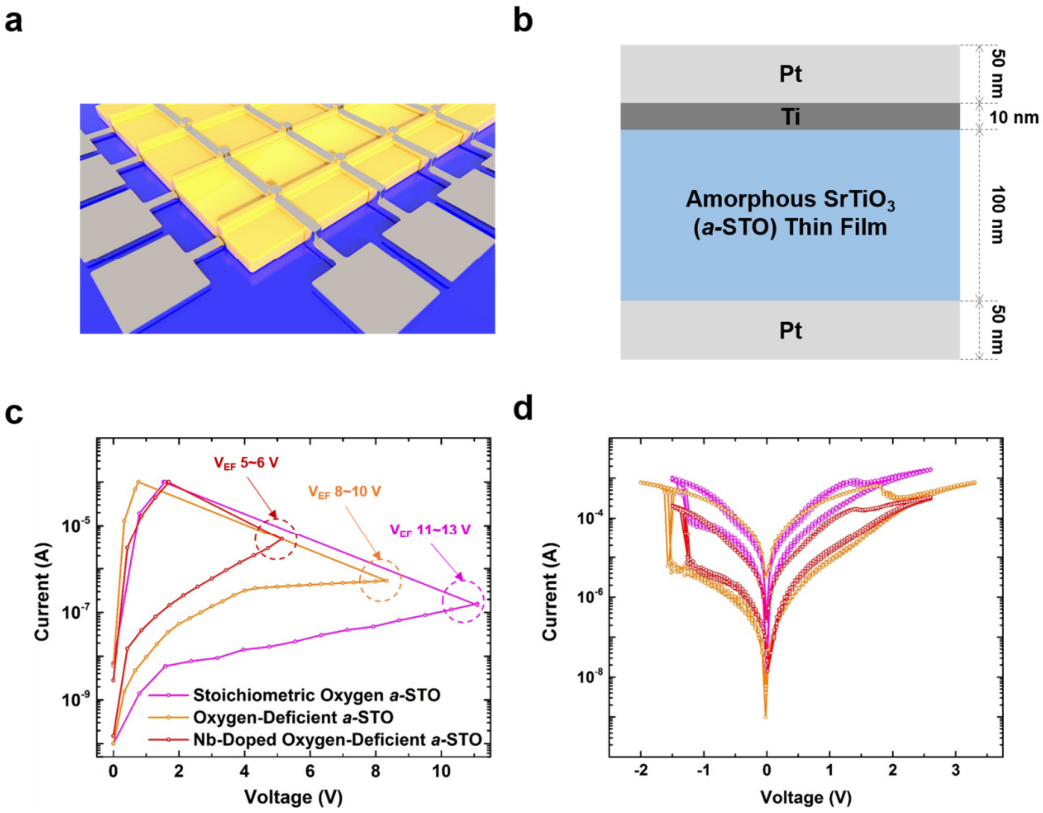

Figure 4.7. (a) Schematic of the cross-bar structure. **(b)** Cross-sectional schematic of *a*-STO MIM cells. **(c)** Typical electroforming sweeps and **(d)** representative bipolar switching behavior over 10^4 cycles for *a*-STO MIM cells utilizing different oxide layers.

Table 4.2. Performance characteristics of *a*-STO MIM devices.

	Stoichiometric Oxygen *a*-STO	Oxygen-Deficient *a*-STO	Nb-Doped Oxygen-Deficient *a*-STO
Electroforming Voltage (V)	11-13	8-10	5-6
Switching Ratios	50-100	10^3-10^4	~10^3
WRITE Voltage / Current (V / µA)	-1.3 / 710	-1.35 / 200	-1.6 / 55
READ Voltage / Current at LRS (mV / µA)	±250 / 160	±250 / 85	±250 / 23
ERASE Voltage / Current (V / µA)	2.0 / 1100	1.9 / 600	1.78 / 446
READ Voltage / Current at HRS (mV / µA)	±250 / 0.3	±250 / 0.046	±250 / 0.021
Retention (s)	>10^5	>10^5	>10^5
Number of Cycles	~10^4	>10^6	>10^6

The electroformed devices retain high switching ratios of ~10^3 that are comparable to those observed for the oxygen-deficient films while showing reduced requirements for WRITE/ERASE and READ currents in both low and high resistance states. More than fifty devices of each oxide composition with electrode sizes ranging from 20×20 to 100×100 μm^2 were tested in sweep WRITE/ERASE and pulsed WRITE/READ/ERASE cycles (pulse widths of 10-100 µs). Table 4.2 details the switching performance of *a*-STO devices.

4.2.2. Role of the defect chemistry in the switching performance of *a*-STO cells

It is well known that the defect structure in transition metal oxides resulting from intermediate chemical phases and oxygen vacancy induced point and line defects, largely determine the memristive behavior of metal oxide based MIM devices [4.2,5,7,8,18,21,27-30]. In order to investigate the chemical states in *a*-STO thin films and the impact of the compositional changes on the memristive behavior of *a*-STO MIM devices, a detailed analysis of the XPS binding energy spectra of principal elements was carried out throughout the thickness of oxide layers. Chemically distinct species were resolved using a non-linear least-square fitting procedure [4.31] after correcting the background of as-obtained XPS spectra using the Shirley algorithm [4.32] and aligning the elemental binding energies to adventitious carbon (C*1s*) binding energy of 285 eV. Figure 4.8 illustrates the de-convolution of the core level spectra of for O*1s* and Sr*3d* in different *a*-STO oxide layers. The chemical phases of Sr and O showed negligible change through the thickness of the oxides indicating a uniform perovskite oxide phase.

Sr*3d* core level spectra through the thickness of all *a*-STO oxides consist of a single component that can be correlated to Sr^{2+} species in amorphous STO structure [4.33,34].

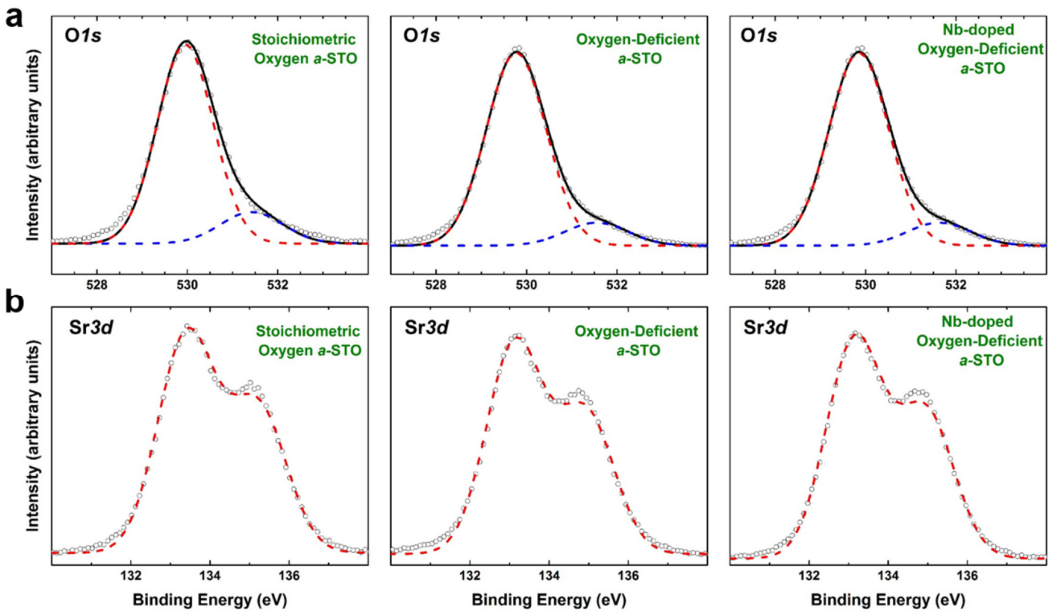

Figure 4.8. De-convolution of binding energy spectra for **(a)** oxygen and **(b)** strontium in virgin *a*-STO oxide layers. O*1s* spectra can be de-convoluted to two into two components with binding energies at 529.9 (O^{2-} ions in *a*-STO structure) and 531.5 eV (adventitious C–O bonds adsorbed onto the sample) for all three oxides. Sr*3d* spectra consists of a single component that can be correlated to Sr^{2+} species in amorphous STO structure. The binding energies for Sr$3d_{5/2}$ spin orbital pairs are 133.4, 133.1, and 133.2 `eV for stoichiometric oxygen, oxygen-deficient, and Nb-doped oxygen-deficient *a*-STO oxides, respectively.

The binding energies for Sr$3d_{5/2}$ spin orbital pairs are 133.4, 133.1, and 133.2 `eV for stoichiometric oxygen, oxygen-deficient, and Nb-doped oxygen-deficient *a*-STO oxides, respectively. The shift to lower binding energies in oxygen-deficient oxides can be interpreted as a shift in the Fermi energy level due to the as-grown oxygen vacancy sites in the *a*-STO structure [4.33]. Moreover, O*1s* spectra in all oxides can be de-convoluted into two components

with binding energies at 529.9 and 531.5 eV, corresponding to O^{2-} ions in the *a*-STO structure [4.35] and the adventitious C–O bonds adsorbed onto the sample surface, respectively.

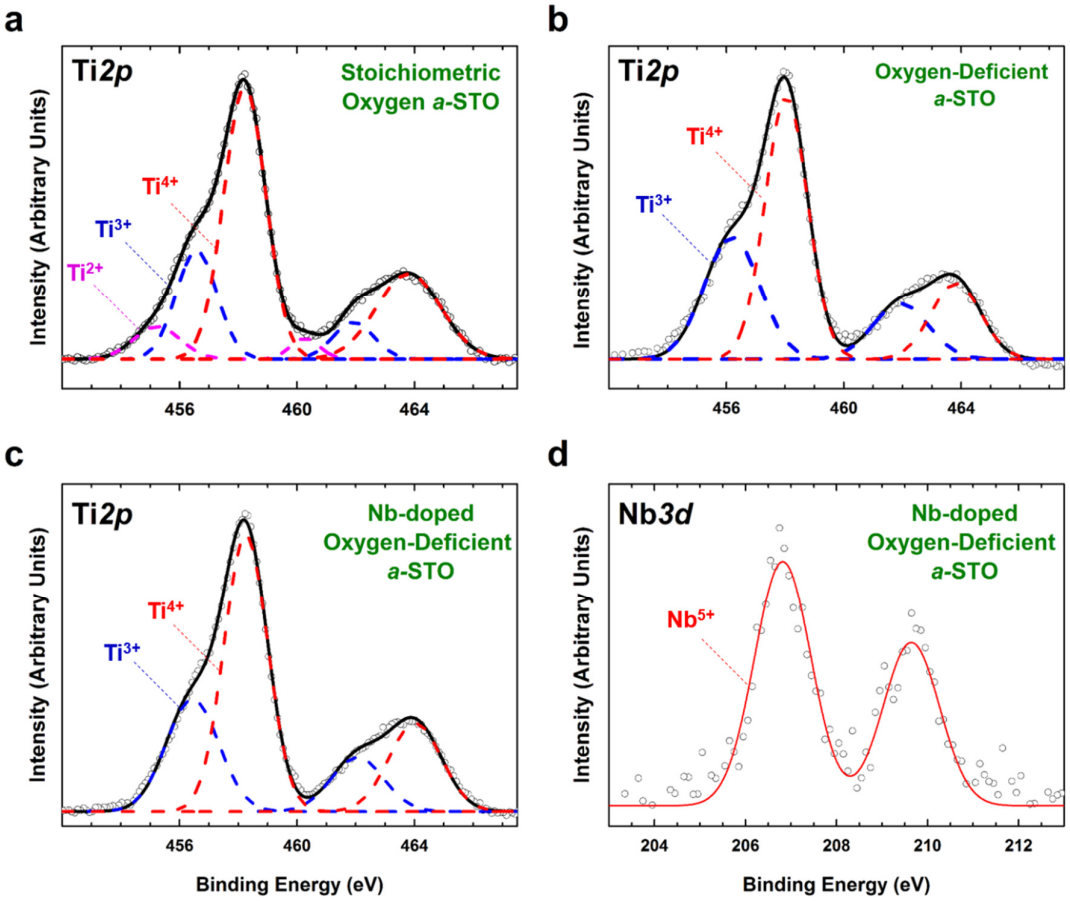

Figure 4.9. De-convolution of binding energy spectra for *B*-site components in virgin *a*-STO oxides. Ti*2p* spectrum of **(a)** stoichiometric oxygen *a*-STO, **(b)** oxygen-deficient *a*-STO and **(c)** Nb-doped oxygen-deficient *a*-STO oxides. **(d)** Nb*3d* spectrum of Nb-doped oxygen-deficient *a*-STO oxide.

The analysis of the core level binding energy spectra of *B*-site components in *a*-STO oxides, provides invaluable insights into the conduction and switching mechanisms of *a*-STO MIM cells. At the top Ti/*a*-STO interface in virgin *a*-STO MIM cells, the Ti*2p* spectra of all *a*-STO devices consist only of Ti^{4+} ($Ti2p_{3/2}$ peak at 458.5 eV) [4.35-37] species indicating a TiO_2 surface finish in *a*-STO

oxides. Except for the top interface, Ti*2p* spectra of *a*-STO oxides exhibit strong dependence on the synthesis conditions. Figure 4.9 illustrates the de-convoluted binding energy spectra for *B*-site components of *a*-STO oxides. These spectra did not show any appreciable change throughout the thickness of oxides. Fractional analysis of Ti*2p* spectrum for stoichiometric *a*-STO virgin MIM cells indicates the presence of Ti^{4+}, Ti^{3+}, and Ti^{2+} oxidation states with reference binding energies of $Ti2p_{3/2}$ peaks [4.35-37] at 458.5, 456.7, and 455.3 eV and relative concentrations of 67.7%, 23.8%, and 8.5% respectively. For pristine and Nb-doped oxygen-deficient *a*-STO cells, Ti*2p* spectra consist only of Ti^{4+} and Ti^{3+} sub-oxides (no Ti^{2+}) with relative concentrations of 60.2%:39.8% and 65.6%:34.4%, respectively.

The bipolar switching behavior of STO-based MIM devices is largely attributed [4.13] to the nanoionics transport mechanisms and reversible redox reactions along the oxygen vacancy induced defect structure in TiO_2 sub-lattice [4.3,4,8,29]. Ti^{3+} species are the signature of charge transfer from oxygen vacancies to neighboring Ti atoms [4.38,39], and therefore, the nanoionics transport processes largely take place along the Ti^{3+} sub-oxide network [4.7,8,40,41]. The relative concentrations of as-grown Ti^{3+} species in oxygen deficient *a*-STO cells is 45-65% higher than that of oxygen-rich cells. *a*-STO oxides sputtered in pure argon atmosphere develop inherent oxygen vacancies due to heavy Ar^+ ion bombardment and preferential removal of oxygen atoms in the vacuum system [4.41,42]. The pre-existing vacancy defect network accounts for their low electroforming energy requirements through reduction of activation energies for the drift diffusion of oxygen vacancies [4.39] and their superior switching characteristics. Moreover, the presence of oxygen during the

sputtering of oxygen-rich *a*-STO oxides facilitates negative ion creation and re-sputtering processes [4.42,43] that lead to the creation of misfit Ti^{2+} metallic sub-oxide species [4.38,44]. These frozen-in misfit species contribute to the formation of *pseudo*-Ohmic conduction pathways during the high energy electroforming process; thereby, reducing the overall resistance and further hindering the switching performance of oxygen-rich *a*-STO MIM cells.

Nb*3d* spectrum in Nb-doped oxygen-deficient *a*-STO devices consists solely of Nb^{5+} ($Nb3d_{5/2}$ peak at 206.86 eV) [4.45,46] species with Nb/Ti ratio of 0.023, throughout the thickness of the oxide. Nb^{5+} species substitutes Ti^{4+} site in *a*-STO structure [4.34,44]. As the ionic radius of Nb^{5+} (0.069 nm) is very close to that of Ti^{4+} (0.068 nm), substitutional doping at such low concentrations is not expected to induce a transition in the electronic structure of the oxide [4.34]. However, the mismatch in the ionization of *B*-site species is likely to introduce additional bands and contribute to an overall reduction of the bandgap. The reduced bandgap results in an overall reduction of the energy requirements during the electroforming procedure while additional electronic energy states render an assistive role to the bipolar switching behavior through non-linear electron trapping/de-trapping and hopping mechanisms reported in published literature [4.2,6,29].

To ascertain the effect of niobium doping on the electronic band energies of oxygen-deficient *a*-STO oxides, photoluminescence (PL) measurements were carried out on virgin MIM cells at room temperature. Under 4.5 eV (275 nm) excitation, two broad emissions were observed for oxygen-deficient *a*-STO, while Nb-doped *a*-STO showed three broad emissions. To obtain further insights into the electronic energy states, these broad spectra were

de-convoluted into individual components. Figure 4.10 shows the de-convoluted PL spectra obtained under 4.5 eV (275 nm) excitation. Pristine oxygen-deficient *a*-STO oxide shows three distinct emission energies (3.3 eV, 3.2 eV, and 2.7 eV). As expected, substitutional niobium doping shifts the two main high bandgap states towards lower energies (to 3.0 eV and 2.9 eV). Further, additional energy states (at 3.9 eV and 3.7 eV) with a difference of ~1.2 eV between the lowest and the highest energy states appear as a result of niobium doping.

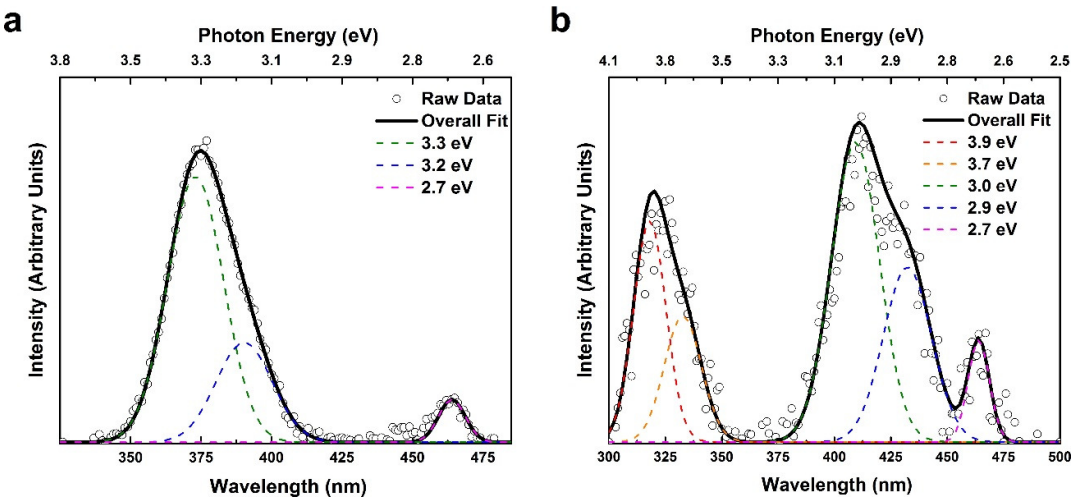

Figure 4.10. Photoluminescence (PL) spectra of **(a)** oxygen-deficient and **(b)** Nb-doped oxygen-deficient *a*-STO oxides under 4.5 eV (275 nm) excitation energies.

Hence, the dynamic evolution of the resistance of the Nb-doped MIM cells can be described by a time evolving state function, which relies on the variability of the carrier hopping through multiple energy states [4.29]. The presence of such energy states creates a non-linear drift of electrons and ions through the conducting channel [4.29]. The relatively lower activation energies needed for carrier hopping reduces the energy requirements for the electroforming process as well as the operating current densities in Nb-doped MIM switching devices.

4.2.3. Defect and oxygen vacancy distribution in *a*-STO switching cells

The evolution of defect structures under high electrical gradients during electroforming is largely believed to be the major contributor to the bipolar electroresistive switching in STO-based MIM devices [4.7,8]. In a typical electroforming step, the defect structure is extended from a *pseudo*-Ohmic electroforming cathode (grounded electrode) towards the blocking anode (positively-biased inert electrode) *via* the migration of positively charged oxygen vacancies along the pre-existing defect structure. This results in the formation of a virtual cathode that can be expanded (during SET) or abridged (during RESET) depending on the polarity of electrical field [4.8]. To investigate the impact of electroforming on the defect structure of *a*-STO MIM cells and ascertain the dynamics of their memristive behavior, XPS analysis was carried out throughout the thickness of active oxygen-deficient *a*-STO memristive cells. The interface between the TiO_2 finished surface of *a*-STO oxide and the Ti layer (which forms an Ohmic contact) is kept as the electroforming and switching cathode (grounded electrode) throughout all experiments. O*1s* spectra averaged over the whole area at the interfacial region of *a*-STO MIM cells (Figure 4.11c) indicate a sharp decrease of oxygen content in the electroformed *a*-STO oxide at the interfacial region. The oxygen concentration increases to almost the same level as in the virgin oxide (~57%), beyond 30 nm from the interface. The large oxygen vacancy gradient in a-STO switching cells indicates the formation of virtual cathode regions at the top Ti/a-STO interface during the electroforming step. Moreover, such large systematic variations in the oxygen concentrations over the whole switching cell area, hint to distributed

multi-filamentary conduction mechanisms similar to those reported in STO single crystals [4.20], rather than highly localized filamentary conductive channels typically observed in STO- and TiO2-based MIM switching cells [4.19,24,26,27,47]. As such, it appears that the electroforming and subsequent bipolar switching takes place across the entire *a*-STO MIM cell area. The evolution of Ti*2p* binding energy spectra in active *a*-STO MIM cells near the interfacial region (Figure 4.11d-f) complement the evidence for multi-filamentary redox-based switching process in *a*-STO memristive cells.

At the top Ti/*a*-STO interface, Ti*2p* spectra of active *a*-STO cells indicate the presence of a third, metallic Ti phase with a reference Ti$2p_{3/2}$ binding energy of 453.3 eV. The peaks for Ti^{3+} and Ti^{4+} species appear at the same binding energies as in the virgin oxide, albeit with the relative Ti^{3+}/Ti^{4+} concentration dropping to 46% (from 65% for the virgin oxide).

The appearance of a strong metallic phase is most likely due to the presence of Ti layer residue at the top interface, possible diffusion of Ti atoms into the *a*-STO structure during the deposition process, and oxygen exchange reactions during the electroforming step. Further from the interface, relative Ti^{3+}/Ti^{4+} concentration is around the same level as the virgin oxide (65%). Moreover, the third Ti$2p_{3/2}$ peaks shift towards higher energy states (453.8 and 454.4 eV at 15 nm and 30 nm away from the interface, respectively) which signals the formation of partially oxidized $Ti^{(2-\delta)+}$ phases during the electroforming step. Beyond 30 nm from the interface, the peak disappears and the configuration of Ti*2p* spectra is similar to that of the virgin devices.

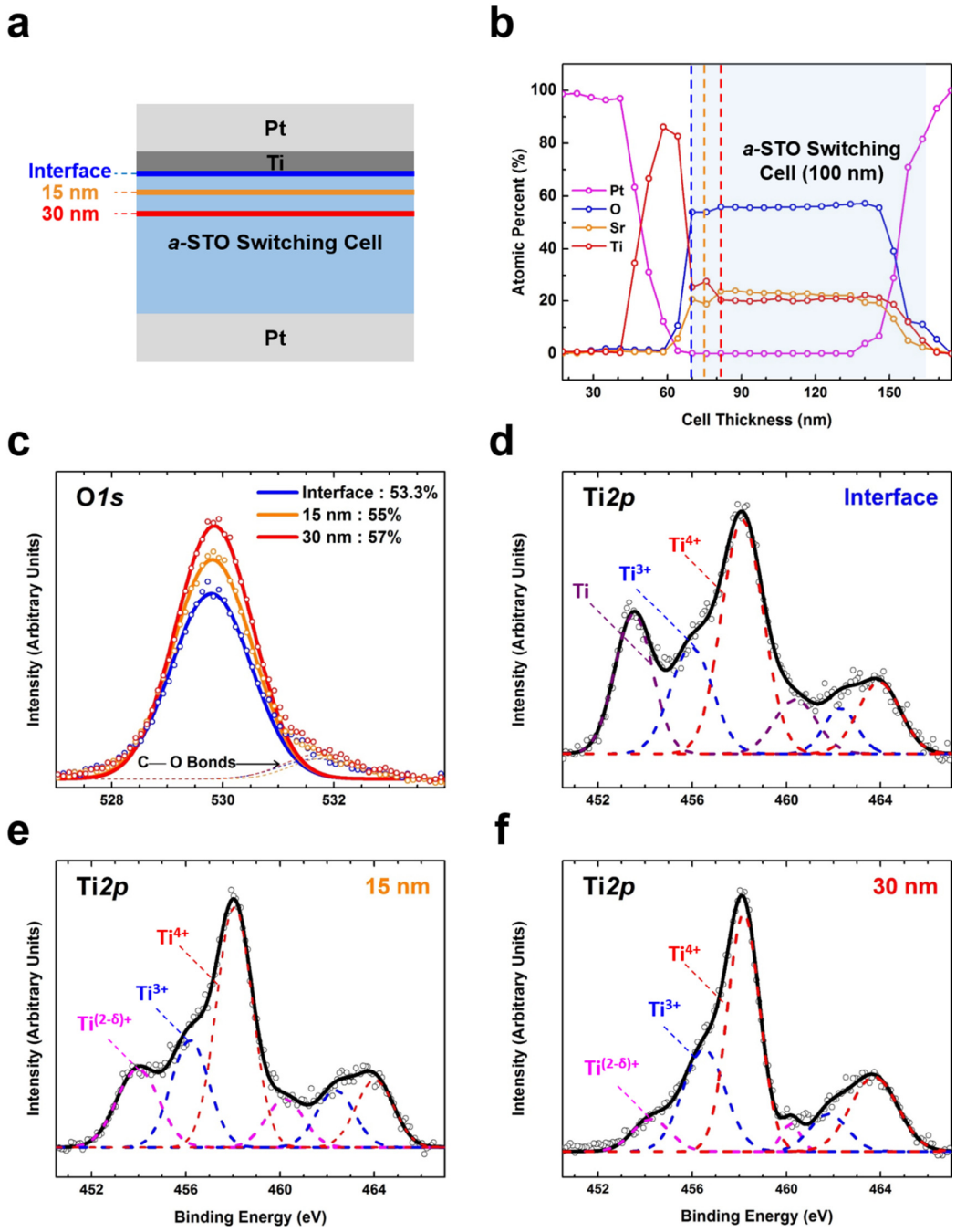

Figure 4.11. De-convolution of binding energy spectra of TiO_2 sub-lattice components throughout the thickness of *a*-STO cells. **(a)** Schematic of an *a*-STO switching cell highlighting the relative depths of the analyzed spectra, **(b)** atomic concentrations of principal elements through the thickness of an active 100 µm² *a*-STO cell **(c)** O*1s* spectra of an active *a*-STO cell at different depths (corresponding to the horizontal lines in the schematic) relative to the top Ti/*a*-STO interface, **(d-f)** Ti*2p* spectrum of the active *a*-STO cell at the same relative depths.

As such, the appearance of a metallic Ti sub-oxide network as a result of the electroforming step points to the creation of oxygen vacancy networks at the vicinity of top Ti/*a*-STO interface and adds more weight to the argument that the resistive switching originates from the migration of oxygen vacancies. The distributed area nature of the XPS signal indicates that the vacancy networks are created across the device near the ohmic interface. However the observed area-independency of the resistive switching hints to a filamentary-type switching at the active (*a*-STO/Pt) interface. Therefore an assumption of the existence of multiple conductive filaments seems viable and will be investigated through conductive nano-contact experiments in Chapter 5.

CHAPTER 5

INVESTIGATION OF NANOSCALE CONDUCTION AND SWITCHING MECHANISMS IN *a*-STO OXIDES

5.1. Probing Nano-Electromechanical Coupling Effect Using *in situ* Electrical Nanoindentation

The phenomena arising from the electromechanical coupling in perovskite oxides at low dimensions can facilitate novel approaches that can overcome current technological bottlenecks [5.1] to realize the next generation of non-volatile memories and logic devices based on nanoionics enabled resistive switching effect [5.2,3]. Nanoscale electromechanical phenomena in functional oxide layers, ranging from flexoelectricity to mechanically-induced insulator-metal transitions (IMTs), have been a subject of rigorous research effort in recent years [5.2,4,5]. In case of STO, strain-induced effects (such as ferroelectricity) have been previously reported and investigated in detail [5.6-9]. Recent theoretical studies have also indicated the role of mechanical stress in enhancing in-plane oxygen vacancy migration [5.10,11]. *In situ* electrical

nanoindentation provides a powerful tool to investigate such phenomena in complex electronic material systems through providing a direct time-based coupling between nano-mechanical and electrical response [5.12-14].

This chapter details the use of quantified *in situ* electrical nanoindentation measurements for investigating nanoscale conduction and switching mechanisms and electromechanical couplings in oxygen deficient *a*-STO oxides as an oxide template for high performance memristive devices. The results presented in this chapter are partly published in the journal of ***Advanced Functional Materials*** and the details of quantified *in situ* electrical measurements are published in the ***Journal of Applied Physics***.

5.2. Quantitative *in situ* Electrical Nanoindentation: Nano-Contact Properties

The ability to quantify the *in situ* electrical response, coupled with the unrivaled mechanical control of the nanoindentation experiments will create an irreplaceable toolbox to investigate electromechanical coupling effects in novel complex electronic material systems. This goal is however hampered by the difficulties of an accurate theoretical and/or *ex situ* assessment of the nanoindenter probe's inherent electrical properties and geometric factors, and the electrical transport properties of nanoscale contacts. The inaccuracies in determining the true electrical nano-contact area during an *in situ* electrical nanoindentation experiments have to be addressed prior to quantifying the nano-electromechanical response.

Accurate characterization of nanoscale electro-mechanical properties through *in situ* electrical nanoindentation experiments [5.12,14] is dependent on a precise evaluation of the true electrical contact area as well as the resistance profile of the conductive indenter subject to indentation load/depth. This allows to underpin distinct phenomena modifying the transport behavior of the material at the nanoscale contact during nanoindentation [5.15-19].

An empirical model has been developed to characterize the evolution of contact resistance subject to contact load/depth which precisely includes the dynamics of the true electrical contact area. The model is developed and verified using *in situ* electrical indentation data on standard bulk gold samples (ρ_{avg} = 2.8 μΩ.cm) and FTO coated glass slides (ρ_{avg} = 290 μΩ.cm) to widen the validity of the predicted values across the range of samples' mechanical properties, surface topography and electrical resistivity. The empirical model relies on the conductive tip's area profile, characterized on standard fused quartz samples. Appendix B details the methodology of the tip area calibration and describes the use of the empirical relations for detailed analysis of nano-electromechanical properties of nano-crystalline platinum thin films.

5.2.1. Nano-contacts in elastic and elasto-plastic regimes

Where penetration depths are sufficiently larger (~5 times) than the surface roughness of the sample, calculations based on the tip area functions provide an accurate estimate of the nominal electrical contact diameters. For the purpose of a preliminary estimation of the nano-contact's resistance profile, the nominal contact diameter (*d*) at a given penetration depth (h) can be explained in terms of a geometric contact [5.20,21]:

$$d = 2 \times \sqrt{2R_e h - h^2} \qquad (1)$$

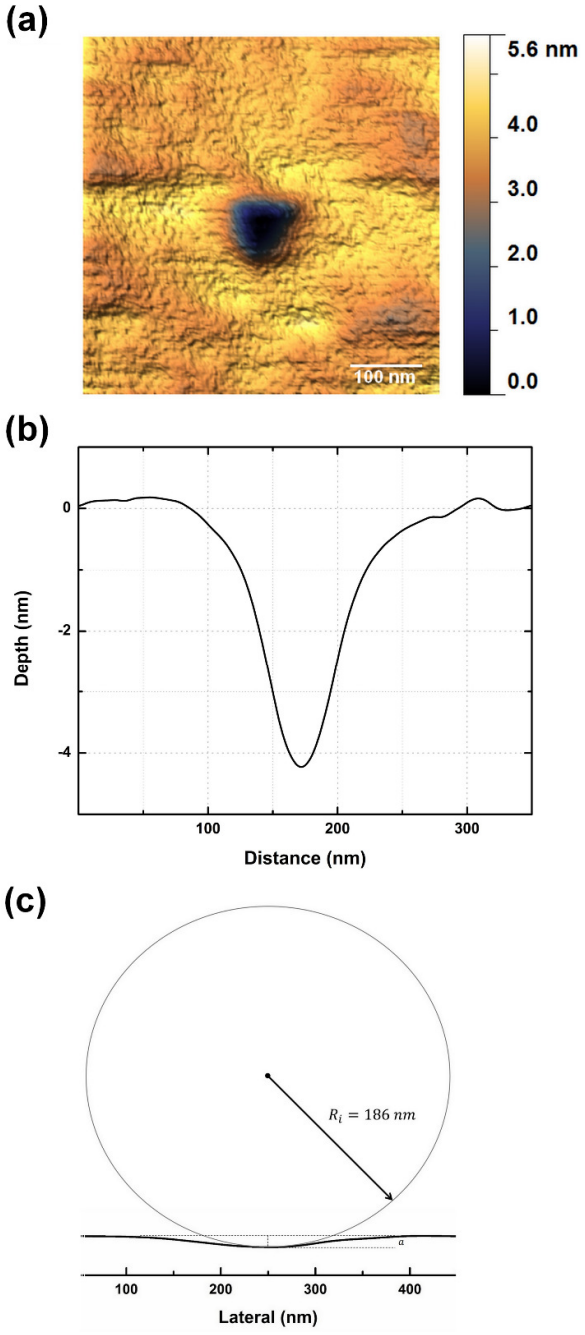

Figure 5.1. Tip radius estimation based on shallow (100 µN) indents. **(a)** *In situ* SPM scan of a 100 µN indent contact. **(b)** Contact depth profile of the 100 µN indent. **(c)** Spherical contact fitted to the 100 µN indetns.

where the effective radius of the probe (R_e) is calculated as the average between the radii of indenter's rounding sphere and the radius of the circle circumventing the projected contact area. The radius of the indenter's rounding sphere can be calculated through fitting a spherical contact to very shallow residual plastic deformations. Fitting the residual contact area for 100 µN indents (Figure 5.1), this radius is estimated to be 186±4 nm.

For extremely small penetration depths (corresponding to very low indentations loads) where the deformation behavior of platinum films is mainly elastic, the nominal electrical contact diameter can be described as the elastic contact between two bodies [5.22,23]:

$$\mathrm{d} = 2 \times \left(\frac{3}{4}\frac{\mathrm{PR}^*}{\mathrm{E}^*}\right)^{1/3} \qquad (2)$$

where R^* is the reduced radius of the two contacting spheres ($1/\mathrm{R}^* = 1/\mathrm{R}_1 + 1/\mathrm{R}_2$), P is the mechanical load and E^* is the reduced modulus. As for the electrical resistance at the nanoscale contact area (R_c), where the contact diameter is sufficiently larger than the electrons' mean free path (l), it can be described as the constriction resistance between the indenter and the platinum film in the diffusive regime, and can be related to the resistivity values (ρ_i and ρ_s for the indenter and the thin films, respectively) of contacting bodies by the Holm's equation [5.24]:

$$\mathrm{R_c} = \frac{\rho_\mathrm{i}+\rho_\mathrm{s}}{2\mathrm{d}} = \frac{\rho_\mathrm{i}+\rho_\mathrm{s}}{2\times\sqrt{2\mathrm{R_e h}-\mathrm{h}^2}} \qquad (3)$$

Equation (3) assumes a perfect contact between two nominally smooth surfaces which, as mentioned before, results in an over-estimation of the true electrical

contact area in nanoindentation experiments. Therefore, to ascertain the true resistivity values of the indenter and platinum thin films, further modifications based on empirical data are required.

Where the contact diameter is comparable to the electron's mean free-path (estimated value of ~17.1 nm for nano-crystalline platinum films) [5.25], the constriction resistance falls into the *quasi*-ballistic regime. At this limit, the resistance can be described using the Wexler correction for nanoscale contacts [5.22]:

$$R_w = \frac{4(\rho_i+\rho_s)}{3\pi d} K + \frac{\rho_i+\rho_s}{2d} \Gamma(K) \qquad (4)$$

where $K = 2l/d$ and $\Gamma(K)$ is a gamma function of unity order.

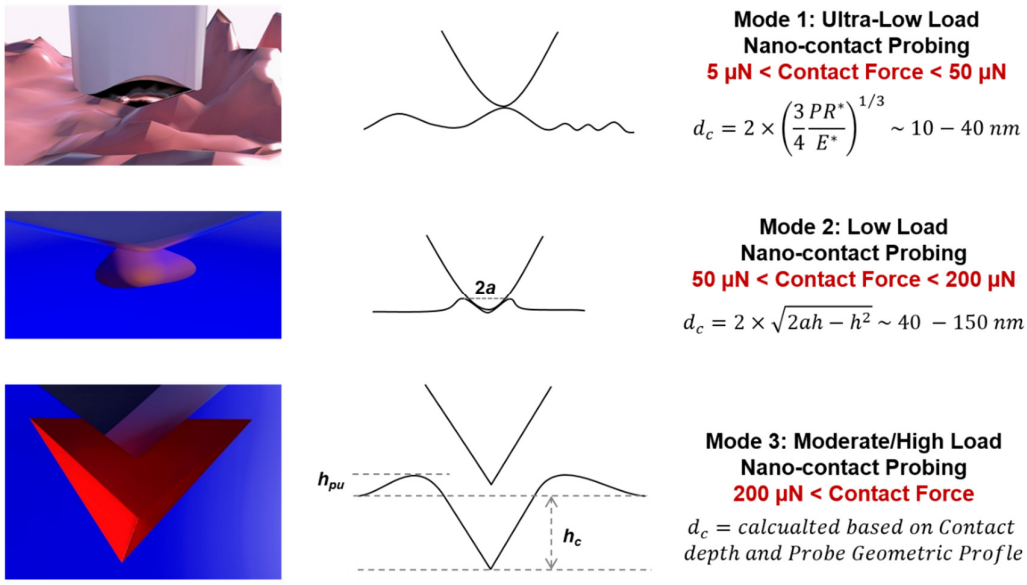

Figure 5.2. Different penetration regime in *in situ* electrical nanoindentation measurements. The measurement technique in very low-load regimes can be utilized as a conductive SPM probing technique where the SPM contact diameter and properties can be ascertained with a large degree of confidence.

Figure 5.2 summarizes the three different probe penetration regimes and highlights the appropriate contact estimation method in each of these regimes. In order to accurately assess the nano-electromechanical response of the nano-crystalline platinum films using Equations (1) to (4), the resistivity imposed by the indenter at the nanoscale contact has to be accurately assessed.

The conductive ceramic Berkovich tip used in this study has a self-similar and self-limiting three-sided pyramidal geometry. The ceramic material is vanadium carbide which has a Young's modulus of 470-500 GPa, a hardness of ~30 GPa, an average electrical resistance of 2–5 × 10^{-4} Ω.cm, and a work function of ~5.1 eV. The dynamics of the formation of the nano indentation contacts at different load/displacement points would help provide a better perspective regarding the creation of conductive paths. The conductive ceramic Berkovich tip used in this study has an average resistivity of 247.6 × 10^{-4} Ω.cm. However the resistance imposed by the tip contact at the nanoindentation contact is strongly dependent on the mechanical load and the penetration depth. The tip's geometry at small to moderate penetration depths (purely elastic and elasto-plastic contacts) cannot be assumed to be ideal. Moreover the true electrical contact area in such experiments is usually far smaller than the nominal contact area even when the contact areas are calculated using a non-ideal geometry profile.

5.2.2. Calibrations of nano-contacts resistivity profiles

For nanoindentation experiments in the elastic regime, the electrical contact can be defined as the contact between the indenter's rounding sphere and the conductive a-spot(s) on the sample surface. The imposed resistivity on the

nano-contacts engaging only the indenter's rounding sphere (933.4 μΩ.cm) is considerably higher than the average resistivity of the indenter (247.6 μΩ.cm) and is found to be uniform from the measured contact resistances at 2 μN load holding segments at the beginning and the end of the loading profile (Fig. 7 in the manuscript) and fully elastic indentation experiments (peak loads <50 μN). The value represents the maximum resistivity value for the conductive indenter's contacts and it includes the effects of imperfect contacts and drift/friction as it is derived from average contact resistances on all samples.

The case of plastic contacts is more complex due to several reasons: (i) direct estimation of the true electrical contact area is not possible as the details of the arrangement and deformation of contacting asperities are unknown; (ii) mechanical loads induce a significant drop in the contact resistance at constant penetration depths as they improve the contact between the asperities at the two sides of the contact.

Here, the real-time correlation between the mechanical and electrical response during the nanoindentation experiments have been utilized to isolate the contributions of such effects to the measured nanoscale contact resistance. The derivation of the empirical model relies on the assumption that the resistivity values of bulk gold sample and FTO coated glass do not deviate significantly from their average bulk value in the designated indentation depth/load. As such, the changes in the contact resistance subject to contact depth/load are characterized based on Holm's equation in the diffusive regime. The resistivity imposed by the conductive indenter at the nanoscale contact is then modelled based on empirical data assuming a non-uniform resistivity profile for the

conductive indenter. A further correction factor is added to account for the load effect on the imposed nano-contact resistance.

(i) Conductive probe's resistivity profile vs. indentation depth

If the nano-contact's resistivity at a given penetration depth is known, the nanoscale resistivity of the sample can be reliably assessed independent of the contact area. To address this issue, *in situ* electrical indentation experiments with loads ranging from 100-5000 μN (with multiple loading rates of 10-100 μN/s) were performed on a standard bulk gold sample with an average resistivity of 2.8 μΩ.cm. The experiments were performed in both load-controlled and depth-controlled modes to identify outliers and anomalous data resulting from surface irregularities and impurities. Aggregate contact resistivity values $(\rho_i + \rho_s)$ were calculated based on Holm's equation from contact resistance values measured at different penetration depths in the unloading curves, where the contact loads were 10-20% of the maximum indentation load. Hence, these values can be regarded as the contact resistivity at a designated depth where the effect of mechanical load is uniformly minimal, and therefore can be neglected. Figure 5.3 illustrates average resistivity values of the indenter contact *vs.* penetration depth on the bulk gold sample. These values are found to be uniform and independent of the maximum indentation loads. While the true aggregate resistivity of the nano-contact has to be constant across all penetration depths (assuming no change in the inherent electrical properties of the contacting materials), the variable modeled resistivity accounts for the evolution of the true electrical contact area as a function of nominal contact depth/area.

The aggregate resistivity settles to a constant value of 291.9 μΩ.cm at moderate penetration depths (>50 nm), where the effect of surface topography/roughness has ceased. The empirical data can be fitted to a function of logistic form to acquire the resistivity profile of the indenter *versus* the true penetration depth:

$$\rho_i = \left(\rho_{i,min} + \frac{\rho_{i,max} - \rho_{i.min}}{1 + (h/h_0)^m}\right) \qquad (5)$$

Where $\rho_{i,max}$ and $\rho_{i.min}$ are the maximum and minimum bounds of the calculated indenter resistivity, h_0 is the weighted center of the depth scale, h is the penetration depth and m is the fitting constant. FTO glass slides (ρ_{avg} = 290 μΩ.cm) were used as control samples. While the accuracy of the model for FTO indents remained intact in the moderate penetration regimes, the calculations for lower penetration depths showed a higher error margin (±10%) which can be ascribed to the significantly higher surface roughness of FTO coated glass slides (~30 nm) compared to the gold samples. As such, the function provides a very accurate real-time estimation of the resistivity imposed by the indenter at the nanoscale contact for a given contact depth.

(ii) The effect of indentation load on the nanoscale contact resistance

The mechanical pressure increases both the nominal and the true electrical contact area as the increase in the number of contact asperities and their plastic deformation (i.e. flattening) result in a net drop of constriction resistance [5.26]. On the other hand, large mechanical strain/stress has the ability to significantly modify the band structure and electrical transport properties of the material.

Therefore, the decreases in contact resistance due to the increase of electrical contact area have to be accurately isolated.

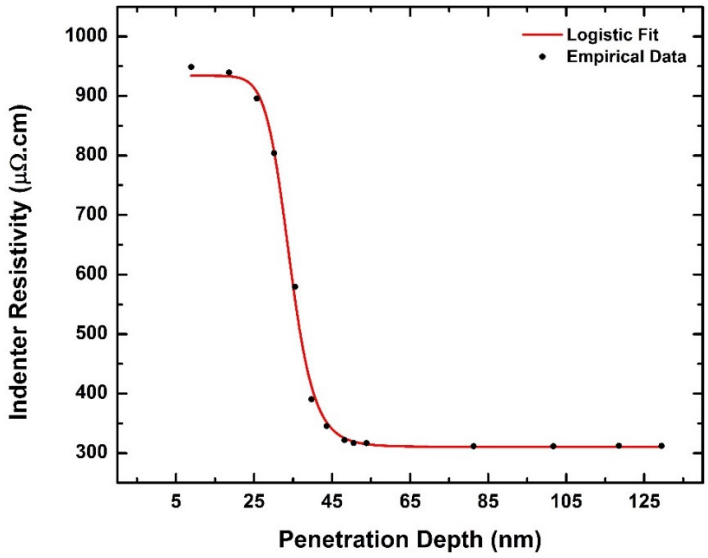

Figure 5.3. Average modeled resistivity of the indenter contact *vs.* penetration depth. The values were calculated from the contact resistivity values in the unloading curves where the contact load was 10-20% of the maximum indentation loads. The red line shows the Logistic fit of empirical data.

As such, aggregate resistivity values obtained from contact resistances of standard bulk gold sample at constant penetration depths at varying mechanical loads were used. Additionally, a set of partial load-unload experiments were performed at constant penetration depths subject to different indentation loads. Figure 5.4 shows the ratio between the resistivity calculated at higher forces to those at lower forces, at constant contact depths. As expected, calculated resistivity values at high and low loads become closer as the corresponding indentation depths are increased. This data can be used to obtain a correction component that accounts for the contact load effect on the resistivity value of

the indenter. A generalized hyperbolic function would provide a reasonable fit with the exception of loads less than 300 µN. This is mainly because of the fact that resistivity values calculated for lower load limits at a range below 300 µN are impacted by surface roughness and friction effects. Therefore, the values deviate from the trend followed by resistivity at higher loads where a reasonably large contact diameter mitigates such effects. As such, the calculated resistivity of the indenter at a constant contact diameter can be expressed in the following form after correcting for the mechanical load effect:

$$\frac{\rho_{i,H}}{\rho_{i,L}} = \left(a - \frac{b}{(1+cP)^{(1/d)}}\right) \qquad (6)$$

where $\rho_{i,L}$ and $\rho_{i,H}$ correspond to the calculated indenter resistivities at low and high loads at a constant contact depth, *P* is the maximum load on the contact and *a*, *b*, *c*, and *d* are fitting constants for the function.

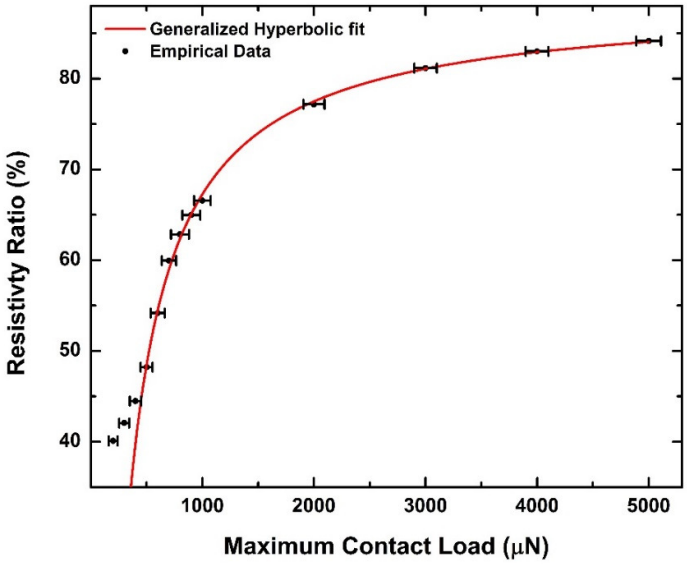

Figure 5.4. The ratio of the resistivity values calculated at high contact load to those calculated at low contact loads for constant contact depths.

Based on these analyses, an empirical based relationship between the measured contact resistance and the aggregate resistivity of the nanoscale probe and the sample can be achieved:

$$R_c = \frac{\rho_i+\rho_s}{2\times\sqrt{2R_e h-h^2}} = \left(\frac{1}{2\sqrt{2R_e h-h^2}}\right)\left[\begin{array}{l}\left(\rho_{i,min}+\frac{\rho_{i,max}-\rho_{i.min}}{1+(h/h_0)^m}\right)\\ \times\left(a-\frac{b}{(1+cP_{max})^{(1/d)}}\right)+\rho_s\end{array}\right] \quad (7)$$

It should be noted that the inherent resistivity of the conductive ceramic Berkovich probe is not expected to change subject to nanoindentation loads. However, a direct estimation of the real contact area is not possible as the current only passes through contacting asperities (conductive *a-spots*) on the two surfaces [5.26] and thus the true electrical contact area is only a fraction of the nominal contact area. Moreover, it is well known that a higher mechanical load increases the effective electrical contact area at the nanoscale contact by enhancing both the number and the size of contacting asperities [5.26].

Table 5.1. Fitting parameters for the generalized nano-contact resistance function

Fit Parameter	Value
$\rho_{i,min}$	933.4 μΩ.cm
$\rho_{i,max}$	291.9 μΩ.cm
h_0	34.1549 nm
m	10.8416
a	0.8884
b	4.948
c	0.0257
d	1.04867

Therefore, assuming a variable resistivity profile for the nanoindenter tip subject to indentation load and depth, allows for an accurate assessment of the impact

of contact area and indentation load on the true electrical nano-contact area. Equation (7) accounts for the evolution of true contact area subject to indentation load/depth. Moreover, the resistivity imposed by the indenter in the elastic contact regime (ultra-low load/penetration) is found to be uniform and is well predicted by the upper bound of the indenter's resistivity profile in Equation (7).

Therefore, the resistivity imposed by the nanoscale indenter contact is known at any indentation load/depth and the resistivity of the sample can be quantifiably assessed from the contact resistance values using Equation (7). Table 5.1 denotes the values of fitting parameters for the conductive Berkovich indenter used in this study.

5.3. Nano-Contact Electromechanical Investigations of *a*-STO Thin Films

The evolution of conductive channels due to field-dependant non-linear ionic migration along the network of point defects in *a*-STO thin films appears to play a decisive role in the switching behaviour of *a*-STO-based cells. However, it is difficult to isolate the individual contributions of the oxide layer and the electrode interfaces towards the overall conduction mechanisms that occur during the electroforming and bipolar switching events in MIM structures. To this end, *in situ* electrical nanoindentation can be employed as a powerful characterization tool as it provides stable nanoscale contacts with extremely accurate real-time control over the contact size (<5 nm in both axial and lateral dimensions) and pressure [5.12-14,18,27]. Moreover, the unrivalled mechanical load control in nanoindentation experiments and precise time-based correlation between

mechanical and electrical responses make it the premium tool to study strain-induced phenomena at the nanoscale.

In situ electrical nanoindentation technique was employed to acquire fundamental insights into the nanoionics-based conduction mechanisms in *a*-STO based devices. Throughout these *in situ* measurements, the underlying platinum substrate was uniformly forward-biased while the progressively increasing nanoscale contact area (as a function of applied mechanical force) at the surface of thin film was grounded (Figure 5.5).

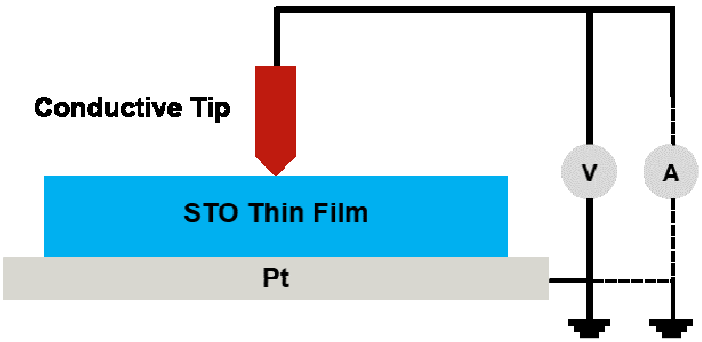

Figure 5.5. Schematic of the setup for *in situ* electrical nanoindentation experiments.

The empirical relations for the nano-contact resistance derived in the previous sections, allow to characterize and separate the effects of probe's resistance, surface adsorbates and contaminations and surface roughness effects on the contact resistance in elastic and elasto-plastic nanoindentation contacts. This allows for an accurate assessment of the *in situ* electrical nanoindentation data by eliminating the role of nano-contacts in the measured data.

5.3.1. Nano-contact studies of the conduction mechanisms in *a*-STO MIM cells

Virgin and formed *a*-STO device were investigated using nanoscale contacts with the conductive indentation probe to clarify their switching behaviour. Top

metal electrodes (50/10 nm Pt/Ti layer) were removed from 2 µm × 2 µm areas of different-sized devices *via* a precise depth limited scanning wear step. Figure 5.6a, b show the *in situ* SPM scans on the surface of virgin and formed *a*-STO devices under the top electrode. The cluster-like nano-grains (average diameter of ~80 nm) are distributed uniformly under the electrode in the formed devices (in both switching states).

Nanoscale probing of the electroformed devices was carried out using an indentation force of 100 µN with a ±250 mV voltage sweep at the maximum load (equivalent contact diameter *d* ~80 nm). Figure 5.6b, c illustrate a device area before and after indentation experiments. The nano-mechanical response of the non-deformed regions under a 100 µN indentation load is almost fully elastic. In contrast, the large plastic deformation of the nano-grains under identical loads indicate a weak mechanical structure for the nano-grains (Figure 5.6d). Further, the non-deformed regions show an insulating behaviour upon sweeps at maximum load, similar to that of the virgin devices (Figure 5.6e), whereas a bi-stable switching current transport (with an average current density of 50 A/cm^2) is observed for the nano-grains (Figure 5.6f). As such, structurally weak nano-grains with a bi-stable switching behaviour can in fact be regarded as the filamentary pathways throughout the oxide layer in *a*-STO devices. These “nano-filaments” are distributed uniformly over the device area, contributing to the bipolar switching behaviour as a parallel network. Hence, the overall increase in the oxygen vacancy concentration throughout the thickness of switching devices as characterized by XPS depth profile results denotes the formation of uniformly distributed nano-filaments upon electroforming. Previous studies into the nature of conductive filaments in redox based resistive

switching devices have typically identified localized filamentary pathways in electroformed devices [5.28-31].

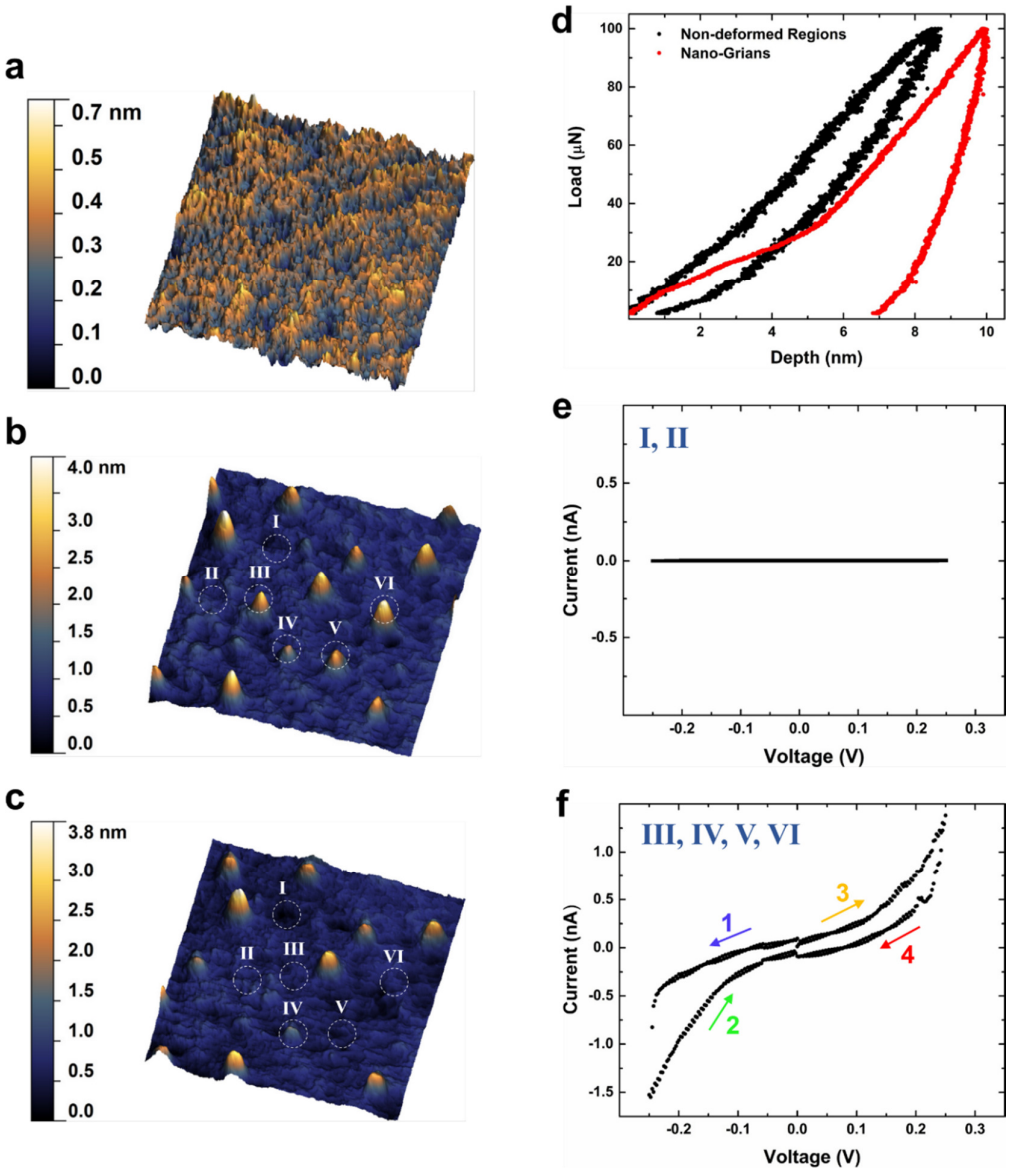

Figure 5.6. *In situ* SPM scans (1 μm × 1 μm) and electrical nanoindentation on *a*-STO MIM cells after removing the top Pt/Ti electrodes (top Ti/*a*-STO interface). **(a)** *In situ a*-STO oxide interface in a virgin cell. **(b, c)** *In situ* SPM scan of electroformed *a*-STO oxide before and after *in situ* electrical indentation with a 100 μN force (equivalent contact diameters of 80 nm), respectively. **(d)** Load-displacement curves of the non-deformed surface and nano-grains in electroformed *a*-STO cells. **(e)** Insulating current transport behaviour of non-deformed regions (I and II). **(f)** The repeatable bi-stable switching of individual nano-grains (III to VI).

Some researchers have reported evidence of homogenous conductivity in the ON state in Fe-STO thin films [5.32,33] as well as individually switchable localized point defects at single dislocations on the surface of STO single crystals [5.34-36]. However, such highly localized individually switchable nano-filaments or "nano-switches" have not been previously reported in metal–oxide MIM cells.

To further ascertain dynamics of the isolated resistive switching in nano-switches in *a*-STO MIM cells, additional ultra low-load *in situ* electrical nanoindentation measurements were carried out. Nano-contacts with an estimated diameter of ~35-40 nm were held constant on the top interface of an active *a*-STO cell in the ON state for a fixed time period (10 seconds) during ultra low-load (25 µN peak load) *in situ* electrical nanoindentation experiments. The contact load was chosen to ensure that no mechanical deformations occur upon forming the nano-contacts and *in situ* electrical measurements at peak load, in either the virgin cells or the nano-switches. During the hold period at the peak mechanical load, cyclic switching step voltages were applied and the current response and tip contact (i.e. nano-contact) displacements were recorded. This setup was used to accurately map the current transport of 2 µm × 2 µm *a*-STO cell regions through a large number (40×40 point arrays) of successive ultra low-load experiments. While the non-deformed areas in electroformed *a*-STO cells preserved their insulating properties, the nano-switches exhibited a repeatable bipolar switching behavior (Figure 5.7a). A close examination of the time correlated evolution of current transport upon applying SET and RESET voltage at the constant peak load provides further insights into the dynamical evolution of current transport in the nano-switches.

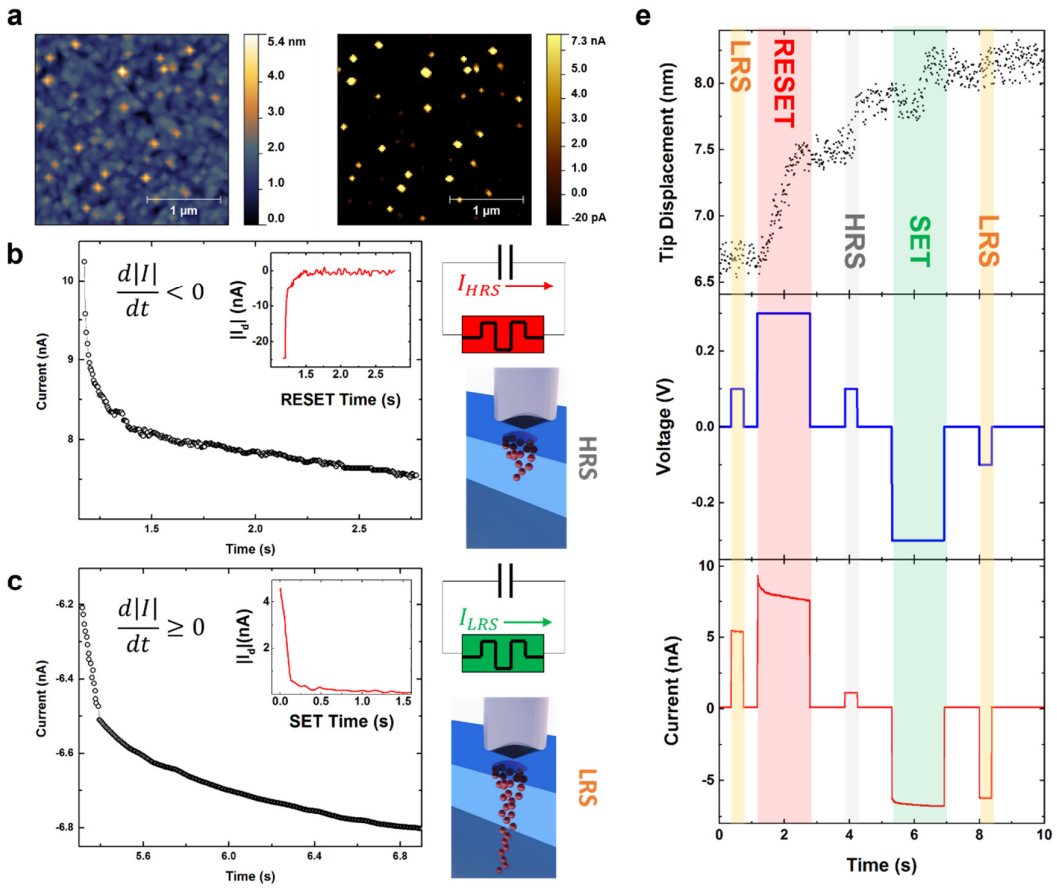

Figure 5.7. (a) *in situ* SPM image of the surface (left) and compiled area conductivity map form nano-contact probing experiments (right) of an active *a*-STO cell after removing the top metal electrode layers exhibiting distributed nano-switches and their conductivity profile compared to the non-deformed regions. **(b,c)** Time-based current evolution of a single nano-switch upon applying SET/RESET step voltages (±300 mV) at 25 µN nano-contact load. The insets show the current derivatives in for each case. The schematics show the resistive states and current directions. **(d)** Cyclic resistive switching of a single nano-switch the time-based correlation of nano-contact displacements.

Upon applying a step RESET voltage (300 mV) on the platinum electrode, diffusive charge carrier species (i.e. oxygen vacancies) move away from the bottom electrode rendering the nano-switch OFF. The current flow through the grounded top nano-contact (Figure 5.7b) strongly resembles a capacitive

discharge current where $\frac{dI}{dt} < 0$ with an almost purely exponential decay characteristics as in the simple Equation (1):

$$I = I_0 e^{-t/\tau_c} \qquad (1)$$

Assuming a capacitive current discharge process, the combined time constant of the nano-switch and the nano-contact probing system is calculated to be $\tau_c = 0.21$ s. In considering the capacitive decay time constant for nano-switches, the resistance imposed by nano-contact at 25 µN peak load has to be taken into account. At such low contact forces the nano-contact resistance is in the range of 0.15–0.25 MΩ, depending on the surface roughness and average grain size of the sample. As such, assuming a low resistance ohmic top contact, as is the case for *a*-STO MIM cells, would result in significantly reduced estimated time constants for nano-switches according to $\tau_c = RC$. It can therefore be concluded that these nano-switches are highly localized fast charge transport channels capable of fast resistive switching.

On applying a step SET voltage (-300 mV) to a nano-switch in OFF state form the platinum bottom electrode, the memristive mechanisms (the motion of oxygen vacancies towards the residual barrier at *a*-STO/Pt interface) become activated and the nano-switch switches back to ON state. The memristive regime is exemplified by a positive and decaying current derivative ($\frac{dI}{dt} \geq 0$).

Messerschmitt *et al.* have recently proposed a chronoamperometry technique [5.37] for memristors through which bias dependent memristive time-constant (τ_m) charge carrier diffusion coefficients can be experimentally extracted. The

memristive time-constant is defined as the time at which $I\sqrt{t}$ has its maximum subject to constant bias:

$$t(\tau_m) = \langle |I_{lim} - I(t)|\sqrt{t}\rangle_{max} \quad (2)$$

The time constant can be extracted from the maximum value position on $I\sqrt{t}$ vs. $1/\sqrt{t}$ plot (Figure 5.8).

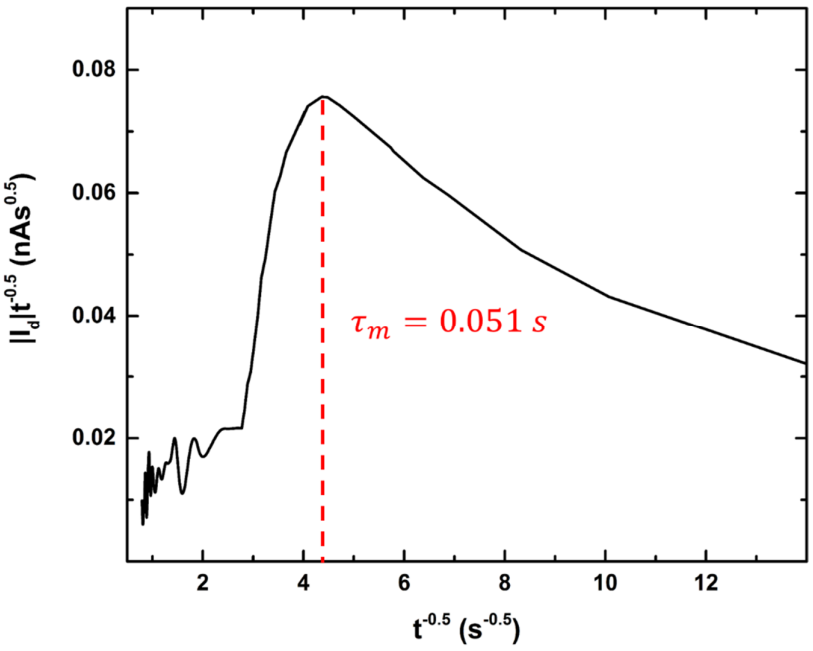

Figure 5.8. The $|I_d(t)|t^{0.5}$ vs. $t^{0.5}$ plot to derive the memristive time constant subject to full SET voltage (-300 mV).

The memristive time constant derived for nano-switches is significantly lower than the lowest time constants derived for 25 × 25 µm Pt/$SrTiO_{3-\delta}$/Pt memristive with a 600 nm oxide layer investigated by Messerschmitt *et al.* [5.37]. Besides the thickness difference, the significantly smaller active area of a nano-switch results in an extremely localized electrical field which inhibit faster switching and settling times. Moreover, PLD grown crystalline thin films used in this study did not undergo a high energy electroforming step. Nano-switches in *a*-STO

memristive cells on the other hand, are the aftermath of a high voltage electroforming step in the originally insulating devices. As a result, the presumed locally high carrier (oxygen vacancy) density confined in the extended defect structure of nano-switches results in a fast switching mechanism.

A memristive-based Cottrelll equation accounting for the vacancy movement mechanisms has been proposed by Messerschmitt *et al.* to evaluate the diffusion coefficient, D_m, based on the differential transient current data [5.37,38]:

$$D_m = \left(\frac{(I_d\sqrt{t})_{max}\sqrt{\pi}}{nFA\Delta c}\right)^2 \qquad (3)$$

Where n is the number of electrons transferred per redox process, F the Faraday constant, A the geometric electrode area and Δc is the difference between the equilibrium concentrations of diffusive species at the start and the end of the switching process. For the single direction motion of oxygen vacancies (for the maximum length, L, of the oxide thickness, between two electrodes) the charge transfer can be related to the volume (AL) as:

$$\Delta Q = nF\Delta c(AL) \qquad (4)$$

where the total charge transfer (until a limiting current is reached in the memristive regime) can be described as:

$$\Delta Q = \int_{t=0}^{\infty} I(t)dt \qquad (5)$$

Hence, it follows form Equation (3)-(5) that [5.38]:

$$D_m = \left(\frac{(I_d\sqrt{t})_{max}\sqrt{\pi}L}{\Delta Q}\right)^2 = \left(\frac{(I_d\sqrt{t})_{max}\sqrt{\pi}L}{\int_{t=0}^{\infty} I(t)dt}\right)^2 \qquad (6)$$

As the nano-contact cannot be held on top of the nano-switch for an extended period of time due to thermal drift and surface friction effects, the transient memristive current data obtained for a period of 1.5 s, was extrapolated over time using a coupled exponential decay function to reach a self-limiting current where $\frac{dI}{dt} < 10^{-11}$. The extrapolated data was then used to estimate ΔQ for a full switching period. Further, the role of the series nano-contact resistance (~200 KΩ ± 10%) has been eliminated by substituting an area-corrected resistance proportional to the overall resistance of a full MIM cell in the ON state. Assuming a diffusion length of 100 nm (the thickness of the oxide) for the nano-switch, a diffusion constant of 5.27 × 10^{-15} m^2s^{-1} was calculated for the nano-switches. The anomalously high calculated diffusion constant likely originates from an overestimation of the diffusion length; *i.e.*, the migration length of oxygen vacancies along the nano-switches for a switching transition is likely to be only a small fraction of the oxide length. Nonetheless, this demonstrates that extremely localized charge transport along the extended defect structure of nano-switches facilitates higher directional mobilities for the diffusive oxygen vacancy species. The abrupt changes in the current transport regimes can also be correlated with unique bursts in the time *vs.* displacement data observed upon switching the voltage to ±300 mV (ERASE/WRITE) values (Figure 5.7e). As evident, the structure of the grains is not altered by such low load nano-contacts (i.e. the grains are not deformed or flattened). These observed displacement bursts appear to be due to the instantaneous shift of charged species upon switching, which drastically changes the charge

equilibrium and adhesion forces at the contact area, thereby, displacing the contact [5.18,19]. These results support further experimental evidence for the oxygen vacancy related nature of memristive behavior in *a*-STO cells and nano-switches.

The formation of isolated nano-switches has to do with the amorphous nature of the functional metal oxide. While a pre-existing point-defect structure in the amorphous network facilitates the formation of filamentary pathways during the electroforming, lack of crystalline order results in a non-preferential expansion of isolated defects and effectively limits the extended defect structures to a close neighbourhood of the initial point defects. These observations signal the great potential of *a*-STO cells in terms of scalability and energy requirements for switching operations. The small dimensions and the uniform distribution of individual nano-switches indicate the ultimate scalability of these devices and their fast carrier transport mechanisms qualify them further for large area integration of memory devices.

5.3.2. Formation of conductive channels at nano-contacts: strain effect

In situ electrical nanoindentation is used to investigate in detail the nanoscale dynamics of conduction mechanisms in virgin *a*-STO/Pt stacks. As-grown *a*-STO thin films (100, 60, and 12 nm) were found to be completely insulating when probed using ultra low load nano-contacts (equivalent contact diameter $d = 80$ nm). 100 and 60 nm thin films were then subjected to a series of high voltage sweeps at progressively increasing (from 0.1 to 5 mN) indentation loads. Throughout these experiments, the nano-mechanical response of *a*-STO

thin films was monitored to ensure the ultimate nano-contact depth does not breach the film's thickness and the ultimate contact depths (upon full unloading) are kept to less than half of the thickness of the oxide layer (Figure 5.9).

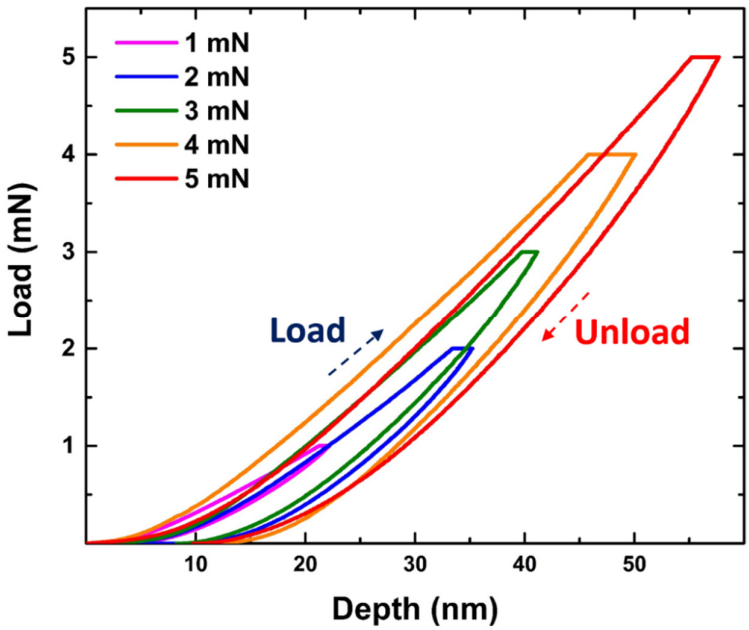

Figure 5.9. Typical load-displacement curves of 100 and 60 nm *a*-STO/Pt stacks under different maximum loads during *in situ* electrical nanoindentation experiments.

A stable Schottky transport behaviour was observed for *a*-STO/Pt stacks at stable contacts loads up to 1 mN. A dramatic non-linear increase in current density is observed at higher indentation loads (>1 mN) after accounting for the increased contact area and the non-uniform resistivity of the indenter tip (Figure 5.10a). Moreover, scanning probe microscope (SPM) scans of high-load nanoscale contact areas revealed deformations around the contact area for contact loads ≥1 mN as a direct consequence of the voltage sweep cycles (Figure 5.10b-d). Low-load nano-contact probing of the deformed regions reveals a significant uniform enhancement in electrical conductivity (Figure 5.10e) indicating the creation of conductive paths inside the oxide layer.

Based on these observations, two principal strain-related phenomena can be identified.

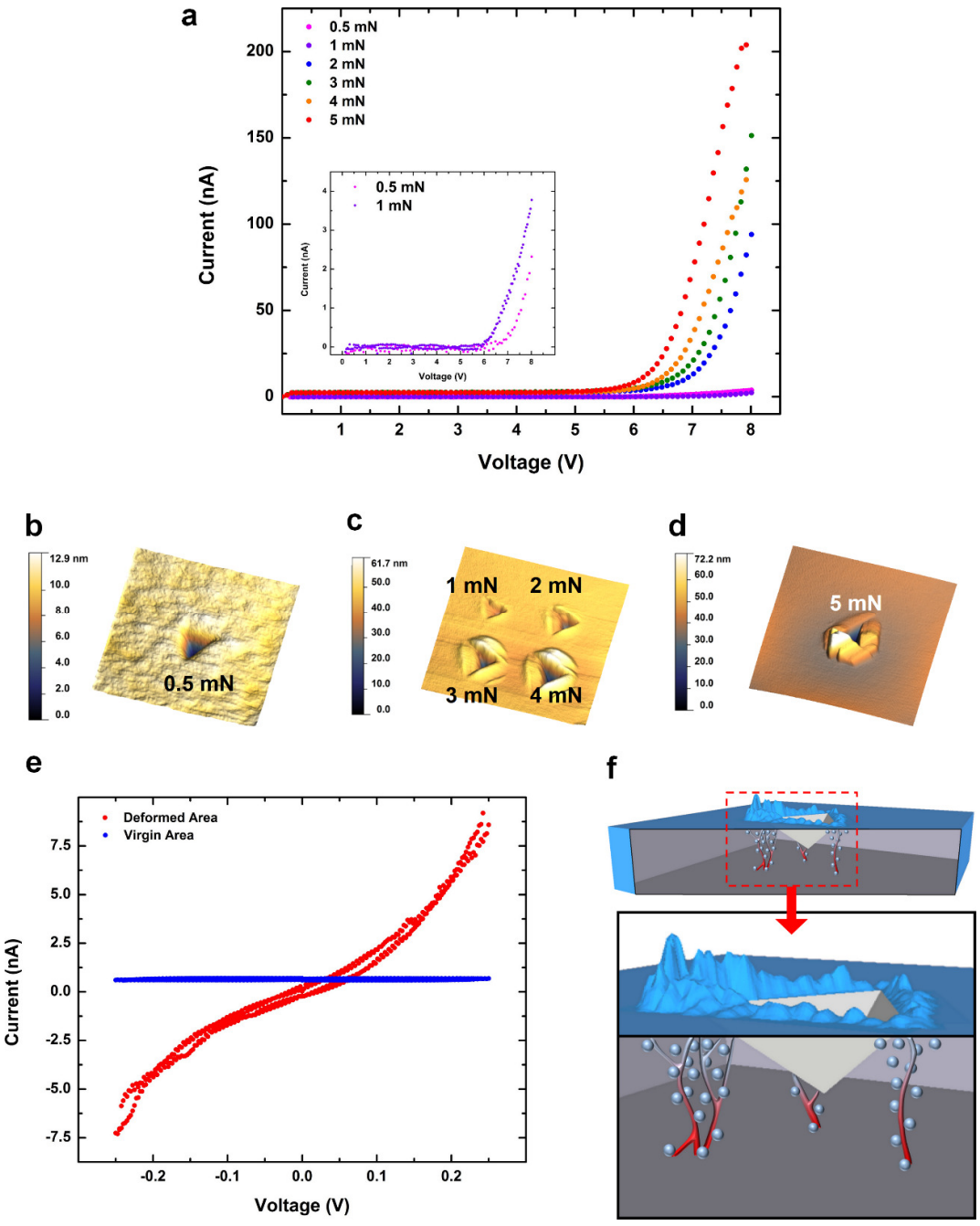

Figure 5.10. **(a)** Current transport behaviour of 60 nm *a*-STO films under increasing nanoindentation loads. **(b-d)** SPM scans of deformations around the electrical nano-contact area in 60 nm *a*-STO films under different loads after 10 cycles of high voltage sweeps under increasing maximum indentation loads. The scan area is 1 µm × 1 µm in **(b)** and 5 µm × 5 µm in

both **(c)** and **(d). (e)** Current transport of virgin and deformed regions (around the 5 mN contact area, after sweep cycles) in 60 nm *a*-STO thin films. **(f)** Schematic of formed filaments as a result of oxygen vacancies migration around the nano-contact area.

Firstly, increasing the contact load results in a corresponding decrease in the width of the depletion layer at the *a*-STO/Pt interface. This is presumably the result of enhanced carrier concentration due to increased defect density. More importantly, the application of mechanical force enhances the drift-diffusion of oxygen vacancies in the STO network [5.10,11]. Due to the geometry of the nano-contact (defined by the non-ideal geometry of the Berkovich probe and the nano-mechanical deformation of *a*-STO thin films), the majority of the electrical contact area is concentrated at the peripheral nano-contact area (rather than its center) where the number of contact asperities is larger and the topographical profiles of the contacting sides are smoother. Therefore, oxygen vacancies diffuse towards the peripheral electrical contacts in the nano-contact area through the network of pre-existing point defects, forming conductive filamentary channels *via* the creation of extended defect structures (Figure 5.10f).

5.3.3. Direct electroforming at *a*-STO/Pt interface

Nano-contact investigations were conducted on ultra-thin (12 nm) *a*-STO films to investigate the role of oxide/metal interfaces in the electroforming and switching behaviours. At such small thicknesses the short range electronic effects at the *a*-STO/Pt anode interface can be closely mimicked. Moreover, at such low dimensions the higher local densities of the point defects augment the impact of electromechanical stimuli on the interfacial electronic properties as well as the non-linear ionic transport in *a*-STO layers. Probed with ultra low-load

(50-100 µN) nano-contacts, these ultra-thin films exhibited a fully elastic mechanical behaviour and consistently maintained their highly insulating virgin characteristics (Figure 5.11) which are governed by the Schottky effect that arises due to the depletion region at the *a*-STO/Pt interface. The effect of the mechanical pressure on the transport characteristics of the interface were observed even at such small loads (Figure 5.11b).

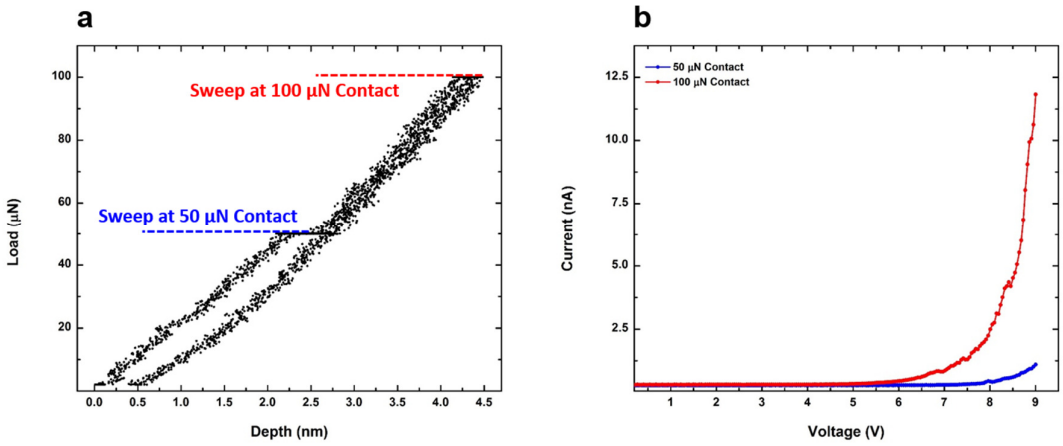

Figure 5.11. Ultra low-load nano-contact characterization of 12 nm *a*-STO/Pt stacks. **(a)** The load-displacement behavior of *a*-STO films subject to indentation loads up to 100 µN. Voltage sweeps are performed at 50 and 100 µN constant load segments (corresponding contact diameters of 40 and 80 nm respectively). **(b)** *I–V* characteristics of the stacks at 50 and 100 µN nano-contacts.

On the other hand, high voltage (up to 10 V) sweeps at 250 and 500 µN contact loads (corresponding contact diameters of 100 of 130 nm respectively) result in an abrupt deviation from the Schottky behaviour of the transport characteristics of the metal-oxide interface (Figure 5.11a,b). The critical threshold voltage is found to be proportional to the contact load. Moreover, the change in the current transport characteristics is accompanied by large displacement of the nano-contact and chaotic deformations in a large area around the contact area.

(Figure 5c,d). At voltages above the threshold value, the current transport characteristics resemble space charge limited conduction (SCLC) at the *a*-STO/Pt interface.

Such transport mechanisms require low barrier heights (e.g. a metal-n^+ oxide interface) for easy charge carrier injections into the conduction band of the oxide [5.39,40].

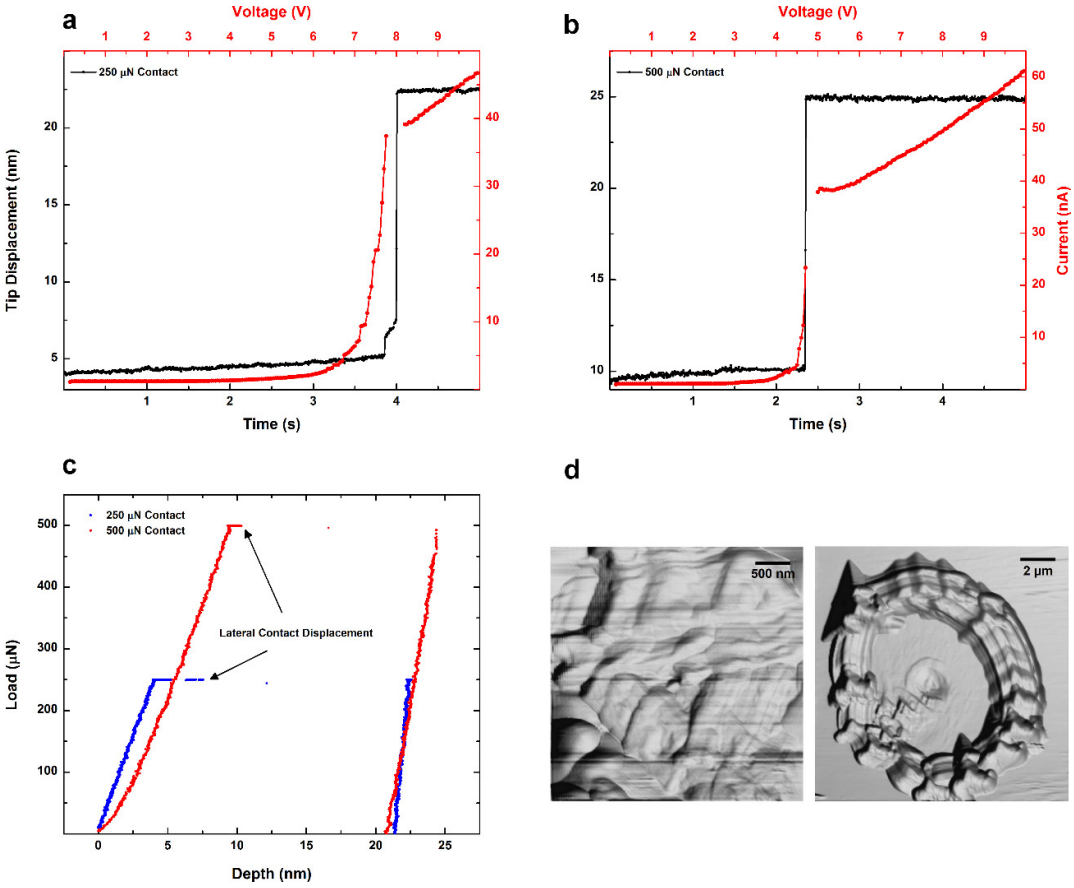

Figure 5.12. Current transport at the 12 nm *a*-STO/Pt interface at 250 and 500 µN contact loads. **(a, b)** The time/voltage correlation of abrupt change of the *I–V* characteristics and contact displacement at constant contact loads upon 10 V voltage sweeps. **(c)** Load-displacement curves of the 250 and 500 µN nano-contacts highlighting the lateral displacement of the nano-contact at constant loads upon high voltage sweeps. **(d)** Zoomed-in and large-area SPM scan of the deformed regions around the 500 µN nano-contact as a result of the high voltage sweeps.

Conductive mappings of the deformed regions utilizing low load nano-contacts (100 µN contact loads) reveal a full spectrum of conduction behaviours at localized areas in the deformed region (Figure 5.12).

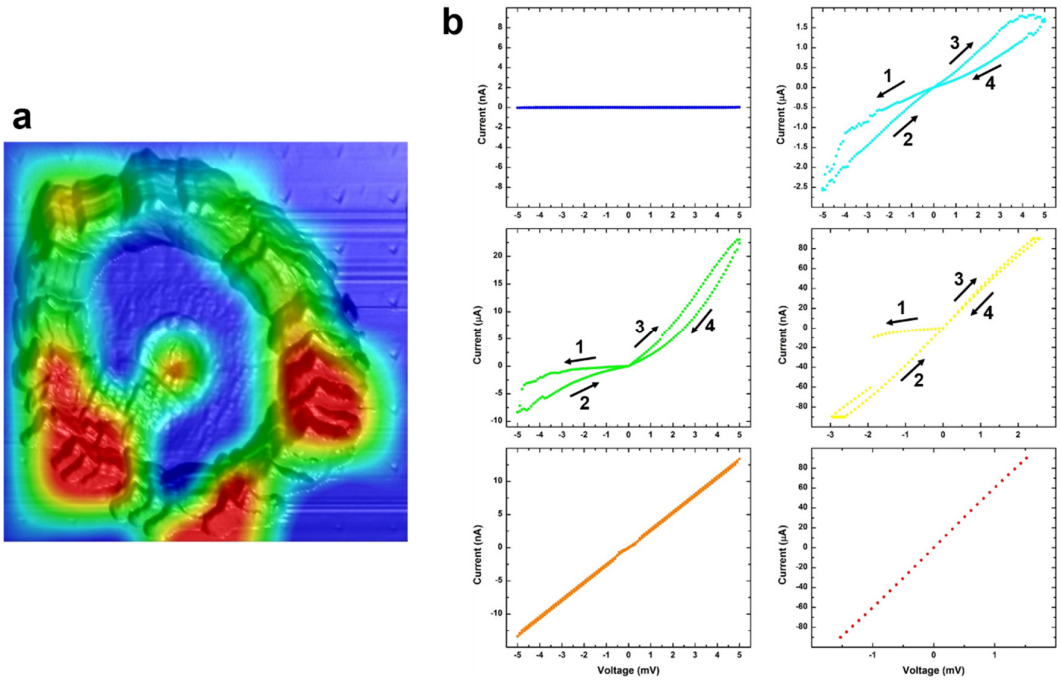

Figure 5.13. Conduction and switching characteristics of 12 nm *a*-STO/Pt stacks after direct electroforming with nanoindentation contacts. **(a)** Contour map of areas with distinct conduction characteristics in deformed 12 nm *a*-STO thin films. **(b)** Individual *I*–*V* characteristics of different regions in the deformed area (colours correspond to those of the contours map for deformed regions). Non-deformed regions retain their highly insulating properties. In the deformed region, the partial formations of strong and weak conductive channels result in distinct resistive states. Ohmic regions with high current densities are the result of a complete breakdown of electronic barrier and the formation of strong conductive filaments

This pattern indicates the localized changes in the interfacial electronic barrier and the formation of conductive pathways through the oxide layer. These observations help complete the picture of the electroforming process dynamics and subsequent switching mechanisms in *a*-STO resistive switches and further signify the assistive role of mechanical pressure in such mechanisms. The

mechanical pressure reduces the thermodynamical requirements for the drift-diffusion of frozen-in vacancy point defects in the oxide layer. As a result, subject to a sufficiently high field gradient, mechanically assisted local redox processes render the oxide layer around the nano-contact area into a highly n-type conducting state which in effect changes the electronic nature of the metal-oxide interface. Moreover, redox processes induce locally formed conductive filaments with distinct current transport characteristics.

To summarize, Nano-contact studies of *a*-STO MIM devices reveal that the electroforming step results in the formation of uniformly distributed conductive nano-filaments in the oxide layer where each of these filaments are switchable in isolation and thus act as individual resistive nano-switches. The *in situ* electrical nanoindentation experiments on *a*-STO/Pt stacks confirm the underlying electronic and ionic transport phenomena that take place during the electroforming and highlight the impact of mechanical stress on the modulation of non-linear ionic transport mechanisms in *a*-STO films. Ultra-thin *a*-STO films were directly electroformed using nanoscale contacts with controlled mechanical load. The resulting conductive filamentary regions exhibited distinct current transport and switching characteristics. These insights promise that perovskite memristors hold the key for high performance memristive systems.

CHAPTER 6

CONCLUSIONS AND FUTURE WORK

6.1. Conclusions

The PhD research project detailed in this thesis aimed to establish a comprehensive synthesis and characterization methodology for functional perovskite oxides and complex oxide based devices, specifically metal-oxide-metal (MIM) memristive devices. The research program has resulted in several significant scientific achievements, encompassing facile synthesis techniques for functional perovskite oxides on conventional substrates, realization of high performance MIM memristive devices and development of detailed experimental techniques to study nanoscale electromechanical correlations in a wide range of novel electronic materials and structures including perovskite oxides and quasi-two dimensional layers.

The results obtained during this PhD program indicate that there is still much more to be investigated with respect to the fundamental principles of functional complex oxides, correlated oxide structures and interfaces, and the use of state-of-the-art nanoscale characterization techniques to investigate thermodynamical couplings in complex oxide interfaces.

This chapter provides a brief summary of the highlights and significant outcomes of this PhD research project and outlines the scope of future work in the field.

6.1.1. Controlled synthesis of perovskite oxides

A detailed methodology for facile synthesis of functional perovskite oxides, ferro/piezoelectric potassium sodium niobate (KNN) and archetypical strontium titanate (STO), with control over their crystal structure (in case of KNN thin films), stoichiometry and sub-oxide species is established. This was achieved through characterization of perovskite oxide thin films synthesized and post-treated at different conditions.

In case of KNN, the ability to vary the concentration of alkali species and control the sub-oxide concentration through RF magnetron sputtering using a single ceramic oxide target, serves as a valuable tool to tailor the composition and in turn, tune the ferroelectric polarization and piezoelectric response of KNN thin films. Also, the ability to tailor the preferential orientation of KNN thin films adds a degree of freedom in the design of MEMS/NEMS piezo-based devices subject to multi-directional stress/strain fields.

In case of STO, the ability to tailor the as-grown oxygen deficiency, *A*-site/*B*-site dopant concentration allows for further exploration of immense potentials of STO-based functional oxides. Further, through the controlled PVD synthesis, monolithic amorphous STO thin films with thickness down to ~10 nm are realized. These oxide layers can be utilized as the functional oxide layers in facile low temperature fabrication of nanoscale devices. Distinctly dense

structure of *a*-STO oxide layers also suggest the possibility of the realization of multi-layered oxide structures with distinct oxide-oxide interfaces.

Moreover, because of the low synthesis temperature, *a*-STO thin films can be readily deposited on bio-compatible and flexible polymer substrates.

6.1.2. Realization of high performance *a*-STO based MIM memristors

Amorphous STO (*a*-STO) thin films (100 nm) with controllable as-grown oxygen deficiency induced defect structures and external dopant concentrations were synthesized as the functional layers in Pt/Ti/*a*-STO/Pt MIM cross-point devices for the first time. Devices utilizing oxygen deficient oxide layers exhibited exceptional bipolar switching performance subsequent to a single electroforming step the polarity of which can govern the switching polarity of *a*-STO cells. Consistently high switching ratios of the order of 10^3-10^4 were observed at small READ voltage/current. The conduction and switching mechanisms in *a*-STO MIM devices were investigated utilizing a large set of characterization tools. Compositional analysis on *a*-STO based devices highlight the potential of stoichiometry and defect structure control over the non-linear resistive switching performance of *a*-STO cells to attain high-performance memristive devices. Evidence of multi-filamentary non-linear ionic drift and valence exchange along a mixed valence defect structure in the TiO_2 sub-lattice are presented as the major contributors to bipolar resistive switching behavior in *a*-STO devices. Further, room temperature co-doping with donor species are shown to introduce additional energy states in the oxide band

structure, which play a significant assistive role in the electroforming and the subsequent nanoionics-based switching processes.

6.1.3. Experimental technique for nano-contact electrical and nano-electromechanical characterizations

In situ electrical nanoindentation has been utilized as a powerful tool to study the electrometrical coupling effects in ultra-thin oxide metal stacks, as well as a stable nano-contact probing technique for the investigation of nanoscale conduction mechanisms in electronic materials. To this end, an empirical relationship between the measured contact resistance and the modeled resistivity profile of the conductive indenter versus contact load/depth. This has enabled precise assessment of the nanoscale electrical properties of different material systems, encompassing nano-crystalline platinum films, *a*-STO oxide layers and quasi-two dimensional MoS_2 and MoO_3 layers at elastic and plastic nano-contacts across a wide range of contact sizes and loads.

As such, the model provides an adaptable empirical approach to gain precise quantitative insights from *in situ* electrical nanoindentation data. The experimental procedure is readily applicable for quantified *in situ* electrical measurements in material systems and complex nanostructures that exhibit a Hertzian or continuous load-displacement behavior under nanoindentation loads. As for the characteristic discontinuities in the load-displacement behavior for materials systems that undergo phase change or structural break-down, the empirical model can underpin such deviations and characterize the changes in material's resistivity solely on the basis of the contact depth. Therefore, it is an

invaluable tool for scientific investigations of nano-electromechanical properties of complex material systems.

6.1.4. Investigations of nanoscale conduction mechanisms and nano-electromechanical effects in *a*-STO oxides and devices

The *in situ* electrical nanoindentation experimental methodology and empirical relations developed as part of this PhD research project, were utilized to conduct a detailed investigation of nanoscale conduction and switching mechanisms in *a*-STO oxides. Nano-contact studies of *a*-STO MIM devices in virgin and switching states reveals that the electroforming step results in the formation of uniformly distributed conductive nano-filaments in the oxide layer where each of these filaments is switchable in isolation and thus acts as an individual resistive nano-switch. The *in situ* electrical nanoindentation experiments on a-STO/Pt stacks confirm the underlying electronic and ionic transport phenomena that take place during the electroforming and highlight the impact of mechanical stress on the modulation of non-linear ionic transport mechanisms in *a*-STO films. Ultra-thin *a*-STO films were directly electroformed using nano-scale contacts with controlled mechanical load. The resulting conductive filamentary regions exhibited distinct current transport and switching characteristics.

As such, these results highlight the multi-filamentary switching phenomena which takes place in *a*-STO MIM cells and hold the promise that *a*-STO perovskite oxides can be utilized to realize ultra-dense high performance memory and logic architectures.

6.2. Future Work

The PhD research project detailed in this thesis has provided significant insights into the novel electronics devices based on complex oxides. However, there remain numerous opportunities for continued investigations in the field of functional oxide electronics and nanoscale memristive devices and systems. Following, is a list of few significant research topics that can contribute to the advancement of the field.

6.2.1. Realization of high performance nanoscale *a*-STO based memristive arrays

Although micro-scale *a*-STO based MIM memristors demonstrated in this work show promising resistive switching performance and scaling potential, the realization of working memory and logic arrays based on nanoscale *a*-STO devices (device sizes < 200 nm) requires further refinement of the oxide defect chemistry and composition, as well as the MIM cell structure. The multi-filamentary switching phenomena in a-STO oxides and their high switching ratios hint at the ultimate scalability of *a*-STO based devices. Further downscaling of the device size (both in oxide dimensions and device size) is also an opportunity to investigate physical phenomena arising due to extreme electrical gradients and confined metal-oxide interfaces.

6.2.2. Development of physical and electronic circuit-based models for *a*-STO MIM memristors

The development of a comprehensive physical-based behavioral model for *a*-STO MIM memristors will serve as a stepping stone to better understanding the underlying device mechanisms. It will also allow for tailored design of

memristive cells with specific performance characteristics. To achieve such a physical model, the conduction and switching mechanisms as well as structural and physical parameters of *a*-STO oxide layers and interfaces need to be fully investigated. A detailed physical model will allow for the development of equivalent circuit models of *a*-STO memristive cells and the eventual integration of these devices into the conventional electronic circuit design process.

6.2.3. Design and optimization of multi-layered complex oxide structures and interfaces

The facile PVD synthesis process introduced in this project can be readily utilized to achieve optimal conditions for the realization of sub 100 nm multi-layered oxide structures. Such structures are rife with interesting and, once mastered, extremely potent physical phenomena arising from strongly correlated oxide interfaces. In case of memristive devices, multilayered *a*-STO oxide structures with disparate electronic structures and activation energies can serve as rectifier-memory building blocks in large-scale memory arrays. Further, metal-insulator transitions (IMTs) are already reported at dissimilar oxide interfaces, suggesting possibilities for the realization of different types of memristive behavior.

BIBLIOGRAPHY

Chapter 1

[1.1] Ramirez A P 2007 Oxide electronics emerge *Science* **315** 1377-8

[1.2] Reyren N, Thiel S, Caviglia A, Kourkoutis L F, Hammerl G, Richter C, Schneider C, Kopp T, Rüetschi A-S and Jaccard D 2007 Superconducting interfaces between insulating oxides *Science* **317** 1196-9

[1.3] Yang Z, Ko C and Ramanathan S 2011 Oxide electronics utilizing ultrafast metal-insulator transitions *Annual Review of Materials Research* **41** 337-67

[1.4] Mannhart J and Schlom D 2010 Oxide interfaces—an opportunity for electronics *Science* **327** 1607-11

Chapter 2

[2.1] Yang J J S, Strukov D B and Stewart D R 2013 Memristive devices for computing *Nat. Nanotechnol.* **8** 13-24

[2.2] Nguyen T D, Mao S, Yeh Y W, Purohit P K and McAlpine M C 2013 Nanoscale Flexoelectricity *Adv. Mater.* **25** 946-74

[2.3] Rondinelli J M, May S J and Freeland J W 2012 Control of octahedral connectivity in perovskite oxide heterostructures: An emerging route to multifunctional materials discovery *MRS Bulletin* **37** 261-70

[2.4] Ramirez A P 2007 Oxide electronics emerge *Science* **315** 1377-8

[2.5] Yang Z, Ko C and Ramanathan S 2011 Oxide electronics utilizing ultrafast metal-insulator transitions *Annual Review of Materials Research* **41** 337-67

[2.6] Sawa A 2008 Resistive switching in transition metal oxides *Mater. Today* **11** 28-36

[2.7] Waser R, Dittmann R, Staikov G and Szot K 2009 Redox-Based Resistive Switching Memories - Nanoionic Mechanisms, Prospects, and Challenges *Adv. Mater.* **21** 2632-63

[2.8] Santander-Syro A F, Copie O, Kondo T, Fortuna F, Pailhes S, Weht R, Qiu X G, Bertran F, Nicolaou A, Taleb-Ibrahimi A, Le Fevre P, Herranz G, Bibes M, Reyren N, Apertet Y, Lecoeur P, Barthelemy A and Rozenberg M J 2011 Two-dimensional electron gas with universal subbands at the surface of SrTiO3 *Nature* **469** 189-93

[2.9] Walia S, Balendhran S, Nili H, Zhuiykov S, Rosengarten G, Wang Q H, Bhaskaran M, Sriram S, Strano M S and Kalantar-zadeh K 2013 Transition metal oxides–Thermoelectric properties *Progress in Materials Science* **58** 1443-89

[2.10] Mannhart J and Schlom D 2010 Oxide interfaces—an opportunity for electronics *Science* **327** 1607-11

[2.11] Nguyen T D, Mao S, Yeh Y-W, Purohit P K and McAlpine M C 2013 Nanoscale Flexoelectricity *Advanced Materials* **25** 946-74

[2.12] Pershin Y V and Di Ventra M 2011 Memory effects in complex materials and nanoscale systems *Advances in Physics* **60** 145-227

[2.13] Granozio F M, Koster G and Rijnders G 2013 Functional oxide interfaces *MRS Bulletin* **38** 1017-23

[2.14] Cava R, Batlogg B, Krajewski J J, Farrow R, Rupp L, White A, Short K, Peck W and Kometani T 1988 Superconductivity near 30 K without copper: the $Ba_{0.6}K_{0.4}BiO_3$ perovskite *Nature* **332** 814-6

[2.15] Maeno Y, Hashimoto H, Yoshida K, Nishizaki S, Fujita T, Bednorz J and Lichtenberg F 1994 Superconductivity in a layered perovskite without copper *Nature* **372** 532-4

[2.16] Haeni J, Irvin P, Chang W, Uecker R, Reiche P, Li Y, Choudhury S, Tian W, Hawley M and Craigo B 2004 Room-temperature ferroelectricity in strained SrTiO3 *Nature* **430** 758-61

[2.17] Saito T, Wada T, Adachi H and Kanno I 2004 Pulsed laser deposition of high-quality (K, Na) NbO_3 thin films on $SrTiO_3$ substrate using high-density ceramic targets *Japanese Journal of Applied Physics* **43** 6627

[2.18] Shibata K, Oka F, Ohishi A, Mishima T and Kanno I 2008 Piezoelectric properties of (K, Na) NbO_3 films deposited by RF magnetron sputtering *Applied Physics Express* **1** 1501

[2.19] Wakasa Y, Kanno I, Yokokawa R, Kotera H, Shibata K and Mishima T 2011 Piezoelectric properties of microfabricated (K,Na)NbO_3 thin films *Sens. Actuator A-Phys.* **171** 223-7

[2.20] Wang L Y, Yao K and Ren W 2008 Piezoelectric $K_{0.5}Na_{0.5}NbO_3$ thick films derived from polyvinylpyrrolidone-modified chemical solution deposition *Appl. Phys. Lett.* **93**

[2.21] Blomqvist M, Khartsev S, Grishin A, Petraru A and Buchal C 2003 Optical waveguiding in magnetron-sputtered $Na_{0.5}K_{0.5}NbO_3$ thin films on sapphire substrates *Appl. Phys. Lett.* **82** 439-41

[2.22] Kan D, Terashima T, Kanda R, Masuno A, Tanaka K, Chu S, Kan H, Ishizumi A, Kanemitsu Y and Shimakawa Y 2005 Blue-light emission at room temperature from Ar^+-irradiated $SrTiO_3$ *Nat. Mater.* **4** 816-9

[2.23] Nili H, Walia S, Balendhran S, Strukov D B, Bhaskaran M and Sriram S 2014 Nanoscale Resistive Switching in Amorphous Perovskite Oxide (*a*-$SrTiO_3$) Memristors *Advanced Functional Materials*

[2.24] Dittmann R, Muenstermann R, Krug I, Park D, Menke T, Mayer J, Besmehn A, Kronast F, Schneider C M and Waser R 2012 Scaling Potential of Local Redox Processes in Memristive $SrTiO_3$ Thin-Film Devices *Proc. IEEE* **100** 1979-90

[2.25] Rodenbucher C, Speier W, Bihlmayer G, Breuer U, Waser R and Szot K 2013 Cluster-like resistive switching of $SrTiO_3$: Nb surface layers *New J. Phys.* **15** 14

[2.26] Panda P 2009 Review: environmental friendly lead-free piezoelectric materials *Journal of materials science* **44** 5049-62

[2.27] Shibata K, Suenaga K, Watanabe K, Horikiri F, Nomoto A and Mishima T 2011 Improvement of Piezoelectric Properties of (K,Na)NbO_3 Films Deposited by Sputtering *Japanese Journal of Applied Physics* **50**

[2.28] Kanno I, Mino T, Kuwajima S, Suzuki T, Kotera H and Wasa K 2007 Piezoelectric properties of (K,Na)NbO_3 thin films deposited on (001)$SrRuO_3$/Pt/MgO substrates *IEEE Trans. Ultrason. Ferroelectr. Freq. Control* **54** 2562-6

[2.29] Khartsev S I, Grishin M A and Grishin A M 2005 Characterization of heteroepitaxial $Na_{0.5}K_{0.5}NbO_3$/$La_{0.5}Sr_{0.5}CoO_3$ electro-optical cell *Appl. Phys. Lett.* **86**

[2.30] Aksel E and Jones J L 2010 Advances in Lead-Free Piezoelectric Materials for Sensors and Actuators *Sensors* **10** 1935-54

[2.31] Panda P K 2009 Review: environmental friendly lead-free piezoelectric materials *Journal of Materials Science* **44** 5049-62

[2.32] Rodel J, Jo W, Seifert K T P, Anton E M, Granzow T and Damjanovic D 2009 Perspective on the Development of Lead-free Piezoceramics *Journal of the American Ceramic Society* **92** 1153-77

[2.33] Safari A and Abazari M 2010 Lead-Free Piezoelectric Ceramics and Thin Films *IEEE Trans. Ultrason. Ferroelectr. Freq. Control* **57** 2165-76

[2.34] Shrout T R and Zhang S 2007 Lead-free piezoelectric ceramics: Alternatives for PZT? (vol 19, 2007) *J. Electroceram.* **19** 185-

[2.35] Ahtee M and Hewat A W 1978 Structrual Phase-Transition In Sodium-Potassium Niobate Solid-Solutions By Neutron Powder Diffraction *Acta Crystallogr. Sect. A* **34** 309-17

[2.36] Ahtee M and Hewat A W 1975 Structures of $Na_{0.98}K_{0.02}NbO_3$ and $Na_{0.90}K_{0.10}NbO_3$ (Phase-*Q*) at room-temperature by neutron powder diffraction *Acta Crystallogr. Sect. A* **31** 846-50

[2.37] Ahtee M and Hewat A W 1978 Structural phase-transitions in solium-potassium niobate solid-solutions by neutron powder diffraction *Acta Crystallogr. Sect. A* **34** 309-17

[2.38] Shirane G, Newnham R and Pepinsky R 1954 Dielectric Properties And Phase Transition OF $NaNbO_3$ And $(Na,K)NbO_3$ *Physical Review* **96** 581-8

[2.39] The Crystal Structure of NKN (URL: http://groups.ist.utl.pt/rschwarz/rschwarzgroup_files/Ferroelectrics_files/NOLEAD2.htm)

[2.40] Abazari M and Safari A 2009 Effects of doping on ferroelectric properties and leakage current behavior of KNN-LT-LS thin films on $SrTiO_3$ substrate *Journal of Applied Physics* **105**

[2.41] Guo Y P, Kakimoto K and Ohsato H 2005 $(Na_{0.5}K_{0.5})NbO_3$-$LiTaO_3$ Lead-Free Piezoelectric Ceramics *Mater. Lett.* **59** 241-4

[2.42] Hollenstein E, Davis M, Damjanovic D and Setter N 2005 Piezoelectric properties of Li- and Ta-modified $(K_{0.5}Na_{0.5})NbO_3$ ceramics *Appl. Phys. Lett.* **87**

[2.43] Abazari M, Choi T, Cheong S W and Safari A 2010 Nanoscale characterization and local piezoelectric properties of lead-free KNN-LT-LS thin films *J. Phys. D-Appl. Phys.* **43**

[2.44] Szot K, Speier W, Bihlmayer G and Waser R 2006 Switching the electrical resistance of individual dislocations in single-crystalline $SrTiO_3$ *Nat. Mater.* **5** 312-20

[2.45] Brinkman A, Huijben M, Van Zalk M, Huijben J, Zeitler U, Maan J, Van der Wiel W, Rijnders G, Blank D and Hilgenkamp H 2007 Magnetic effects at the interface between non-magnetic oxides *Nat. Mater.* **6** 493-6

[2.46] Bert J A, Kalisky B, Bell C, Kim M, Hikita Y, Hwang H Y and Moler K A 2011 Direct imaging of the coexistence of ferromagnetism and superconductivity at the LaAlO3/SrTiO3 interface *Nature physics* **7** 767-71

[2.47] Muenstermann R, Menke T, Dittmann R and Waser R 2010 Coexistence of Filamentary and Homogeneous Resistive Switching in Fe-Doped $SrTiO_3$ Thin-Film Memristive Devices *Adv. Mater.* **22** 4819-22

[2.48] Cen C, Thiel S, Hammerl G, Schneider C, Andersen K, Hellberg C, Mannhart J and Levy J 2008 Nanoscale control of an interfacial metal–insulator transition at room temperature *Nat. Mater.* **7** 298-302

[2.49] Reyren N, Thiel S, Caviglia A, Kourkoutis L F, Hammerl G, Richter C, Schneider C, Kopp T, Rüetschi A-S and Jaccard D 2007 Superconducting interfaces between insulating oxides *Science* **317** 1196-9

[2.50] Ueno K, Nakamura S, Shimotani H, Ohtomo A, Kimura N, Nojima T, Aoki H, Iwasa Y and Kawasaki M 2008 Electric-field-induced superconductivity in an insulator *Nat. Mater.* **7** 855-8

[2.51] Jang H W, Kumar A, Denev S, Biegalski M D, Maksymovych P, Bark C W, Nelson C T, Folkman C M, Baek S H, Balke N, Brooks C M, Tenne D A, Schlom D G, Chen L Q, Pan X Q, Kalinin S V, Gopalan V and Eom C B 2010 Ferroelectricity in Strain-Free $SrTiO_3$ Thin Films *Phys. Rev. Lett.* **104** 4

[2.52] Kan D, Terashima T, Kanda R, Masuno A, Tanaka K, Chu S, Kan H, Ishizumi A, Kanemitsu Y, Shimakawa Y and Takano M 2005 Blue-light emission at room temperature from Ar+-irradiated SrTiO3 *Nat Mater* **4** 816-9

[2.53] Hou J, Nonnenmann S S, Qin W and Bonnell D A 2014 Size Dependence of Resistive Switching at Nanoscale Metal-Oxide Interfaces *Advanced Functional Materials* n/a-n/a

[2.54] Tomio T, Miki H, Tabata H, Kawai T and Kawai S 1994 Control of electrical conductivity in laser deposited SrTiO3 thin films with Nb doping *Journal of applied physics* **76** 5886-90

[2.55] Guo X, Chen X, Sun Y, Sun L, Zhou X and Lu W 2003 Electronic band structure of Nb doped $SrTiO_3$ from first principles calculation *Physics Letters A* **317** 501-6

[2.56] Merkle R and Maier J 2008 How Is Oxygen Incorporated into Oxides? A Comprehensive Kinetic Study of a Simple Solid-State Reaction with SrTiO3 as a Model Material *Angewandte Chemie International Edition* **47** 3874-94

[2.57] Strukov D B and Kohlstedt H 2012 Resistive switching phenomena in thin films: Materials, devices, and applications *Mrs Bulletin* **37** 108-17

[2.58] Chua L 1971 Memristor-the missing circuit element *Circuit Theory, IEEE Transactions on* **18** 507-19

[2.59] Chua L O and Kang S M 1976 Memristive devices and systems *Proceedings of the IEEE* **64** 209-23

[2.60] Strukov D B, Snider G S, Stewart D R and Williams R S 2008 The missing memristor found *Nature* **453** 80-3

[2.61] Strukov D and Williams R S 2009 Exponential ionic drift: fast switching and low volatility of thin-film memristors *Appl. Phys. A* **94** 515-9

[2.62] Dignam M 1968 Ion transport in solids under conditions which include large electric fields *Journal of Physics and Chemistry of Solids* **29** 249-60

[2.63] Yang J J, Inoue I H, Mikolajick T and Hwang C S 2012 Metal oxide memories based on thermochemical and valence change mechanisms *MRS Bulletin* **37** 131-7

[2.64] Dietz G W, Antpohler W, Klee M and Waser R 1995 Electrode infulence on the charge-transport through $SrTiO_3$ thin-films *Journal of Applied Physics* **78** 6113-21

[2.65] Lenser C, Connell Z, Kovács A, Dunin-Borkowski R, Köhl A, Waser R and Dittmann R 2013 Identification of screw dislocations as fast-forming sites in Fe-doped $SrTiO_3$ *Applied Physics Letters* **102** 183504

[2.66] Lenser C, Kuzmin A, Purans J, Kalinko A, Waser R and Dittmann R 2012 Probing the oxygen vacancy distribution in resistive switching Fe-$SrTiO_3$ metal-insulator-metal-structures by micro-x ray absorption near-edge structure *Journal of Applied Physics* **111**

[2.67] Shibuya K, Dittmann R, Mi S B and Waser R 2010 Impact of Defect Distribution on Resistive Switching Characteristics of Sr_2TiO_4 Thin Films *Adv. Mater.* **22** 411-4

[2.68] Stille S, Lenser C, Dittmann R, Koehl A, Krug I, Muenstermann R, Perlich J, Schneider C M, Klemradt U and Waser R 2012 Detection of filament formation in forming-free resistive switching $SrTiO_3$ devices with Ti top electrodes *Appl. Phys. Lett.* **100** 4

[2.69] Kowalczyk S P, McFeely F R, Ley L, Gritsyna V T and Shirley D A 1977 The electronic structure of $SrTiO_3$ and some simple related oxides (MgO, Al_2O_3, SrO, TiO_2) *Solid State Communications* **23** 161-9

[2.70] Basletic M, Maurice J L, Carretero C, Herranz G, Copie O, Bibes M, Jacquet E, Bouzehouane K, Fusil S and Barthelemy A 2008 Mapping the spatial distribution of charge carriers in LaAlO3/SrTiO3 heterostructures *Nat Mater* **7** 621-5

[2.71] De Souza R A, Metlenko V, Park D and Weirich T E 2012 Behavior of oxygen vacancies in single-crystal $SrTiO_3$: Equilibrium distribution and diffusion kinetics *Physical Review B* **85** 174109

[2.72] Janotti A, Steiauf D and Van de Walle C G 2011 Strain effects on the electronic structure of $SrTiO_3$: Toward high electron mobilities *Physical Review B* **84** 201304

[2.73] Rondinelli J M and Spaldin N A 2011 Structure and Properties of Functional Oxide Thin Films: Insights From Electronic-Structure Calculations *Advanced Materials* **23** 3363-81

[2.74] Tufte O and Chapman P 1967 Electron mobility in semiconducting strontium titanate *Physical Review* **155** 796

[2.75] Jia C, Lentzen M and Urban K 2003 Atomic-resolution imaging of oxygen in perovskite ceramics *Science* **299** 870-3

[2.76] Waser R and Aono M 2007 Nanoionics-based resistive switching memories *Nat. Mater.* **6** 833-40

[2.77] Menzel S, Waters M, Marchewka A, Bottger U, Dittmann R and Waser R 2011 Origin of the Ultra-nonlinear Switching Kinetics in Oxide-Based Resistive Switches *Advanced Functional Materials* **21** 4487-92

[2.78] Hofman W, Hoffmann S and Waser R 1997 Dopant influence on dielectric losses, leakage behaviour, and resistance degradation of $SrTiO_3$ thin films *Thin Solid Films* **305** 66-73

[2.79] Waser R and Klee M 1992 Theory of conduction and breakdown in perovskite thin films *Integrated Ferroelectrics* **2** 23-40

[2.80] Menke T, Dittmann R, Meuffels P, Szot K and Waser R 2009 Impact of the electroforming process on the device stability of epitaxial Fe-doped $SrTiO_3$ resistive switching cells *Journal of Applied Physics* **106** 114507

[2.81] De Hosson J T M 2009 Advances in transmission electron microscopy: In situ straining and in situ compression experiments on metallic glasses *Microsc. Res. Tech.* **72** 250-60

[2.82] Hohmann-Marriott M F, Sousa A A, Azari A A, Glushakova S, Zhang G, Zimmerberg J and Leapman R D 2009 Nanoscale 3D cellular imaging by axial scanning transmission electron tomography *Nat Meth* **6** 729-31

[2.83] Morgan A B and Gilman J W 2003 Characterization of polymer-layered silicate (clay) nanocomposites by transmission electron microscopy and X-ray diffraction: A comparative study *J. Appl. Polym. Sci.* **87** 1329-38

[2.84] Muller D A 2009 Structure and bonding at the atomic scale by scanning transmission electron microscopy *Nat. Mater.* **8** 263-70

[2.85] Schroder D K 2010 Nano Characterization of Materials *ECS Transactions* **33** 3-22

[2.86] Varela M, Lupini A R, Benthem K v, Borisevich A Y, Chisholm M F, Shibata N, Abe E and Pennycook S J 2005 Materials characterization in the aberration-corrected scanning transmission electron microscope *Annual Review of Materials Research* **35** 539-69

[2.87] Loos J 2005 The Art of SPM: Scanning Probe Microscopy in Materials Science *Adv. Mater.* **17** 1821-33

[2.88] Park J Y, Maier S, Hendriksen B and Salmeron M 2010 Sensing current and forces with SPM *Mater. Today* **13** 38-45

[2.89] Garleff J K, Wijnheijmer A P and Koenraad P M 2011 Challenges in cross-sectional scanning tunneling microscopy on semiconductors *Semicond. Sci. Technol.* **26** 064001

[2.90] Tourek C J and Sundararajan S 2010 Atom Scale Characterization of the Near Apex Region of an Atomic Force Microscope Tip *Microsc. Microanal.* **16** 636-42

[2.91] Bombis C, Kalashnyk N, Xu W, Lægsgaard E, Besenbacher F and Linderoth T R 2009 Hydrogen-Bonded Molecular Networks of Melamine and Cyanuric Acid on Thin Films of NaCl on Au(111) *Small* **5** 2177-82

[2.92] Lee J, Choi I, Hong S, Lee S, Yang Y I, Kim Y and Yi J 2008 Construction of pcAFM module to measure photoconductance with a nanoscale spatial resolution *Ultramicroscopy* **108** 1090-3

[2.93] Reid O G, Munechika K and Ginger D S 2008 Space charge limited current measurements on conjugated polymer films using conductive atomic force microscopy *Nano Lett.* **8** 1602-9

[2.94] Xu D, Watt G D, Harb J N and Davis R C 2005 Electrical conductivity of ferritin proteins by conductive AFM *Nano Lett.* **5** 571-7

[2.95] Seemann L, Stemmer A and Naujoks N 2007 Local surface charges direct the deposition of carbon nanotubes and fullerenes into nanoscale patterns *Nano Lett.* **7** 3007-12

[2.96] Bogan M J, Benner W H, Boutet S, Rohner U, Frank M, Barty A, Seibert M M, Maia F, Marchesini S, Bajt S, Woods B, Riot V, Hau-Riege S P, Svenda M, Marklund E, Spiller E, Hajdu J and Chapman H N 2007 Single Particle X-ray Diffractive Imaging *Nano Lett.* **8** 310-6

[2.97] de Smit E, Swart I, Creemer J F, Hoveling G H, Gilles M K, Tyliszczak T, Kooyman P J, Zandbergen H W, Morin C, Weckhuysen B M and de Groot F M F 2008 Nanoscale chemical imaging of a working catalyst by scanning transmission X-ray microscopy *Nature* **456** 222-5

[2.98] Larson B C, Yang W, Ice G E, Budai J D and Tischler J Z 2002 Three-dimensional X-ray structural microscopy with submicrometre resolution *Nature* **415** 887-90

[2.99] Robinson I and Harder R 2009 Coherent X-ray diffraction imaging of strain at the nanoscale *Nat Mater* **8** 291-8

[2.100] Sakdinawat A and Attwood D 2010 Nanoscale X-ray imaging *Nat. Photon.* **4** 840-8

[2.101] Li X, Chasiotis I and Kitamura T 2010 In Situ Scanning Probe Microscopy Nanomechanical Testing *MRS Bull.* **35** 361-7

[2.102] Oliver W C and Pharr G M 2010 Nanoindentation in materials research: Past, present, and future *MRS Bull.* **35** 897-907

[2.103] Marks L D, Warren O L, Minor A M and Merkle A P 2008 Tribology in Full View *MRS Bull.* **33** 1168-73

[2.104] Fang L, Muhlstein C L, Collins J G, Romasco A L and Friedman L H 2008 Continuous electrical *in situ* contact area measurement during instrumented indentation *J. Mater. Res.* **23** 2480-5

[2.105] Nowak J, Major R, Oh J, Shan Z, Asif S and Warren O 2010 Developments in In Situ Nanomechanical Testing *Microsc. Microanal.* **16** 462-3

[2.106] Clarke D R, Kroll M C, Kirchner P D, Cook R F and Hockey B J 1988 Amorphization and Conductivity of Silicon and Germanium Induced by Indentation *Phys. Rev. Lett.* **60** 2156-9

[2.107] Pharr G M, Oliver W C, Cook R F, Kirchner P D, Kroll M C, Dinger T R and Clarke D R 1992 Electrical resistance of metallic contacts on silicon and germanium during indentation *J. Mater. Res.* **7** 961-72

[2.108] Bradby J E, Williams J S and Swain M V 2003 In situ electrical characterization of phase transformations in Si during indentation *Phys. Rev. B* **67** 085205

[2.109] Ruffell S, Bradby J E, Fujisawa N and Williams J S 2007 Identification of nanoindentation-induced phase changes in silicon by in situ electrical characterization *J. Appl. Phys.* **101** 083531

[2.110] Ruffell S, Bradby J E, Williams J S and Warren O L 2007 An in situ electrical measurement technique via a conducting diamond tip for nanoindentation in silicon *J. Mater. Res.* **22** 578-86

[2.111] Fujisawa N, Ruffell S, Bradby J E, Williams J S, Haberl B and Warren O L 2009 Understanding pressure-induced phase-transformation behavior in silicon through in situ electrical probing under cyclic loading conditions *J. Appl. Phys.* **105** 106111

[2.112] Mylvaganam K, Zhang L C, Eyben P, Mody J and Vandervorst W 2009 Evolution of metastable phases in silicon during nanoindentation: mechanism analysis and experimental verification *Nanotechnol.* **20** 305705

[2.113] Nguyen H H, Wei P J and Lin J F 2011 Electric contact resistance for monitoring nanoindentation-induced delamination *Adv. Nat. Sci.: Nanosci. Nanotechnol.* **2** 015007

[2.114] Nowak R, Chrobak D, Nagao S, Vodnick D, Berg M, Tukiainen A and Pessa M 2009 An electric current spike linked to nanoscale plasticity *Nat. Nanotechnol.* **4** 287-91

[2.115] Giannakopoulos A E and Suresh S 1999 Theory of indentation of piezoelectric materials *Acta Mater.* **47** 2153-64

[2.116] Sridhar S, Giannakopoulos A E, Suresh S and Ramamurty U 1999 Electrical response during indentation of piezoelectric materials: A new method for material characterization *J. Appl. Phys.* **85** 380-7

[2.117] Sridhar S, Giannakopoulos A E and Suresh S 2000 Mechanical and electrical responses of piezoelectric solids to conical indentation *J. Appl. Phys.* **87** 8451-6

[2.118] Algueró M, Bushby A J, Reece M J, Poyato R, Ricote J, Calzada M L and Pardo L 2001 Stress-induced depolarization of (Pb,La)TiO_3 ferroelectric thin films by nanoindentation *Appl. Phys. Lett.* **79** 3830-2

[2.119] Algueró M, Calzada M L, Bushby A J and Reece M J 2004 Ferroelectric hysteresis loops of (Pb,Ca)TiO_3 thin films under spherical indentation *Appl. Phys. Lett.* **85** 2023-5

[2.120] Koval V, Reece M J and Bushby A J 2005 Ferroelectric/ferroelastic behavior and piezoelectric response of lead zirconate titanate thin films under nanoindentation *J. Appl. Phys.* **97** 074301

[2.121] Rar A, Pharr G M, Oliver W C, Karapetian E and Kalinin S V 2006 Piezoelectric nanoindentation *J. Mater. Res.* **21** 552-6

[2.122] Sriram S, Bhaskaran M, Holland A S, Short K T and Latella B A 2007 Measurement of high piezoelectric response of strontium-doped lead zirconate titanate thin films using a nanoindenter *J. Appl. Phys.* **101** 104910

[2.123] Sriram S, Bhaskaran M and Mitchell A 2010 Low-temperature deposition of high-response piezoelectric thin films *Scripta Mater.* **63** 189-91

[2.124] Bhaskaran M, Sriram S, Ruffell S and Mitchell A 2011 Nanoscale characterization of energy generation from piezoelectric thin films *Advanced Functional Materials* **21** 2251-7

Chapter 3

[3.1] Guo Y P, Kakimoto K and Ohsato H 2005 $(Na_{0.5}K_{0.5})NbO_3$-$LiTaO_3$ Lead-Free Piezoelectric Ceramics *Mater. Lett.* **59** 241-4

[3.2] Hollenstein E, Davis M, Damjanovic D and Setter N 2005 Piezoelectric properties of Li- and Ta-modified $(K_{0.5}Na_{0.5})NbO_3$ ceramics *Appl. Phys. Lett.* **87**

[3.3] Saito T, Wada T, Adachi H and Kanno I 2004 Pulsed laser deposition of high-quality (K, Na) NbO_3 thin films on $SrTiO_3$ substrate using high-density ceramic targets *Japanese Journal of Applied Physics* **43** 6627

[3.4] Shirane G, Newnham R and Pepinsky R 1954 Dielectric Properties And Phase Transition OF $NaNbO_3$ And (Na,K)NbO_3 *Physical Review* **96** 581-8

[3.5] Blomqvist M, Khartsev S, Grishin A, Petraru A and Buchal C 2003 Optical waveguiding in magnetron-sputtered $Na_{0.5}K_{0.5}NbO_3$ thin films on sapphire substrates *Appl. Phys. Lett.* **82** 439-41

[3.6] Khartsev S I, Grishin M A and Grishin A M 2005 Characterization of heteroepitaxial $Na_{0.5}K_{0.5}NbO_3$/$La_{0.5}Sr_{0.5}CoO_3$ electro-optical cell *Appl. Phys. Lett.* **86**

[3.7] Lee H J, Ahn C W, Kang S H, Kim I W, Lee J S and Jin B M 2006 The ferroelectric properties of $(Na_{0.5}K_{0.5})NbO_3$ thin films fabricated by RF-magnetron sputtering *Ferroelectrics* **335** 227-32

[3.8] Kanno I, Ichida T, Adachi K, Kotera H, Shibata K and Mishima T 2012 Power-generation performance of lead-free (K, Na) NbO_3 piezoelectric thin-film energy harvesters *Sensors and Actuators A: Physical*

[3.9] Shibata K, Oka F, Ohishi A, Mishima T and Kanno I 2008 Piezoelectric properties of (K, Na) NbO_3 films deposited by RF magnetron sputtering *Applied Physics Express* **1** 1501

[3.10] Wakasa Y, Kanno I, Yokokawa R, Kotera H, Shibata K and Mishima T 2011 Piezoelectric properties of microfabricated (K,Na)NbO_3 thin films *Sens. Actuator A-Phys.* **171** 223-7

[3.11] Tanaka K, Kakimoto K and Ohsato H 2006 Fabrication of highly oriented lead-free (Na, K)NbO_3 thin films at low temperature by sol-gel process *J. Cryst. Growth* **294** 209-13

[3.12] Lai F P and Li J F 2007 Sol-gel processing and characterization of (Na,K)NbO_3 lead-free ferroelectric films *Ferroelectrics* **358** 1063-9

[3.13] Wang L Y, Yao K and Ren W 2008 Piezoelectric $K_{0.5}Na_{0.5}NbO_3$ thick films derived from polyvinylpyrrolidone-modified chemical solution deposition *Appl. Phys. Lett.* **93**

[3.14] Ahn C W, Lee S Y, Lee H J, Ullah A, Bae J S, Jeong E D, Choi J S, Park B H and Kim I W 2009 The effect of K and Na excess on the ferroelectric and piezoelectric properties of $K_{0.5}Na_{0.5}NbO_3$ thin films *J. Phys. D-Appl. Phys.* **42**

[3.15] Abazari M, Choi T, Cheong S W and Safari A 2010 Nanoscale characterization and local piezoelectric properties of lead-free KNN-LT-LS thin films *J. Phys. D-Appl. Phys.* **43**

[3.16] Abazari M and Safari A 2009 Effects of doping on ferroelectric properties and leakage current behavior of KNN-LT-LS thin films on $SrTiO_3$ substrate *Journal of Applied Physics* **105**

[3.17] Wang X, Olafsson S, Madsen L D, Rudner S, Ivanov I P, Grishin A and Helmersson U 2002 Growth and characterization of $Na_{0.5}K_{0.5}NbO_3$ thin films on polycrystalline $Pt_{80}Ir_{20}$ substrates *J. Mater. Res.* **17** 1183-91

[3.18] Kugler V M, Soderlind F, Music D, Helmersson U, Andreasson J and Lindback T 2003 Low temperature growth and characterization of (Na,K)NbO_x thin films *J. Cryst. Growth* **254** 400-4

[3.19] Kanno I, Mino T, Kuwajima S, Suzuki T, Kotera H and Wasa K 2007 Piezoelectric properties of (K,Na)NbO_3 thin films deposited on (001)$SrRuO_3$/Pt/MgO substrates *IEEE Trans. Ultrason. Ferroelectr. Freq. Control* **54** 2562-6

[3.20] Shibata K, Oka F, Nomoto A, Mishima T and Kanno I 2008 Crystalline structure of highly piezoelectric (K, Na) NbO_3 films deposited by RF magnetron sputtering *Japanese Journal of Applied Physics* **47** 8909

[3.21] Shibata K, Suenaga K, Watanabe K, Horikiri F, Nomoto A and Mishima T 2011 Improvement of Piezoelectric Properties of (K,Na)NbO_3 Films Deposited by Sputtering *Japanese Journal of Applied Physics* **50**

[3.22] Kim B Y, Seong T G, Seo I T, Jang M S, Nahm S, Kang J Y and Yoon S J 2012 Effects of annealing atmosphere on the structural and electrical properties of $(Na_{0.5}K_{0.5})NbO_3$ thin films grown by RF magnetron sputtering *Acta Mater.* **60** 3107-12

[3.23] Wang X, Helmersson U, Olafsson S, Rudner S, Wernlund L D and Gevorgian S 1998 Growth and field dependent dielectric properties of epitaxial $Na_{0.5}K_{0.5}NbO_3$ thin films *Appl. Phys. Lett.* **73** 927-9

[3.24] Kugler V M, Soderlind F, Music D, Helmersson U, Andreasson J and Lindback T 2004 Structure/dielectric property relationship of low temperature synthesised (Na,K)NbO_x thin films *J. Cryst. Growth* **262** 322-6

[3.25] Zaldo C, Gill D S, Eason R W, Mendiola J and Chandler P J 1994 Growth of $KNbO_3$ Thin-Films On MgO By Pulsed-Laser Deposition *Appl. Phys. Lett.* **65** 502-4

[3.26] Nili H, Kandjani A E, Du Plessis J, Bansal V, Kalantar-zadeh K, Sriram S and Bhaskaran M 2013 Alkali ratio control for lead-free piezoelectric thin films utilizing elemental diffusivities in RF plasma *CrystEngComm* **15** 7222-9

[3.27] Pfisterer H and Schubert K 1950 Neue Phasen Vom MNP(B31)-TYP *Z. Metallk.* **41** 358-67

[3.28] Ahtee M and Hewat A W 1975 Structures of $Na_{0.98}K_{0.02}NbO_3$ and $Na_{0.90}K_{0.10}NbO_3$ (Phase-*Q*) at room-temperature by neutron powder diffraction *Acta Crystallogr. Sect. A* **31** 846-50

[3.29] Ahtee M and Hewat A W 1978 Structural phase-transitions in solium-potassium niobate solid-solutions by neutron powder diffraction *Acta Crystallogr. Sect. A* **34** 309-17

[3.30] Zeman M, Fulton C, Lucovsky G, Nemanich R and Yang W-C 2006 Thermal stability of TiO_2, ZrO_2, or HfO_2 on Si (100) by photoelectron emission microscopy *Journal of applied physics* **99** 023519--6

[3.31] Pesty F, Steinrück H-P and Madey T E 1995 Thermal stability of Pt films on TiO_2 (110): evidence for encapsulation *Surface science* **339** 83-95

[3.32] Bhaskaran M, Sriram S, Ruffell S and Mitchell A 2011 Nanoscale Characterization of Energy Generation from Piezoelectric Thin Films *Advanced Functional Materials* **21** 2251-7

[3.33] Castaldi L, Gibbs M R J and Davies H A 2003 Deposition of hard magnetic rare-earth–Fe–B thin films by magnetron sputtering *Journal of applied Physics* **93** 9165-9

[3.34] Rossnegal S M, Yang I and Cuomo J J 1991 Compositional changes during magnetron sputtering of alloys *Thin Solid Films* **199** 59-69

[3.35] Sriram S, Bhaskaran M, Plessis J d, Short K T, Sivan V P and Holland A S 2009 Influence of oxygen partial pressure on the composition and orientation of strontium-doped lead zirconate titanate thin films *Micron* **40** 104-8

[3.36] Thornton J A 1977 High Rate Thick Film Growth *Annual review of materials science* **7** 239-60

[3.37] Thornton J A 1974 Influence of apparatus geometry and deposition conditions on the structure and topography of thick sputtered coatings *Journal of Vacuum Science and Technology* **11** 666-70

[3.38] Shirley D A 1972 High-resolution X-ray photoemission spectrum of the valence bands of gold *Physical Review B* **5** 4709

[3.39] Bansal V, Syed A, Bhargava S K, Ahmad A and Sastry M 2007 Zirconia enrichment in zircon sand by selective fungus-mediated bioleaching of silica *Langmuir* **23** 4993-8

[3.40] Jung K, Kim Y, Park Y S, Jung W, Choi J, Park B, Kim H, Kim W, Hong J and Im H 2011 Unipolar resistive switching in insulating niobium oxide film and probing electroforming induced metallic components *Journal of Applied Physics* **109** 054511-4

[3.41] Magnussen N, Quinones L, Dufner D C, Cocke D L, Schweikert E A, Patnaik B K, Leite C V B and Baptista G B 1989 Analysis of anodic oxide films on niobium *Chemistry of Materials* **1** 220-5

[3.42] Kundu S, Wang Y, Xia W and Muhler M 2008 Thermal sta-bility and reducibility of oxygen-containing functional groups on multiwalled carbon nanotube surfaces: A quantitative high-resolution XPS and TPD/TPR study *The Journal of Physical Chemistry C* **112** 16869-78

[3.43] Sriram S, Bhaskaran M, Mitchell A, Mitchell D and Kostovski G 2008 Nanocolumnar Preferentially Oriented PSZT Thin Films Deposited on Thermally Grown Silicon Dioxide *Nanoscale Res. Lett.* **4** 29-33

[3.44] Merkle R and Maier J 2008 How is oxygen incorporated into oxides? A comprehensive kinetic study of a simple solid-state reaction with $SrTiO_3$ as a model material *Angewandte Chemie (International ed. in English)* **47** 3874-94

[3.45] Rondinelli J M, May S J and Freeland J W 2012 Control of octahedral connectivity in perovskite oxide heterostructures: An emerging route to multifunctional materials discovery *Mrs Bulletin* **37** 261-70

[3.46] Santander-Syro A F, Copie O, Kondo T, Fortuna F, Pailhes S, Weht R, Qiu X G, Bertran F, Nicolaou A, Taleb-Ibrahimi A, Le Fevre P, Herranz G, Bibes M, Reyren N, Apertet Y, Lecoeur P, Barthelemy A and Rozenberg M J 2011 Two-dimensional electron gas with universal subbands at the surface of SrTiO3 *Nature* **469** 189-93

[3.47] Walia S, Balendhran S, Nili H, Zhuiykov S, Rosengarten G, Wang Q H, Bhaskaran M, Sriram S, Strano M S and Kalantar-zadeh K 2013 Transition metal oxides–Thermoelectric properties *Progress in Materials Science* **58** 1443-89

[3.48] Zubko P, Catalan G, Buckley A, Welche P R L and Scott J F 2007 Strain-gradient-induced polarization in $SrTiO_3$ single crystals *Phys. Rev. Lett.* **99** 4

[3.49] Dittmann R, Muenstermann R, Krug I, Park D, Menke T, Mayer J, Besmehn A, Kronast F, Schneider C M and Waser R 2012 Scaling Potential of Local Redox Processes in Memristive $SrTiO_3$ Thin-Film Devices *Proc. IEEE* **100** 1979-90

[3.50] Hou J, Nonnenmann S S, Qin W and Bonnell D A 2014 Size Dependence of Resistive Switching at Nanoscale Metal-Oxide Interfaces *Advanced Functional Materials* n/a-n/a

[3.51] Menzel S, Waters M, Marchewka A, Bottger U, Dittmann R and Waser R 2011 Origin of the Ultra-nonlinear Switching Kinetics in Oxide-Based Resistive Switches *Advanced Functional Materials* **21** 4487-92

[3.52] Muenstermann R, Menke T, Dittmann R and Waser R 2010 Coexistence of Filamentary and Homogeneous Resistive Switching in Fe-Doped $SrTiO_3$ Thin-Film Memristive Devices *Adv. Mater.* **22** 4819-22

[3.53] Sawa A 2008 Resistive switching in transition metal oxides *Mater. Today* **11** 28-36

[3.54] Szot K, Speier W, Bihlmayer G and Waser R 2006 Switching the electrical resistance of individual dislocations in single-crystalline $SrTiO_3$ *Nat. Mater.* **5** 312-20

[3.55] Waser R and Aono M 2007 Nanoionics-based resistive switching memories *Nat. Mater.* **6** 833-40

[3.56] Waser R, Dittmann R, Staikov G and Szot K 2009 Redox-Based Resistive Switching Memories - Nanoionic Mechanisms, Prospects, and Challenges *Adv. Mater.* **21** 2632-63

[3.57] Nili H, Walia S, Balendhran S, Strukov D B, Bhaskaran M and Sriram S 2014 Nanoscale Resistive Switching in Amorphous Perovskite Oxide (*a*-$SrTiO_3$) Memristors *Advanced Functional Materials*

[3.58] Wöhlecke M, Marrello V and Onton A 1977 Refractive index of $BaTiO_3$ and $SrTiO_3$ films *Journal of Applied Physics* **48** 1748-50

[3.59] Nam S H and Kim H G 1992 The effect of heat treatment on the $SrTiO_3$ thin films prepared by radio frequency magnetron sputtering *Journal of Applied Physics* **72** 2895-9

[3.60] Morii K, Kawano H, Fujii I, Matsui T and Nakayama Y 1995 Dielectric relaxation in amorphous thin films of $SrTiO_3$ at elevated temperatures *Journal of applied physics* **78** 1914-9

Chapter 4

[4.1] Strukov D B and Kohlstedt H 2012 Resistive switching phenomena in thin films: Materials, devices, and applications *Mrs Bulletin* **37** 108-17

[4.2] Yang J J S, Strukov D B and Stewart D R 2013 Memristive devices for computing *Nat. Nanotechnol.* **8** 13-24

[4.3] Dittmann R, Muenstermann R, Krug I, Park D, Menke T, Mayer J, Besmehn A, Kronast F, Schneider C M and Waser R 2012 Scaling Potential of Local Redox Processes in Memristive $SrTiO_3$ Thin-Film Devices *Proc. IEEE* **100** 1979-90

[4.4] Muenstermann R, Menke T, Dittmann R and Waser R 2010 Coexistence of Filamentary and Homogeneous Resistive Switching in Fe-Doped $SrTiO_3$ Thin-Film Memristive Devices *Adv. Mater.* **22** 4819-22

[4.5] Sawa A 2008 Resistive switching in transition metal oxides *Mater. Today* **11** 28-36

[4.6] Strukov D B, Snider G S, Stewart D R and Williams R S 2008 The missing memristor found *Nature* **453** 80-3

[4.7] Waser R and Aono M 2007 Nanoionics-based resistive switching memories *Nat. Mater.* **6** 833-40

[4.8] Waser R, Dittmann R, Staikov G and Szot K 2009 Redox-Based Resistive Switching Memories - Nanoionic Mechanisms, Prospects, and Challenges *Adv. Mater.* **21** 2632-63

[4.9] Mannhart J and Schlom D 2010 Oxide interfaces—an opportunity for electronics *Science* **327** 1607-11

[4.10] Rondinelli J M, May S J and Freeland J W 2012 Control of octahedral connectivity in perovskite oxide heterostructures: An emerging route to multifunctional materials discovery *MRS Bulletin* **37** 261-70

[4.11] Yang J J, Inoue I H, Mikolajick T and Hwang C S 2012 Metal oxide memories based on thermochemical and valence change mechanisms *MRS Bulletin* **37** 131-7

[4.12] Yang Z, Ko C and Ramanathan S 2011 Oxide electronics utilizing ultrafast metal-insulator transitions *Annual Review of Materials Research* **41** 337-67

[4.13] Nili H, Walia S, Balendhran S, Strukov D B, Bhaskaran M and Sriram S 2014 Nanoscale Resistive Switching in Amorphous Perovskite Oxide (a-$SrTiO_3$) Memristors *Advanced Functional Materials*

[4.14] Szot K, Speier W, Bihlmayer G and Waser R 2006 Switching the electrical resistance of individual dislocations in single-crystalline $SrTiO_3$ *Nat. Mater.* **5** 312-20

[4.15] Herranz G, Basletic M, Copie O, Bibes M, Khodan A N, Carretero C, Tafra E, Jacquet E, Bouzehouane K, Hamzic A and Barthelemy A 2009 Controlling high-mobility conduction in $SrTiO_3$ by oxide thin film deposition *Appl. Phys. Lett.* **94** 3

[4.16] Menke T, Meuffels P, Dittmann R, Szot K and Waser R 2009 Separation of bulk and interface contributions to electroforming and resistive

switching behavior of epitaxial Fe-doped $SrTiO_3$ *Journal of Applied Physics* **105** 3

[4.17] Kohlstedt H, Petraru A, Szot K, Rudiger A, Meuffels P, Haselier H, Waser R and Nagarajan V 2008 Method to distinguish ferroelectric from nonferroelectric origin in case of resistive switching in ferroelectric capacitors *Appl. Phys. Lett.* **92** 62907

[4.18] Yang J J, Pickett M D, Li X M, Ohlberg D A A, Stewart D R and Williams R S 2008 Memristive switching mechanism for metal/oxide/metal nanodevices *Nat. Nanotechnol.* **3** 429-33

[4.19] Yang J J, Miao F, Pickett M D, Ohlberg D A A, Stewart D R, Lau C N and Williams R S 2009 The mechanism of electroforming of metal oxide memristive switches *Nanotechnology* **20** 9

[4.20] Rodenbucher C, Speier W, Bihlmayer G, Breuer U, Waser R and Szot K 2013 Cluster-like resistive switching of $SrTiO_3$: Nb surface layers *New J. Phys.* **15** 14

[4.21] Shibuya K, Dittmann R, Mi S B and Waser R 2010 Impact of Defect Distribution on Resistive Switching Characteristics of Sr_2TiO_4 Thin Films *Adv. Mater.* **22** 411-4

[4.22] Stille S, Lenser C, Dittmann R, Koehl A, Krug I, Muenstermann R, Perlich J, Schneider C M, Klemradt U and Waser R 2012 Detection of filament formation in forming-free resistive switching $SrTiO_3$ devices with Ti top electrodes *Appl. Phys. Lett.* **100** 4

[4.23] Gutruf P, Shah C M, Walia S, Nili H, Zoolfakar A S, Karnutsch C, Kalantar-zadeh K, Sriram S and Bhaskaran M 2013 Transparent functional oxide stretchable electronics: micro-tectonics enabled high strain electrodes *NPG Asia Mater.* **5** 7

[4.24] Kwon D H, Kim K M, Jang J H, Jeon J M, Lee M H, Kim G H, Li X S, Park G S, Lee B, Han S, Kim M and Hwang C S 2010 Atomic structure of conducting nanofilaments in TiO_2 resistive switching memory *Nat. Nanotechnol.* **5** 148-53

[4.25] Miao F, Strachan J P, Yang J J, Zhang M X, Goldfarb I, Torrezan A C, Eschbach P, Kelley R D, Medeiros-Ribeiro G and Williams R S 2011 Anatomy of a Nanoscale Conduction Channel Reveals the Mechanism of a High-Performance Memristor *Adv. Mater.* **23** 5633-40

[4.26] Munstermann R, Yang J J, Strachan J P, Medeiros-Ribeiro G, Dittmann R and Waser R 2010 Morphological and electrical changes in TiO_2 memristive devices induced by electroforming and switching *Phys. Status Solidi-Rapid Res. Lett.* **4** 16-8

[4.27] Lenser C, Connell Z, Kovács A, Dunin-Borkowski R, Köhl A, Waser R and Dittmann R 2013 Identification of screw dislocations as fast-forming sites in Fe-doped SrTiO3 *Appl. Phys. Lett.* **102** 183504

[4.28] Lenser C, Kuzmin A, Purans J, Kalinko A, Waser R and Dittmann R 2012 Probing the oxygen vacancy distribution in resistive switching Fe-$SrTiO_3$ metal-insulator-metal-structures by micro-x ray absorption near-edge structure *Journal of Applied Physics* **111**

[4.29] Strukov D B, Borghetti J L and Williams R S 2009 Coupled Ionic and Electronic Transport Model of Thin-Film Semiconductor Memristive Behavior *Small* **5** 1058-63

[4.30] Alibart F, Zamanidoost E and Strukov D B 2013 Pattern classification by memristive crossbar circuits using ex situ and in situ training *Nat Commun* **4**

[4.31] Bansal V, Syed A, Bhargava S K, Ahmad A and Sastry M 2007 Zirconia enrichment in zircon sand by selective fungus-mediated bioleaching of silica *Langmuir* **23** 4993-8

[4.32] Shirley D A 1972 High-resolution X-ray photoemission spectrum of the valence bands of gold *Physical Review B* **5** 4709

[4.33] Dai S, Lu H, Chen F, Chen Z, Ren Z Y and Ng D H L 2002 In-doped $SrTiO_3$ ceramic thin films *Appl. Phys. Lett.* **80** 3545-7

[4.34] Shibagaki S and Fukushima K 1999 XPS analysis on Nb–$SrTiO_3$ thin films deposited with pulsed laser ablation technique *Journal of the European Ceramic Society* **19** 1423-6

[4.35] van der Heide P A W, Jiang Q D, Kim Y S and Rabalais J W 2001 X-ray photoelectron spectroscopic and ion scattering study of the $SrTiO_3$(001) surface *Surface Science* **473** 59-70

[4.36] Kuznetsov M, Zhuravlev J F and Gubanov V 1992 XPS analysis of adsorption of oxygen molecules on the surface of Ti and TiN_x films in vacuum *Journal of electron spectroscopy and related phenomena* **58** 169-76

[4.37] Sullivan J L, Saied S O and Bertoti I 1991 Effect of ion and neutral sputtering on single crystal TiO_2 *Vacuum* **42** 1203-8

[4.38] Brunen J and Zegenhagen J 1997 Investigation of the $SrTiO_3$(110) surface by means of LEED, scanning tunneling microscopy and Auger spectroscopy *Surface science* **389** 349-65

[4.39] Morii K, Kawano H, Fujii I, Matsui T and Nakayama Y 1995 Dielectric relaxation in amorphous thin films of SrTiO3 at elevated temperatures *Journal of applied physics* **78** 1914-9

[4.40] Merkle R and Maier J 2008 How is oxygen incorporated into oxides? A comprehensive kinetic study of a simple solid-state reaction with $SrTiO_3$ as a model material *Angewandte Chemie (International ed. in English)* **47** 3874-94

[4.41] Lee K B, Lee K H, Cha J O and Ahn J S 2008 Ti-O Binding States of Resistive Switching TiO_2 Thin Films Prepared by Reactive Magnetron Sputtering *Journal of the Korean Physical Society* **53** 1996-2001

[4.42] Nili H, Kandjani A E, Du Plessis J, Bansal V, Kalantar-zadeh K, Sriram S and Bhaskaran M 2013 Alkali ratio control for lead-free piezoelectric thin films utilizing elemental diffusivities in RF plasma *CrystEngComm* **15** 7222-9

[4.43] Wang Z, Kugler V, Helmersson U, Evangelou E, Konofaos N, Nakao S and Jin P 2002 Characteristics of $SrTiO_3$ thin films deposited on Si by rf magnetron sputtering at various substrate temperatures *Philosophical Magazine B* **82** 891-903

[4.44] Russell B C and Castell M R 2008 Reconstructions on the polar $SrTiO_3$ (110) surface: Analysis using STM, LEED, and AES *Physical Review B* **77** 245414

[4.45] Kundu S, Wang Y, Xia W and Muhler M 2008 Thermal stability and reducibility of oxygen-containing functional groups on multiwalled carbon nanotube surfaces: A quantitative high-resolution XPS and TPD/TPR study *The Journal of Physical Chemistry C* **112** 16869-78

[4.46] Jung K, Kim Y, Park Y S, Jung W, Choi J, Park B, Kim H, Kim W, Hong J and Im H 2011 Unipolar resistive switching in insulating niobium oxide film and probing electroforming induced metallic components *Journal of Applied Physics* **109** 054511-4

[4.47] Strukov D and Williams R S 2009 Exponential ionic drift: fast switching and low volatility of thin-film memristors *Appl Phys A* **94** 515-9

[4.48] Bhaskaran M, Sriram S, Ruffell S and Mitchell A 2011 Nanoscale Characterization of Energy Generation from Piezoelectric Thin Films *Advanced Functional Materials* **21** 2251-7

[4.49] Nili H, Cheng G, Venkatesh T, Sriram S and Bhaskaran M 2013 Correlation between nanomechanical and piezoelectric properties of thin films: An experimental and finite element study *Mater. Lett.* **90** 148-51

[4.50] Nili H, Kalantar-zadeh K, Bhaskaran M and Sriram S 2013 *In situ* nanoindentation: Probing nanoscale multifunctionality *Progress in Materials Science* **58** 1-29

[4.51] Minor A M, Asif S A S, Shan Z W, Stach E A, Cyrankowski E, Wyrobek T J and Warren O L 2006 A new view of the onset of plasticity during the nanoindentation of aluminium *Nat. Mater.* **5** 697-702

[4.52] Nowak R, Chrobak D, Nagao S, Vodnick D, Berg M, Tukiainen A and Pessa M 2009 An electric current spike linked to nanoscale plasticity *Nat. Nanotechnol.* **4** 287-91

[4.53] Shkabko A, Aguirre M H, Kumar A, Kim Y, Jesse S, Waser R, Kalinin S V and Weidenkaff A 2013 Surface deformations as a necessary requirement for resistance switching at the surface of $SrTiO_3$:N *Nanotechnology* **24** 9

[4.54] Messerschmitt F, Kubicek M, Schweiger S and Rupp J L 2014 Memristor Kinetics and Diffusion Characteristics for Mixed Anionic-Electronic SrTiO3-δ Bits: The Memristor-Based Cottrell Analysis Connecting Material to Device Performance *Advanced Functional Materials*

[4.55] Deiss E 2002 Spurious potential dependence of diffusion coefficients in Li^+ insertion electrodes measured with PITT *Electrochimica Acta* **47** 4027-34

[4.56] Zhang J, Xiang B, He Q, Seidel J, Zeches R, Yu P, Yang S, Wang C, Chu Y and Martin L 2011 Large field-induced strains in a lead-free piezoelectric material *Nat. Nanotechnol.* **6** 98-102

[4.57] Al-Hamadany R, Goss J P, Briddon P R, Mojarad S A, Al-Hadidi M, O'Neill A G and Rayson M J 2013 Oxygen vacancy migration in compressively strained $SrTiO_3$ *Journal of Applied Physics* **113** 8

[4.58] Al-Hamadany R, Goss J P, Briddon P R, Mojarad S A, O'Neill A G and Rayson M J 2013 Impact of tensile strain on the oxygen vacancy migration in $SrTiO_3$: Density functional theory calculations *Journal of Applied Physics* **113** 8

[4.59] Dietz G W, Antpohler W, Klee M and Waser R 1995 Electrode infulence on the charge-transport through $SrTiO_3$ thin-films *Journal of Applied Physics* **78** 6113-21

[4.60] Joshi P C and Krupanidhi S B 1993 Structural and electrical characteristics of $SrTiO_3$ thin-films for dynamic random-access memory applications *Journal of Applied Physics* **73** 7627-34

Chapter 5

[5.1] Schroeder H, Zhirnov V V, Cavin R K and Waser R 2010 Voltage-time dilemma of pure electronic mechanisms in resistive switching memory cells *Journal of Applied Physics* **107** 8

[5.2] Kim Y, Kelly S J, Morozovska A, Rahani E K, Strelcov E, Eliseev E, Jesse S, Biegalski M D, Balke N, Benedek N, Strukov D, Aarts J, Hwang

I, Oh S, Choi J S, Choi T, Park B H, Shenoy V B, Maksymovych P and Kalinin S V 2013 Mechanical Control of Electroresistive Switching *Nano Lett.* **13** 4068-74

[5.3] Rondinelli J M, May S J and Freeland J W 2012 Control of octahedral connectivity in perovskite oxide heterostructures: An emerging route to multifunctional materials discovery *MRS Bulletin* **37** 261-70

[5.4] Kim Y, Morozovska A N, Kumar A, Jesse S, Eliseev E A, Alibart F, Strukov D and Kalinin S V 2012 Ionically-Mediated Electromechanical Hysteresis in Transition Metal Oxides *ACS Nano* **6** 7026-33

[5.5] Nguyen T D, Mao S, Yeh Y W, Purohit P K and McAlpine M C 2013 Nanoscale Flexoelectricity *Adv. Mater.* **25** 946-74

[5.6] Zubko P, Catalan G, Buckley A, Welche P R L and Scott J F 2007 Strain-gradient-induced polarization in $SrTiO_3$ single crystals *Phys. Rev. Lett.* **99** 4

[5.7] Pertsev N A, Tagantsev A K and Setter N 2000 Phase transitions and strain-induced ferroelectricity in $SrTiO_3$ epitaxial thin films *Physical Review B* **61** R825-R9

[5.8] Haeni J H, Irvin P, Chang W, Uecker R, Reiche P, Li Y L, Choudhury S, Tian W, Hawley M E, Craigo B, Tagantsev A K, Pan X Q, Streiffer S K, Chen L Q, Kirchoefer S W, Levy J and Schlom D G 2004 Room-temperature ferroelectricity in strained $SrTiO_3$ *Nature* **430** 758-61

[5.9] Jang H W, Kumar A, Denev S, Biegalski M D, Maksymovych P, Bark C W, Nelson C T, Folkman C M, Baek S H, Balke N, Brooks C M, Tenne D A, Schlom D G, Chen L Q, Pan X Q, Kalinin S V, Gopalan V and Eom C B 2010 Ferroelectricity in Strain-Free $SrTiO_3$ Thin Films *Phys. Rev. Lett.* **104** 4

[5.10] Al-Hamadany R, Goss J P, Briddon P R, Mojarad S A, Al-Hadidi M, O'Neill A G and Rayson M J 2013 Oxygen vacancy migration in compressively strained $SrTiO_3$ *Journal of Applied Physics* **113** 8

[5.11] Al-Hamadany R, Goss J P, Briddon P R, Mojarad S A, O'Neill A G and Rayson M J 2013 Impact of tensile strain on the oxygen vacancy migration in $SrTiO_3$: Density functional theory calculations *Journal of Applied Physics* **113** 8

[5.12] Bhaskaran M, Sriram S, Ruffell S and Mitchell A 2011 Nanoscale Characterization of Energy Generation from Piezoelectric Thin Films *Advanced Functional Materials* **21** 2251-7

[5.13] Nili H, Cheng G, Venkatesh T, Sriram S and Bhaskaran M 2013 Correlation between nanomechanical and piezoelectric properties of thin films: An experimental and finite element study *Mater. Lett.* **90** 148-51

[5.14] Nili H, Kalantar-zadeh K, Bhaskaran M and Sriram S 2013 *In situ* nanoindentation: Probing nanoscale multifunctionality *Progress in Materials Science* **58** 1-29

[5.15] Nguyen H H, Wei P J and Lin J F 2011 Electric contact resistance for monitoring nanoindentation-induced delamination *Advances in Natural Sciences: Nanoscience and Nanotechnology* **2** 015007

[5.16] Rar A, Pharr G, Oliver W, Karapetian E and Kalinin S V 2006 Piezoelectric nanoindentation *J. Mater. Res.* **21** 552-6

[5.17] Mylvaganam K, Zhang L, Eyben P, Mody J and Vandervorst W 2009 Evolution of metastable phases in silicon during nanoindentation: mechanism analysis and experimental verification *Nanotechnology* **20** 305705

[5.18] Nowak R, Chrobak D, Nagao S, Vodnick D, Berg M, Tukiainen A and Pessa M 2009 An electric current spike linked to nanoscale plasticity *Nat. Nanotechnol.* **4** 287-91

[5.19] Zhang J, Xiang B, He Q, Seidel J, Zeches R, Yu P, Yang S, Wang C, Chu Y and Martin L 2011 Large field-induced strains in a lead-free piezoelectric material *Nat. Nanotechnol.* **6** 98-102

[5.20] Johnson K L and Johnson K L 1987 *Contact mechanics*: Cambridge university press)

[5.21] Braunovic M, Myshkin N K and Konchits V V 2010 *Electrical contacts: fundamentals, applications and technology*: CRC press)

[5.22] Wexler G 1966 The size effect and the non-local Boltzmann transport equation in orifice and disk geometry *Proceedings of the Physical Society* **89** 927

[5.23] Fischer-Cripps A C 2011 *Nanoindentation* vol 1: Springer)

[5.24] Holm R and Holm E 1967 *Electric contacts: theory and application*: Springer-Verlag New York, NY)

[5.25] Schmid U and Seidel H 2008 Effect of high temperature annealing on the electrical performance of titanium/platinum thin films *Thin Solid Films* **516** 898-906

[5.26] Timsit R S 1999 Electrical contact resistance: properties of stationary interfaces *Components and Packaging Technologies, IEEE Transactions on* **22** 85-98

[5.27] Minor A M, Asif S A S, Shan Z W, Stach E A, Cyrankowski E, Wyrobek T J and Warren O L 2006 A new view of the onset of plasticity during the nanoindentation of aluminium *Nat. Mater.* **5** 697-702

[5.28] Yang J J, Miao F, Pickett M D, Ohlberg D A A, Stewart D R, Lau C N and Williams R S 2009 The mechanism of electroforming of metal oxide memristive switches *Nanotechnology* **20** 9

[5.29] Kwon D H, Kim K M, Jang J H, Jeon J M, Lee M H, Kim G H, Li X S, Park G S, Lee B, Han S, Kim M and Hwang C S 2010 Atomic structure of conducting nanofilaments in TiO_2 resistive switching memory *Nat. Nanotechnol.* **5** 148-53

[5.30] Munstermann R, Yang J J, Strachan J P, Medeiros-Ribeiro G, Dittmann R and Waser R 2010 Morphological and electrical changes in TiO_2 memristive devices induced by electroforming and switching *Phys. Status Solidi-Rapid Res. Lett.* **4** 16-8

[5.31] Miao F, Strachan J P, Yang J J, Zhang M X, Goldfarb I, Torrezan A C, Eschbach P, Kelley R D, Medeiros-Ribeiro G and Williams R S 2011 Anatomy of a Nanoscale Conduction Channel Reveals the Mechanism of a High-Performance Memristor *Adv. Mater.* **23** 5633-40

[5.32] Dittmann R, Muenstermann R, Krug I, Park D, Menke T, Mayer J, Besmehn A, Kronast F, Schneider C M and Waser R 2012 Scaling Potential of Local Redox Processes in Memristive $SrTiO_3$ Thin-Film Devices *Proc. IEEE* **100** 1979-90

[5.33] Muenstermann R, Menke T, Dittmann R and Waser R 2010 Coexistence of Filamentary and Homogeneous Resistive Switching in Fe-Doped $SrTiO_3$ Thin-Film Memristive Devices *Adv. Mater.* **22** 4819-22

[5.34] Rodenbucher C, Speier W, Bihlmayer G, Breuer U, Waser R and Szot K 2013 Cluster-like resistive switching of $SrTiO_3$: Nb surface layers *New J. Phys.* **15** 14

[5.35] Szot K, Speier W, Bihlmayer G and Waser R 2006 Switching the electrical resistance of individual dislocations in single-crystalline $SrTiO_3$ *Nat. Mater.* **5** 312-20

[5.36] Shkabko A, Aguirre M H, Kumar A, Kim Y, Jesse S, Waser R, Kalinin S V and Weidenkaff A 2013 Surface deformations as a necessary requirement for resistance switching at the surface of $SrTiO_3$:N *Nanotechnology* **24** 9

[5.37] Messerschmitt F, Kubicek M, Schweiger S and Rupp J L 2014 Memristor Kinetics and Diffusion Characteristics for Mixed Anionic-Electronic $SrTiO_{3-\delta}$ Bits: The Memristor-Based Cottrell Analysis Connecting Material to Device Performance *Advanced Functional Materials*

[5.38] Deiss E 2002 Spurious potential dependence of diffusion coefficients in Li^+ insertion electrodes measured with PITT *Electrochimica Acta* **47** 4027-34

[5.39] Dietz G W, Antpohler W, Klee M and Waser R 1995 Electrode infulence on the charge-transport through $SrTiO_3$ thin-films *Journal of Applied Physics* **78** 6113-21

[5.40] Joshi P C and Krupanidhi S B 1993 Structural and electrical characteristics of $SrTiO_3$ thin-films for dynamic random-access memory applications *Journal of Applied Physics* **73** 7627-34

Appendix B

[B.1] Nili H, Kalantar-zadeh K, Bhaskaran M and Sriram S 2013 *In situ* nanoindentation: Probing nanoscale multifunctionality *Progress in Materials Science* **58** 1-29

[B.2] Giannakopoulos A E and Suresh S 1999 Theory of indentation of piezoelectric materials *Acta Materialia* **47** 2153-64

[B.3] Zhang J X, XiangB, HeQ, SeidelJ, Zeches R J, YuP, Yang S Y, Wang C H, Chu Y H, Martin L W, Minor A M and RameshR 2011 Large field-induced strains in a lead-free piezoelectric material *Nat Nano* **6** 98-102

[B.4] Rar A, Pharr G M, Oliver W C, Karapetian E and Kalinin S V 2006 Piezoelectric nanoindentation *Journal of Materials Research* **21** 552-6

[B.5] Bhaskaran M, Sriram S, Ruffell S and Mitchell A 2011 Nanoscale characterization of energy generation from piezoelectric thin films *Advanced Functional Materials* **21** 2251-7

[B.6] Nowak R, Chrobak D, Nagao S, Vodnick D, Berg M, Tukiainen A and Pessa M 2009 An electric current spike linked to nanoscale plasticity *Nat Nano* **4** 287-91

[B.7] Nili H, Cheng G, Venkatesh T, Sriram S and Bhaskaran M 2013 Correlation between nanomechanical and piezoelectric properties of thin films: An experimental and finite element study *Mater. Lett.* **90** 148-51

[B.8] Nili H, Walia S, Balendhran S, Strukov D B, Bhaskaran M and Sriram S 2014 Nanoscale Resistive Switching in Amorphous Perovskite Oxide (a-SrTiO3) Memristors *Advanced Functional Materials*

[B.9] Romasco A, Friedman L, Fang L, Meirom R, Clark T, Polcawich R, Pulskamp J, Dubey M and Muhlstein C 2010 Deformation behavior of nanograined platinum films *Thin Solid Films* **518** 3866-74

[B.10] Hyun S, Kraft O and Vinci R P 2004 Mechanical behavior of Pt and Pt–Ru solid solution alloy thin films *Acta Mater.* **52** 4199-211

[B.11] Swain M and Menčik J 1994 Mechanical property characterization of thin films using spherical tipped indenters *Thin Solid Films* **253** 204-11

[B.12] Lee H, Coutu R A, Mall S and Leedy K D 2006 Characterization of metal and metal alloy films as contact materials in MEMS switches *Journal of micromechanics and microengineering* **16** 557

[B.13] Khrushchov M and Berkovich E 1951 Methods of determining the hardness of very hard materials: the hardness of diamond *Industrial diamond review* **11** 42-9

[B.14] Nili H, Kandjani A E, Du Plessis J, Bansal V, Kalantar-zadeh K, Sriram S and Bhaskaran M 2013 Alkali ratio control for lead-free piezoelectric thin films utilizing elemental diffusivities in RF plasma *CrystEngComm* **15** 7222-9

[B.15] Fischer-Cripps A C 2011 *Nanoindentation* vol 1: Springer)

[B.16] Oliver W C and Pharr G M 1992 An improved technique for determining hardness and elastic modulus using load and displacement sensing indentation experiments *J. Mater. Res.* **7** 1564-83

[B.17] Oliver W C and Pharr G M 2004 Measurement of hardness and elastic modulus by instrumented indentation: Advances in understanding and refinements to methodology *J. Mater. Res.* **19** 3-20

[B.18] Vlassak J J and Nix W D 1993 Indentation modulus of elastically anisotropic half spaces *Philosophical Magazine A* **67** 1045-56

[B.19] Bhushan B and Li X 2003 Nanomechanical characterisation of solid surfaces and thin films *International Materials Reviews* **48** 125

[B.20] Archard J 1953 Contact and rubbing of flat surfaces *Journal of applied physics* **24** 981-8

[B.21] Vancea J, Hoffmann H and Kastner K 1984 Mean free path and effective density of conduction electrons in polycrystalline metal films *Thin Solid Films* **121** 201-16

[B.22] Hoffmann H, Vancea J and Jacob U 1985 Surface scattering of electrons in metals *Thin Solid Films* **129** 181-93

[B.23] Munoz R C, Finger R, Arenas C, Kremer G and Moraga L 2002 Surface-induced resistivity of thin metallic films bounded by a rough fractal surface *Physical Review B* **66** 205401

[B.24] Munoz R C 2005 Resistivity induced by a rough surface of thin gold films deposited on mica *Journal of Molecular Catalysis A: Chemical* **228** 163-75

[B.25] Zhang W, Brongersma S H, Richard O, Brijs B, Palmans R, Froyen L and Maex K 2004 Influence of the electron mean free path on the resistivity of thin metal films *Microelectronic Engineering* **76** 146-52

APPENDIX A

MATERIALS AND METHODS

A.1. PVD Synthesis and Post-Synthesis Treatments

A.1.1. Magnetron sputtering

All RF magnetron sputtering and RF/DC magnetron co-sputtering of co-doped of perovskite oxide thin films were carried out using a Kurt Lesker PVD 75 PVD Magnetron Sputtering deposition system with DC and . The system has two sputtering power sources, a DC source for the deposition of metallic species and a RF source for the deposition of oxide species from ceramic targets. The deposition orientation is sputter up with a target to substrate distance of 50 cm. A substrate rotation speed of 20 rpm was used to ensure optimal coverage uniformity. For all oxide deposition runs the vacuum chamber was pumped down overnight to reach a base pressure of $< 4 \times 10^{-7}$ Torr. The substrate temperature during the deposition was controlled using a precision Eurotherm controller. These parameters ensure the deposition of monolithic thin films with low sputtering yield which allows for precise control of their thickness and orientation.

A.1.2. Electron beam evaporation

The deposition of all metallic and adhesion layers (Pt, Ti, TiO_2) was carried in a Kurt Lesker PVD 75 electron beam evaporation system using metallic and oxide targets. No substrate heating or rotation was used during these depositions.

A.1.3. Post-annealing treatments

The post annealing treatments were carried out in an MTI vacuum furnace. For vacuum annealing, the furnace was pumped down to a base pressure of $<2\times10^{-6}$ Torr. For annealing in oxygen atmospheres, the furnace was first pumped down to a base pressure of $< 1 \times 10^{-5}$ Torr. Afterward the oxygen was flown into the chamber (10 ppm pressure) using mas flow controlled gauges.

A.2. Materials Characterization

A.2.1. X-Ray diffractometry (XRD)

The crystallography of the thin films was studied by X-ray diffraction (XRD) using a Bruker D4 Endeavour diffractometer with a copper K_α source (with a wavelength of 0.154056 nm). The patterns were collected with a stage rotation of 15 rpm in the 2θ range between 20° and 60° in 0.02° steps, with a collection time of 4 s at each step, in the Bragg-Brentano geometry to account for all possible crystal orientations in the thin films.

A.2.2. X-Ray photoelectron spectroscopy (XPS)

X-ray photoelectron spectroscopy (XPS) surface and depth profile analyses were carried out using a Thermo Scientific K-Alpha instrument with a base vacuum pressure of $< 10^{-8}$ Torr. The surface composition analysis was

performed in the central area of the samples with a 400-100 μm spot size. An aluminum K_α radiation source with energy of 1485 eV was used, with the carbon peaks on the sample surface used as reference for calibration. The composition of the film was determined utilizing the area under the curves, fitted and corrected with sensitivity factors using the Avantage data system.

Depth profiling was performed by successive, repeated argon-ion etch and spectrometry processes. This was performed in consecutive etching steps for 10 s each with a 3 kV source voltage low ion beam intensity. Ion beam raster sizes and etching times were varied from 1 to 2 mm and 5 to 20 s respectively for patterned thin films and of know thickness to establish the etching depth for each thin film composition with the current ion beam intensity. The etching depth was determined *ex situ* using an Ambios XP-2 surface profilometer.

Core-level XPS spectra of distinct elements were background corrected using Shirley algorithm, and distinct chemical species were resolved using a non-linear least square fitting procedure, after aligning the elemental binding energies to adventitious carbon (C1s) binding energy of 285 eV. The fitting procedure involved an estimation of the chemically distinct species based on their reported peak positions and the general shape of the shift-corrected spectrum. Gaussian functions were used to find the best fits for s, d and p orbitals in the vicinity of the estimated peak position with the least square fitting procedure with a targeted fitting goodness measure of > 0.995.

The fitted spectra and calculated atomic concentration for various STO thin films were compared with the reference spectra and concentration data acquired from stoichiometric thin films and single crystal STO samples to

determine the relative change in the concentration and distinct changes in the oxidation states. The relative approach allowed for a tentative assessment and separation of ion beam etching effects on the concentration and oxidation states.

A.2.3. Electrical characterization

The electrical characterization of *a*-STO MIM cells was performed using Agilent 2900A series sourcemeter and pulse generator for two-probe and four-probe direct current and pulse transient measurements. Characterizations were performed using either the bottom or top electrode as the drive electrode with the opposite electrode connected to the system ground.

For voltage sweep measurements, a step trigger time between 10 ms and 100 µs was used and the measurement time constant was varied with accordingly with a minimum of 10 µs. For pulse measurements, pulse widths of 10-100 µs were employed with a fixed measurement time constant of 10 µs. Long duration constant bias measurements were carried out in Source & Sampling mode were a constant bias was held between the two electrodes and current was measured periodically at defined intervals (10 to 100 s).

A.2.4. *In situ* electrical nanoindentation

Nanoindentation experiments with *in situ* electrical measurements were carried out using Hysitron's NanoECR system on a TI 950 Triboindenter. A conductive Pulsar™ Berkovich tip was used, with the nanoindentation technique enabling the *in situ* measurement of electrical contact resistance between the indenter tip and the specimen.

A.2.5. Surface morphology and roughness measurements

The surface morphology and the roughness of thin film samples were measured using two methods.

Atomic Force Microscopy (AFM) scans were performed in the tapping mode with scan sizes of 2×2 µm of 5×5 µm, using a Digital Instruments Dimension 3100 scanning probe microscope with a Nanoscope IIIa controller. Scan rates of 0.5 Hz were used to ensure a high signal to noise ratio. The average roughness of the samples was calculated with Nanoscope analysis software and Gwyddion software package.

In situ Scanning Probe Microscopy (SPM) scan were performed using Hysitron TI950 Triboindenter's *in situ* SPM tool with scan sizes identical to AFM scans. Contact forces in the range of 2 to 0.5 µN and scan rates of 1 to 0.5 Hz were used for all samples. The average roughness of the samples was calculated using Hysitron's Triboscan software and Gwyddion software package.

A.2.6. Depth limited scanning wear

The top electrode of MIM devices were removed through a scanning wear step using Hysitron TI950 Triboindenter's scanning wear tool. 3×3 µm areas of the top electrodes were scanned consecutively in SPM mode with a blunt Berkovich tip (tip radius of ~ 500 nm) and contact forces ranging from 15 to 40 µN. This allowed for the gradual removal of 60 nm Pt/Ti electrode. The wear depth was measured *in situ* after each consecutive scanning pass utilizing *in situ* SPM with 2 µm contact force. The complete removal of the electrode was confirmed by the wear depth as well as *in situ* electrical nanoindentation measurements biasing the top electrode line, to ensure an open circuit inside the wear area.

Considering the metal pile up around the wear region, an effective 2×2 µm area was cleared of the top electrode following the depth limited scanning wear step.

APPENDIX B

NANOSCALE ELECTRO-MECHANICAL DYNAMICS OF NANO-CRYSTALLINE PLATINUM THIN FILMS

Platinum thin films are prevalent as contact electrodes in a variety of MEMS/NEMS applications for devices operating under high temperature, mechanical stress and harsh environments due to their high temperature stability, excellent mechanical properties and high temperature coefficient for resistance. Moreover, platinum thin films are routinely employed as contact electrodes in the high temperature synthesis of complex oxides for emerging oxide electronics applications. As such, it is necessary to understand and accurately quantify the nano-electromechanical properties of these metallic films. Performing nanoindentation (where an ultra-fine hard tip probes mechanical properties) with *in situ* electrical measurements has the capability to provide an unprecedented amount of valuable information [B.1]. The technique has been widely used to investigate nano-electromechanical phenomena in a wide range of complex material systems [B.1-8].

Although there have been a few studies investigating the nanoscale mechanical and electrical characteristics of Pt thin films, they have always reported atypical elastic modulus values [B.9-12]. These studies neglect basic parameters such

as surface roughness of the films that can generate anomalous data. In addition, factors such as substrate effects, film texture, grain morphology and pile-up regions that form as a result of mechanical force need to be considered and their effect eliminated to reveal an error-free depiction of the true characteristics of these thin films. Additionally, a limited number of nanoindentation studies such as the one conducted by Hyun *et al.* [B.10] have been carried out at extremely shallow indent depths (<20 nm) where the surface roughness of the films and abnormalities in indenter's shape have a profound impact.

This Appendix details the use of *in situ* electrical nanoindentation technique using a conductive ceramic Berkovich tip [B.13] to obtain the nano-electromechanical properties of <111> oriented nano-crystalline Pt thin films. The results of this appendix are currently in press for publication in ***Journal of Applied Physics***.

B.1. Experimental Details

Platinum films of 200 nm thickness, with a 20 nm thick TiO_2 adhesion layer, were deposited on thermally oxidized silicon substrates (300 nm SiO_2/Si) using electron beam evaporation at room temperature. The use of 20 nm TiO_2 layer ensures reliable adhesion between the platinum thin film and the underlying substrate which is critical for the reliability of electrical contacts. Furthermore, we have previously reported that the presence of a TiO_2 adhesion layer prevents the structural breakdown of the platinum thin film during the high temperature deposition of perovskite oxides [B.14]. This makes the structure a viable substrate for oxide electronics. Additionally, the presence of an insulating

TiO_2 layer would mean that electrical measurements using *in situ* electrical nanoindentation technique yield the inherent properties of the platinum thin films in the multi-layer structure. As-deposited platinum thin films had an average roughness (R_a) of 0.51 nm and an average grain size of 17.1 nm. As-deposited platinum thin films had an average roughness (R_a) of 0.51 nm and an average grain size of 17.1 nm. The as-deposited thin films were post-annealed in vacuum at 600^0C to acquire nano-crystalline platinum films with a nominal roughness (R_a) of 2.9 nm and average grain size of 29.6 nm, confirmed by atomic force microscopy (Figure B.1).

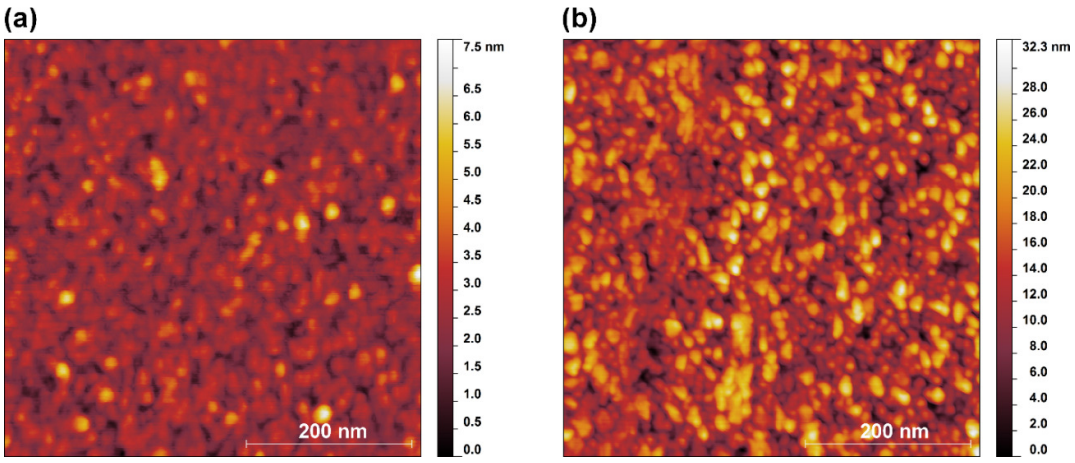

Figure B.1. High resolution AFM scans of **(a)** as-grown and **(b)** nano-crystalline platinum thin films. Post-annealing treatments at 600 ℃ in vacuum were employed to obtain the nano-crystalline films. Post-annealing treatment results in the formation of highly oriented nano-grains with an average diameter of 29.6 nm.

The films were characterized by X-ray diffraction (XRD). Figure B.2 shows the XRD patterns for as-grown and post-annealed Pt/TiO2/SiO2/Si structures. The average resistivity of the nano-crystalline platinum thin films was found to be 16.3 μΩ.cm.

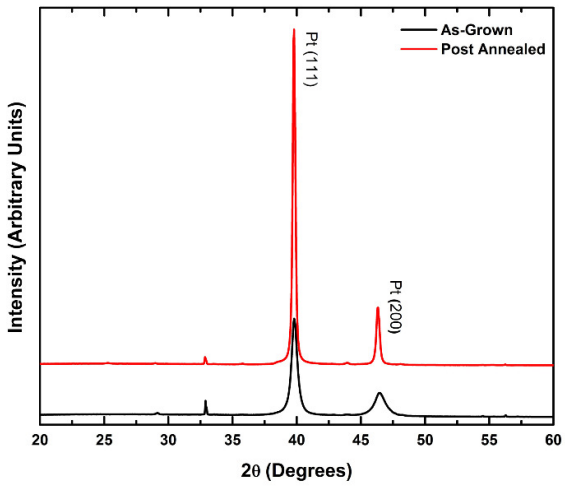

Figure B.2. X-ray diffractograms for as-grown and post-annealed $Pt/TiO_2/SiO_2/Si$ thin films. Post-annealing at 600 ℃ in vacuum results in a strongly <111> oriented nano-crystalline platinum layer.

B.2. Nanomechanical properties of Nano-Crystalline Platinum Thin Film Structure

B.2.1. Quantified evaluation of the mechanical properties of nano-crystalline platinum films

Nanomechanical properties of nano-crystalline platinum thin films were obtained from the nanoindentation experiments. The tip drift rate was negligible (<0.08 nm/s) at varying loading rates (10 to 100 µN/s). The total penetration depths were confined to within 15% of the films' thicknesses [B.15] (load controlled indents with a maximum force of 500 µN). The acquired data was corrected for artefacts such as pile-up heights and machine compliance to obtain an accurate assessment of the inherent nanomechanical properties of the thin films. Using the traditional Oliver-Pharr method [B.16,17] the hardness of the films (H) and the contact plane elastic modulus (E^*) can be calculated as:

$$H = \frac{P_{max}}{A_c} \qquad (1)$$

$$E^* = \frac{1}{2} S \sqrt{\frac{\pi}{A_c}} \qquad (2)$$

where P_{max}, A_c and S are the maximum indentation force, projected contact area and contact stiffness, respectively. Subsequently, the elastic modulus of the thin films (E_f) can be calculated from E^* as:

$$\frac{1}{E^*} = \frac{(1-\nu_i^2)}{E_i} - \frac{(1-\nu_f^2)}{E_f} \qquad (3)$$

where v is the Poisson's ratio, with subscripts *i* and *f* referring to the indenter and the film, respectively.

In the Oliver-Pharr method, an accurate estimation of projected contact area is critical to the accuracy of calculated hardness and elastic modulus. Hence, it is essential to accurately characterize the contact area function of the indenter probe. The relationship between the penetration depth (h_c) and the contact area for an ideal Berkovich indenter (A_c) is given by $A_c = 24.5h_c^2$. In case of a non-ideal probe, the deviations of the contact area profile from the ideal case can be expressed in form of a fitting function as shown below:

$$A_c = C_0 h_c^2 + C_1 h_c + C_2 h_c^{1/2} + C_3 h_c^{1/4} + C_4 h_c^{1/8} + C_5 h_c^{1/16} \qquad (4)$$

where C_n represents the fitting constants calculated based on the measured contact areas on a standard sample of known elastic modulus and hardness (e.g. quartz) in a range of incremental contact depths.

Tip area functions in the form of Equation (4) were calculated using the penetration depth data on a standard fused quartz sample with an elastic modulus of 72.1 GPa. An area function fitted to sufficiently high penetration depths (h_c >100 nm) will provide an accurate estimation of A_c for evaluation of hardness and modulus in a similar penetration depth range. However, for penetration depths outside this designated range, using the same area function leads to an erroneous estimation of the projected contact area due to an often non-uniform profile of the indenter. In particular, the error margin becomes specifically large in the shallow indentation depth regime, where the plastic deformation in the material is minimal, and deviations from an ideal pyramidal shape become more pronounced at the probe's tip. To address this issue, separate tip area functions were fitted to low (3-28.3 nm), moderate (28.3-53.2 nm) and high (53.2-132 nm) penetration depth ranges. Table B.1 includes the fitted constants for area functions in the form of Equation (4) in each penetration depth regime. Area *vs.* depth graphs of these area functions in penetration depths from 3-200 nm are illustrated in Figure B.3. The use of separate area functions for different ranges of penetration depths results in a significant improvement in the accuracy of contact area estimations. Area measurements on the *in situ* SPM images of the residual contact areas on platinum thin films agree very well with the contact areas estimated from the area functions, indicating the accuracy of these functions. The hardness and elastic modulus of nano-crystalline platinum thin films with strong <111> orientations was calculated from load-displacement data at 5×5 indentation arrays at different regions of the thin films using the shallow depth tip area function.

Table B.1. Fitting constants for the area functions in different penetration depth regimes. Calculated from indents with depths on standard fused quartz sample with an average elastic modulus of 72.1 GPa.

	Ideal Berkovich	Shallow Depth	Moderate Depth	Large Depth
C_0	24.5	24.16396	24.5	24.5
C_1	0	927.0421	-252.9766	2273.36
C_2	0	729.377	154481.2	473745.3
C_3	0	0.58313	-1.23457×10^6	-4.75978×10^6
C_4	0	368.8878	2.14228×10^6	5.74874×10^6
C_5	0	0	-964513.8	169.5305

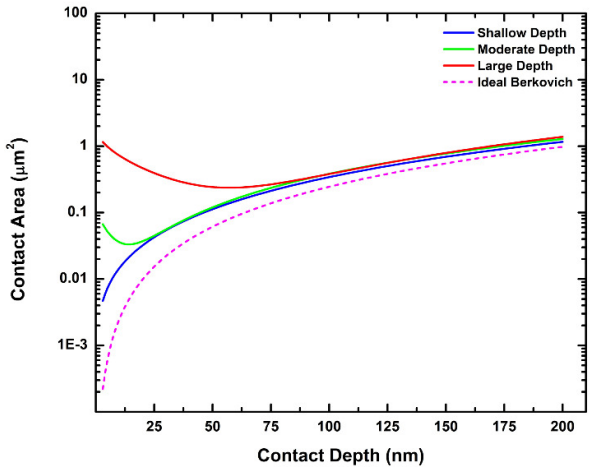

Figure B.3. Contact area *vs.* depth as determined by different tip area functions. Area functions are most accurate in their designated depth range. This is especially true in case of the shallow depth indents where estimations based on moderate and large depth area functions are completely invalid.

The use of the designated tip area function for the shallow depth indentations ensures a greater accuracy in the analysis of the nanoindentation data since it allows correcting for the geometrical non-ideality of the indenter profile which becomes excessively important in the shallow depth regime. A hardness value

of 8.5 GPa (±2.6%) and an elastic modulus of 177 GPa (±1.9%) was obtained for nano-crystalline platinum thin films which is in good agreement with the theoretical values for <111> textured platinum thin films [B.9,18]. Whereas similar hardness values are measured for <111> textured platinum thin films [B.9], the reported measured elastic moduli are usually in the range 150-160 GPa [B.9-11]. This variation is due to the fact that calculations of the plane strain modulus are extremely sensitive to the estimated contact depth and area as described before. An inaccurate estimation of the residual contact area can result in an underestimation of elastic modulus.

B.2.2. Substrate and loading rate effects

Upon further increase of the nanoindentation load, substrate effects on the mechanical response begin to appear where out-of plane stresses due to the structural inhomogeneity are likely to cause pile-up formations. Figure B.4 shows the *P-h* response of the Pt/TiO_2/SiO_2/Si structure under loads of up to 5000 µN.

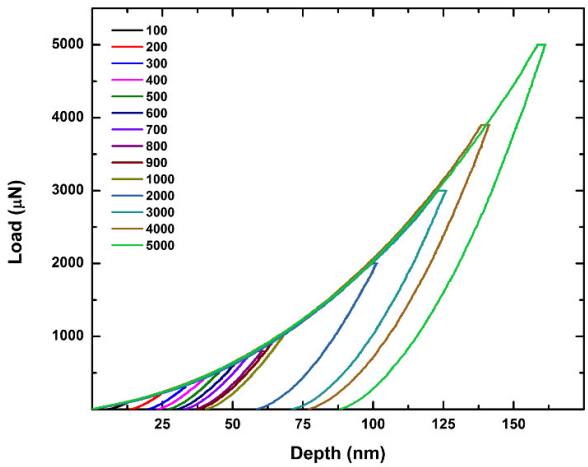

Figure B.4. Load-displacement curves of nano-crystalline platinum thin films in 100-5000 µN load range.

Investigations on the *in situ* SPM images at high-load indent spots reveal noticeable pile-ups around the contact area at loads higher than 1000 µN (Figure B.5), with height only dependent on the maximum load (variations in loading rate did not affect the measured pile-up heights).

The contact depth readings at higher loads include the pile-up height as an added factor which needs to be eliminated to obtain the true indentation depth values [B.19]:

$$h_c = h_{max} - \xi P_{max} S^{-1} - h_{pu} \qquad (5)$$

where h_{pu} corresponds to the pile-up height and ξ is the geometrical factor of the indenter (0.72 in case of Berkovich indenter) [B.19].

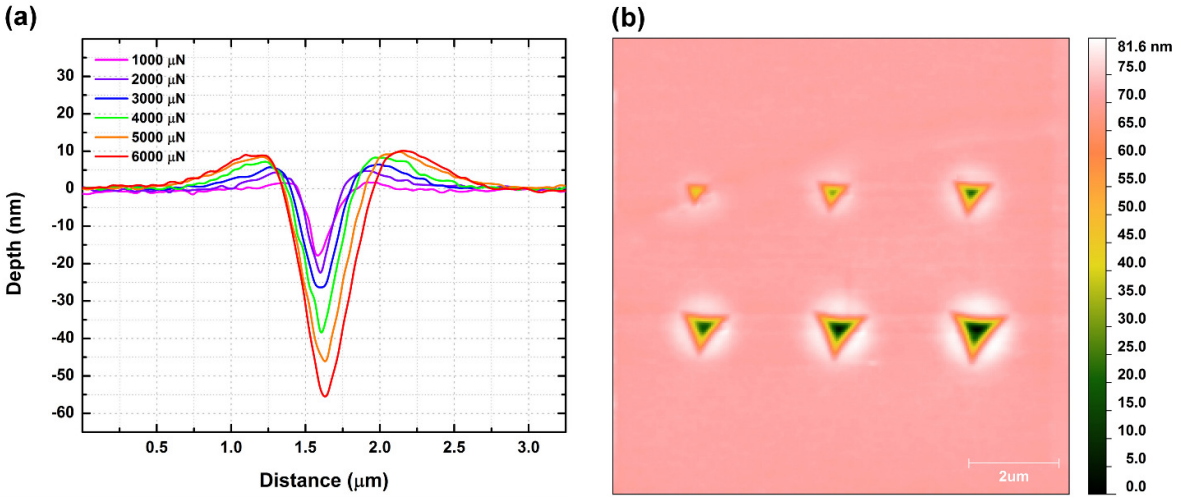

Figure B.5. Pile-up deformations around the nanoindentation contact area in nano-crystalline platinum films. **(a)** 1000-6000 µN contact profiles determined from in situ SPM scans after backgrond corrections. **(b)** High resolution *in situ* SPM scan of the nanoindetnation contacts.

As such, the hardness and elastic modulus values of the structure were evaluated after correcting for the pile-up heights at higher loads. Upon increasing the penetration depths to more than 15% of the film's thickness

(>500 µN loads), the substrate effects become noticeable and both hardness and modulus values begin to drop (Figure B.6). The values eventually settle to an average of 7.76 (±2.1%) GPa and 152.43(± 1.9%) GPa for hardness and elastic modulus at loads higher than 1000 µN. Together with revealing the formation of pile-ups, the results also highlight the effect of substrate on the mechanical behavior of nano-crystalline platinum thin films structure.

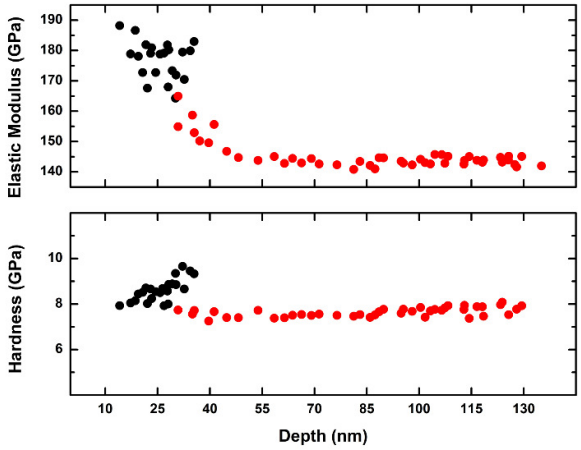

Figure B.6. Mechanical properties of nano-crystalline platinum films subject to increasing indentation load/depth. Black dots denote the nanomechanical response of platinum films (penetration depths <15% of the film thickness). Upon further increase of the indentation load/depth, substrate effects start to appear (red dots).

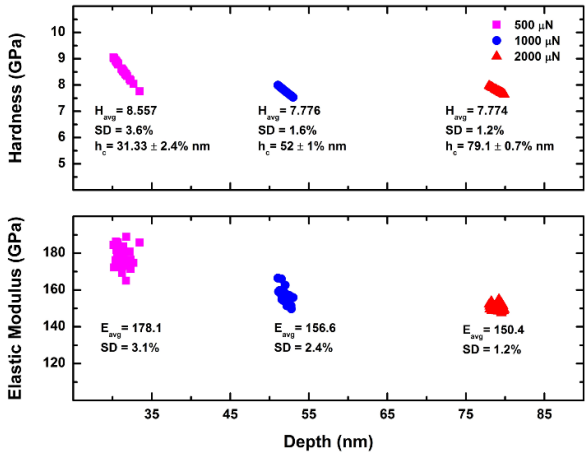

Figure B.7. Mechanical properites of nano-crystalline platinum films at constant indentation loads with variable loading rates for maximum loads of 500, 1000 and 2000 µN.

To verify the accuracy of the results, multiple load-controlled indentation experiments were carried out with constant loads of 500 µN (maximum load to avoid the substrate effect, $h_c \leq 15\%$ film thickness), 2000 and 1000 µN with incremental loading rates (10 to 100 µN/s). Figure B.7 illustrates the mechanical properties calculated for each maximum load along with the standard deviations in each of the calculated parameters. Loading rates appear to have no significant effect on the mechanical response of the structure.

B.3. *In situ* Electrical Nanoindentation

In situ electrical measurements were performed using the loading profile depicted in Figure B.8 to characterize the properties of platinum thin films' nanoscale contacts at different loads and penetration depths. The experiments were carried out at indentation loads ranging from 50 to 5000 µN with constant voltage bias and loading rates.

A constant bias of 1 mV and a loading rate of 10 µN/s were used for loads up to 500 µN. For larger loads the voltage bias and the loading rate were set to 0.5 mV and 100 µN/s, respectively, to minimize the drift value and prevent excessive heating of the nanoscale contact. One second holding periods at the beginning and the end of the loading profile were used to characterize the contact resistance at zero approach and retract points. A long holding segment at maximum load was used to measure the minimum contact resistance at different penetration depths under constant bias as well as with ±1 mV voltage sweeps to evaluate the contact behavior. Figure B.9 show the representative *in situ* current *vs.* depth and contact resistance *vs.* load graphs in low (<500 µN)

and high load (>1000 µN) regimes, respectively, after correcting for the drift rate and displacement offsets.

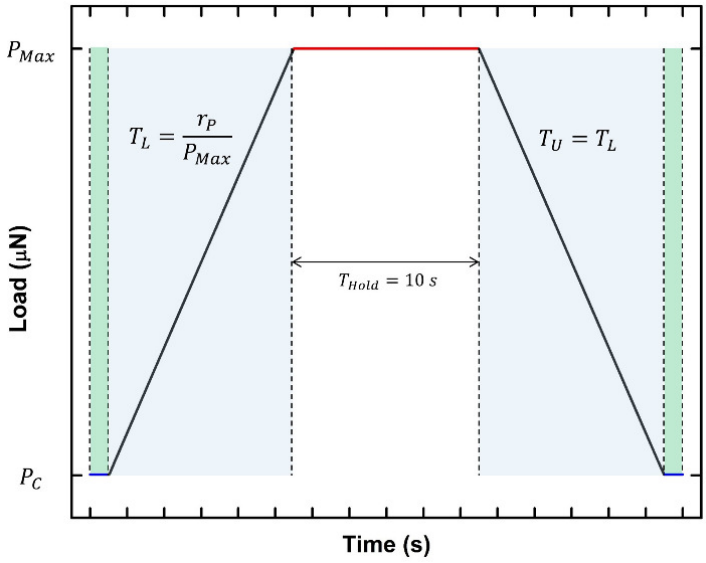

Figure B.8. Load-profile for *in situ* electrical nanoindentation experiments. A constant bias is apped to the platinum at low-load hold and load/unload segments. Sweep experiments are carried out during hold segments at maximum load.

The sweep tests reveal that the contact is ohmic even at indentation loads as low as 50 µN, which confirms the metallic nature of the contact between the indenter and platinum films (Figure B.10). For very small contact areas (maximum contact depth <8 nm and load <50 µN) the contact resistance remains high, possibly due to a higher surface resistivity at the indenter's tip as well as friction, and scattering effects due to the platinum film's roughness [B.20-23] (Figure B.9c, d). After this initial stage, the contact resistance decreases abruptly subject to progressively increasing indentation loads, which can be correlated with the onset of plastic deformation of the platinum films. The discontinuity disappears when the loading rate is increased ten-folds to 100 µN/s for higher peak loads (>1000 µN), as the plastic deformation starts

rapidly, before a full integration cycle (0.5 s) of the current measurement system.

The methodology detailed in Chapter 5, together with depth-specific tip area functions obtained in section B.1 were used to accurately assess the electrical response of nano-crystalline platinum thin films during the *in situ* electrical nanoindentation experiments.

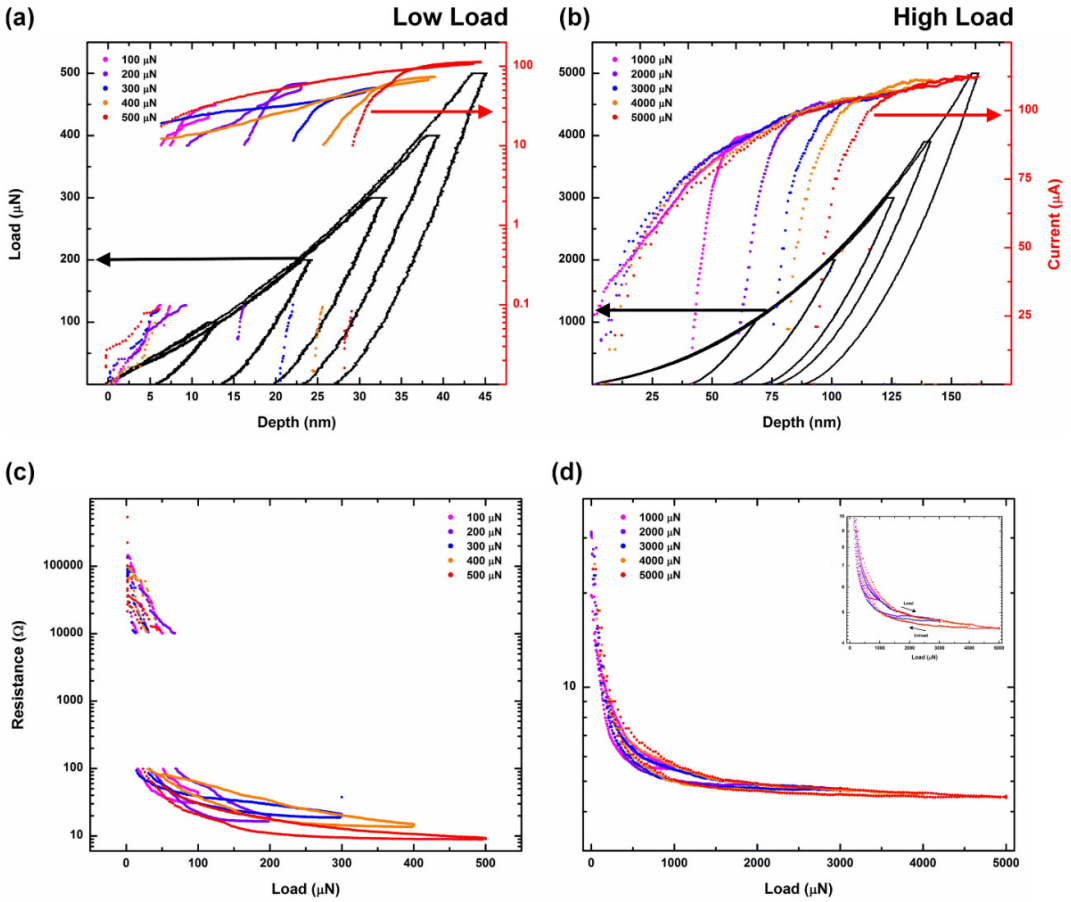

Figure B.9. *In situ* electrical response of nano-crystalline platinum films in low and high load regimes. **(a,b)** *In situ* electrical current at the nano-contact subject to indentation load/depth. **(c,d)** Measured nano-contact resistance *vs.* contact load.

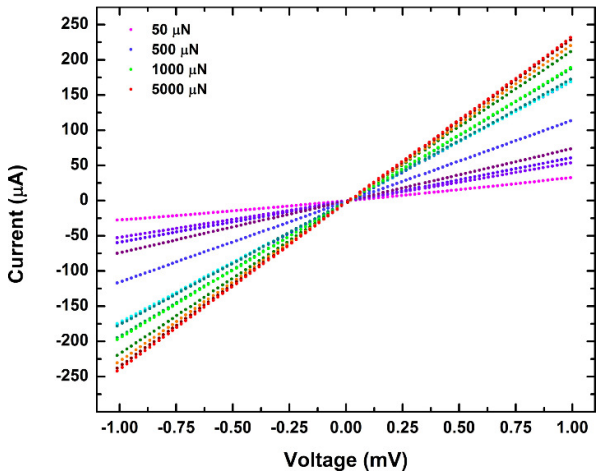

Figure B.10. *In situ* voltage-current characteristics of indentation nano-contact on platinum films. Voltage sweeps are performed at constant maximum loads from 50 to 5000 μN.

B.3.1. Elastic nano-contacts

At penetration depths smaller than ~8 nm (indentation loads <50 μN), the nanoscale contact resistance is 3-5 orders of magnitude higher than at larger penetration depths (Figure 5.9a,c) and decreases at a faster rate with indentation load/depth. The abrupt change in the contact resistance beyond this point likely denotes the onset of plastic deformation in the nano-crystalline platinum film beyond which the contact area increases rapidly. A series of 50 μN indentation experiments confirm the elastic nature of the contact (Figure B.11). At this load range, the mechanical response of the nano-contact remains in a purely elastic regime. In the loading segments, the nano-contact current increases in line with the progressively increasing nano-contact area. However, the nano-contact current in the unloading segments typically does not follow the same trace as the loading current. This behavior likely stems from friction effects and inelastic slipping of the nano-contact at grain boundaries due to thermal drift which becomes more pronounced as larger currents pass through the nano-contact area. During these experiments, the contact resistance

remains in the high resistance regime where it's mainly limited by the high resistivity of the indenter contact at its rounding sphere ($\rho_{i,max}$ = 933.4 μΩ.cm). The diameter of the electrical contacts in the elastic regime was calculated to be 17.2 nm < *d* < 44.3 nm which i comparable with the estimated electron mean free path for the platinum films and therefore the contact can be categorized to be in the quasi-ballistic regime.

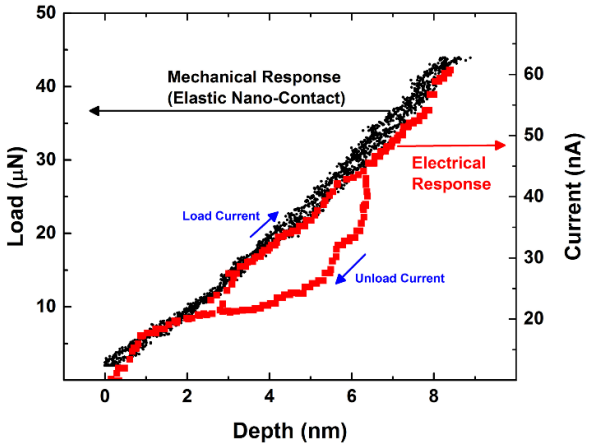

Figure B.11. Nano-electromechanical response of the platinum films under ultra low indentation loads (45 μN). The mechanical response is fully elastic and the contact resistivity is constant.

Assuming a constant resistivity at the indenter's rounding sphere, the resistivity of nano-crystalline platinum films is uniform and is calculated to be 31.1 μΩ.cm. This higher resistivity compared to the average value (16.3 μΩ.cm) mostly stems from the electron scattering at the grain boundaries and roughness effects [B.23-25].

B.3.2. Nano-contacts in the elasto-plastic regime

The abrupt decrease in the contact resistance between the conductive indenter and nano-crystalline platinum films at the onset of plastic deformation is ascribed to a sharp drop of the modeled indenter's resistivity profile at higher

penetration depths as well as the increase in the true electrical contact area subject to increasing contact loads. The electrical contact area increases at higher indentation depths/loads partly as a result of the plastic deformation (i.e. flattening) of individual grains that form the conductive spots at the contact. Moreover, the friction and drift rate effects become negligible at higher loads and penetration depths which results in the progressive decrease of contact resistance at increased load/penetration (Figure B.9b,d). The resistivity of the platinum films in this regime is characterized from measured contact resistances. Figure B.12 illustrates the platinum film's resistivity *vs.* penetration depth averaged from the values in loading and unloading segments with contact loads less than 20% of the peak indentation load. The average resistivity for penetration depths larger than 25 nm is calculated to be 17.6 (± 2%) μΩ.cm which is only slightly higher than the average resistivity (16.5 μΩ.cm). The initially higher resistivity is mainly due to the surface roughness effects. As illustrated in Figure 9 and 11, a stable ohmic nano contact is formed during in situ electrical nanoindentation experiment for all elastic and elasto-plastic nano-contacts, regardless of the maximum indentation force and the loading rate. The empirical relationship between the inherent resistivity of the sample and the evolution of the nano-contact load/depth described by Equation (7) in Chapter 5, does not directly account for the surface roughness effects and electron scattering at the grain boundaries in the largely elastic shallow depth nano contacts. As such, resistivity values calculated from the contact resistance of shallow depth nano-contacts (with contact depths < 15 nm) are expected to be higher than the actual inherent resistivity, since the contact resistance values include the added surface resistance due to such effects. However, since the

geometrical irregularities and the initial high resistivity of the indenter tip are accounted for, the higher calculated resistivity values are a good indicator of the presence and the impact of such surficial effects.

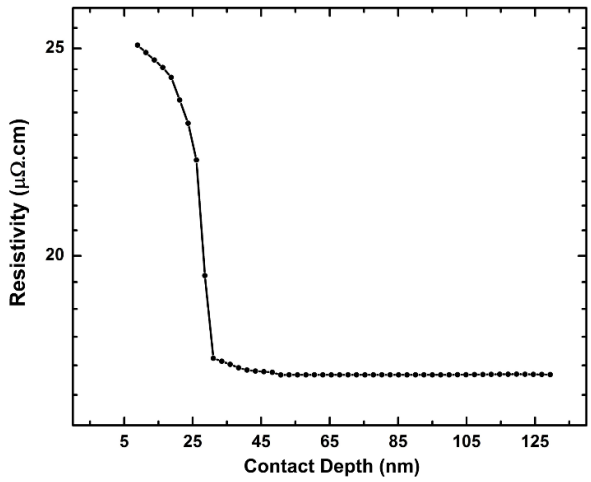

Figure B.12. Nanoscale resistivity of platinum films *vs.* nano-contact depth. Resistivtiy at moderate to large depth nano-contacts, is almost identical to the average resistivity value of the films.

Figure B.13a depicts the resistivity of the platinum subject to indentation load. These values are calculated from *I-V* sweeps at peak indentation loads. At low peak loads, the resistivity values are identical to those in Figure B.12. However, at higher loads the resistivity of the platinum films start to increase, despite an increase in contact area and an overall decrease of measured contact resistances. As such, the increase is possibly indicative of an increase in dislocation density of platinum at the nanoscale contact due to severe plastic deformation. Interestingly, the indentation load/depth threshold for the resistivity increase corresponds closely to the load/depth threshold at which the pile-up deformation around the contact area begins to appear (Figure B.13b). This may

help reveal the origin of pile-up deformations which can be ascribed to the structural deformations and shear-plane movements in the platinum films at the nanoscale contact area when subjected to high mechanical stress.

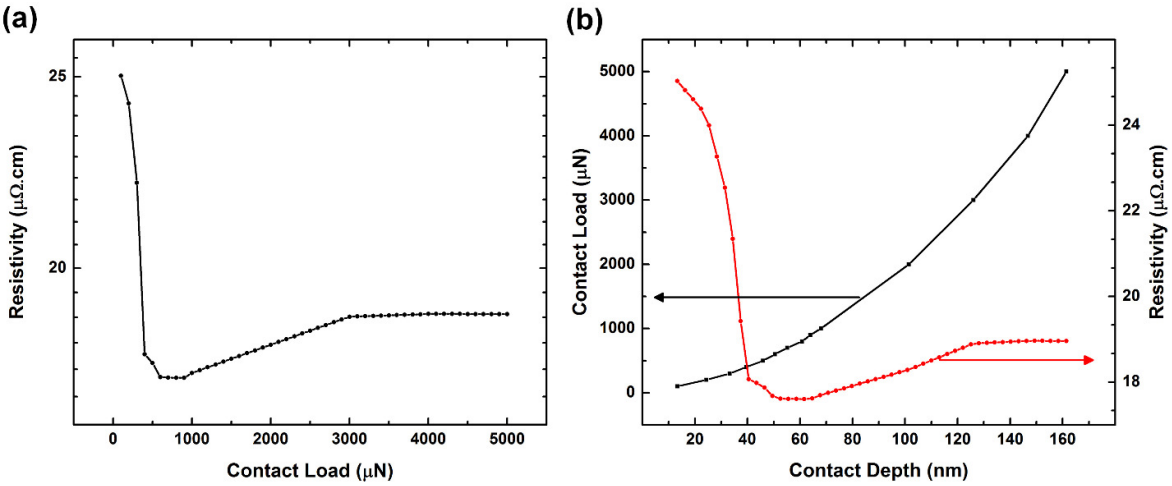

Figure B.13. The effect of mechanical load on the nanoscale resistivity of platinum films. At high contact loads, where pile-up deformations start to appear around the contact, the resistivity of the films start to rise.

To conclude, the nanomechanical and the nanoscale electrical properties of nano-crystalline platinum thin films have been precisely characterized utilizing *in situ* electrical nanoindentation. The influence of substrate structure as well as the effect of indenter's geometry profile, loading rate and pile-up formation have been considered to accurately characterize the nanomechanical properties of platinum films. Moreover, the nanoscale electrical properties of platinum films have been assessed *via* the use of an empirical relationship between the measured contact resistances and the modeled resistivity profile of the conductive indenter versus contact load/depth. Precise assessments of the nanoscale electrical properties of nano-crystalline platinum films at elastic and plastic nano-contacts have been achieved across a wide range of contact sizes and loads.

APPENDIX C

IN SITU CHARACTERIZATION OF NANOSCALE ELECTROMECHANICAL PROPERTIES OF QUASI-TWO-DIMENSIONAL MoS_2 AND MoO_3

Precise manipulation of electronic band structures of two-dimensional (2D) transition metal dichalcogenides and oxides (TMD&Os) via localized strain engineering is an exciting avenue for exploiting their unique characteristics for electronics, optoelectronics, and nano-electromechanical systems (NEMS) applications. Engineered mechanically-induced electrical transitions in quasi-2D molybdenum disulphide (MoS_2) and molybdenum trioxide (MoO_3) using an *in situ* electrical nanoindentation technique have been demonstrated. It is shown that localized strains on such quasi-2D layers can induce carrier transport alterations, thereby changing their electrical conduction behavior. Such strain effects offer a potential tool for precisely manipulating the electronic transport properties of 2D TMD&Os, and understanding the interactions of the atomic electronic states in such layered materials.

The report detailing the methods and the results of this investigation can be found on the publication archive system *arXiv* (arXiv:1409.4949).